

**SELF-ADJOINT SENSITIVITIES OF S -
PARAMETERS WITH TIME-DOMAIN TLM
ELECTROMAGNETIC SOLVERS**

**SELF-ADJOINT SENSITIVITIES OF S -
PARAMETERS WITH TIME-DOMAIN TLM
ELECTROMAGNETIC SOLVERS**

By
YING LI, B.E.

A Thesis
Submitted to the School of Graduate Studies
in Partial Fulfillment of the Requirements
for the Degree
Master of Applied Science

McMaster University
©Copyright by Ying Li, June 2006

MASTER OF APPLIED SCIENCE (2006)
(Electrical and Computer Engineering)

McMaster UNIVERSITY
Hamilton, Ontario

TITLE: **SELF-ADJOINT SENSITIVITIES OF S-
PARAMETERS WITH TIME-DOMAIN TLM
ELECTROMAGNETIC SOLVERS**

AUTHOR: YING LI
B.E. (Huazhong University of Science and Technology)

SUPERVISOR: Dr. Natalia Nikolova, Associate Professor
Department of Electrical and Computer Engineering
Dipl. Eng. (Technical University of Varna)
Ph.D. (University of Electro-Communication)
P. Eng. (Ontario)

CO-SUPERVISOR: Dr. Mohamed Bakr, Assistant Professor
Department of Electrical and Computer Engineering
B.Sc. (Cairo University)
M.Sc. (Cairo University)
Ph.D. (McMaster University)
P. Eng. (Ontario)

NUMBER OF PAGES: xviii, 143

ABSTRACT

The thesis presents an efficient self-adjoint approach to the S -parameter sensitivity analysis based on full-wave electromagnetic (EM) time-domain simulations with two commonly used numerical techniques: the finite-difference time-domain (FDTD) method and the transmission-line matrix (TLM) method. Without any additional simulations, we extract the response gradient with respect to all the design variables making use of the full-wave solution already generated by the system analysis. It allows the computation of the S -parameter derivatives as an independent post-process with negligible overhead. The sole requirement is the ability of the solver to export the field solution at user-defined points. Most in-house and commercial solvers have this ability, which makes our approach readily applicable to practical design problems.

In the TLM-based self-adjoint techniques, we propose an algorithm to convert the electrical and magnetic field solutions into TLM voltages. The TLM-based discrete adjoint variable method (AVM) is originally developed to use incident and reflected voltages as the state variables. Our conversion algorithm makes the TLM-AVM method applicable to all time-domain commercial solvers, FDTD simulators included, with comparable accuracy and less memory overhead. Our approach is illustrated through waveguide examples using a TLM-based commercial simulator.

Currently, our TLM-based self-adjoint approach is limited to loss-free homogeneous problems. However, our FDTD-based self-adjoint approach is valid for lossy inhomogeneous cases as well. The FDTD-based self-adjoint technique needs only the E -field values as the state variables. In order to make it also applicable to a TLM-based solver, whose mesh grid is displaced from the FDTD grid, we interpolate the E -field solution from the TLM mesh to that on the FDTD mesh. Our FDTD-based approach is validated through the response derivatives computation with respect to both shape and constitutive parameters in waveguide and antenna structures. The response derivatives can be used not only to guide a gradient-based optimizer, but also to provide a sufficient good initial guess for the solution of nonlinear inverse problems.

Suggestions for further research are provided.

ACKNOWLEDGMENTS

I wish to express my appreciation to Dr. Natalia Nikolova for her supervision and guidance during the course of the studies. I have greatly benefited from her expert advice, her knowledge and ideas. Her patience, encouragement and understanding during the years of study will always be remembered.

I am also grateful to Dr. Mohamed Bakr for his support and ideas at the important moments in the course of the research. His insight and encouragement during the research development are sincerely appreciated.

I would like to thank my colleagues Yan Li, Ahmed Sayed Mohamed, Payam Abolghasem, Peter Basl, Dongying Li and Jiang Zhu from the Computational Electromagnetics Laboratory for the helpful discussion during the research.

I would like also to thank the Department of Electrical and Computer Engineering, McMaster University, for a Research Assistantship, Teaching Assistantship and Scholarship.

Finally, I thank with all my heart my parents, Huafu Li and Guixiang Luo, for all their love, understanding and support.

CONTENTS

ABSTRACT	iii
ACKNOWLEDGMENTS	v
LIST OF FIGURES	ix
LIST OF TABLES	xviii
Chapter 1 INTRODUCTION	1
References	5
Chapter 2 COMPUTATION OF <i>S</i>-PARAMETERS FROM TIME-DOMAIN		
FIELD SOLUTIONS	9
2.1 Introduction	9
2.2 Scattering Parameters	10
2.3 De-embedding Techniques	11
2.4 FDTD Basics	13
2.5 TLM Basics	16
2.6 Validation Examples	18
2.6.1 Inductive Metallic Obstacle	19
2.6.2 Single-resonator Filter	25
2.7 Summary	32

2.8	References.....	33
Chapter 3	TLM-BASED SELF-ADJOINT SENSITIVITY ANALYSIS	35
3.1	Introduction.....	35
3.2	Adjoint Variable Method for Time-domain TLM Method.....	36
3.3	TLM-based Adjoint Variable Method for S -parameters.....	38
3.4	TLM-based Self-adjoint Sensitivity Theory	41
3.5	Conversion from Field Quantities to Incident Impulses	43
3.6	Validation Examples.....	44
3.6.1	Inductive Metallic Obstacle	45
3.6.2	Single-resonator Filter.....	48
3.6.3	H -plane Filter	52
3.6.4	Single-section Waveguide Impedance Transformer	57
3.7	Summary.....	68
3.8	References.....	69
Chapter 4	FDTD-BASED SELF-ADJOINT SENSITIVITY ANALYSIS.....	71
4.1	Introduction.....	71
4.2	Adjoint Variable Method for the FDTD Method.....	72
4.3	FDTD-based Self-adjoint Sensitivity Theory	77
4.4	Conversion from TLM mesh to FDTD Mesh.....	82
4.5	De-embedding Technique for AVM.....	83
4.6	Validation Examples.....	84

4.6.1	Single-resonator Filter.....	86
4.6.2	Single-section Waveguide Impedance Transformer	89
4.6.3	Dielectric-resonator Filter	100
4.6.4	Dielectric-resonator Antenna	111
4.7	Summary	116
4.8	References.....	117
Chapter 5	TIME DOMAIN SENSITIVITY ANALYSIS OF LOSSY INHOMOGENEOUS STRUCTURES	119
5.1	Introduction.....	119
5.2	FDTD-based AVM Theory with Material Parameters	121
5.3	Validation Examples.....	123
5.3.1	Normally Incident TEM Plane Wave in a Lossy Layered Medium.	123
5.3.2	Object in the 2D Lossy Layered Medium	127
5.4	Summary	131
5.5	References.....	131
Chapter 6	CONCLUSIONS	133
	COMPLETE REFERENCE LIST	137

LIST OF FIGURES

Figure 2.1.	Illustration of the source, observation and de-embedding planes in the waveguide ports of a 2-port structure when the de-embedding of the S -parameter is with respect to the outermost discontinuities of the structure.	12
Figure 2.2.	Allocation of the electric and magnetic field components on the Yee cell.	14
Figure 2.3.	2D TLM shunt node.	17
Figure 2.4.	The inductive metallic obstacle example.	20
Figure 2.5.	Top view of the inductive metallic obstacle structure in MEFiSTo.	20
Figure 2.6.	Magnitude of S_{11} of the inductive metallic obstacle.	22
Figure 2.7.	Phase of S_{11} of the inductive metallic obstacle.	23
Figure 2.8.	Magnitude of S_{21} of the inductive metallic obstacle.	23
Figure 2.9.	Phase of S_{21} of the inductive metallic obstacle.	24
Figure 2.10.	Derivatives of $ S_{11} $ with respect to W in the inductive metallic obstacle example.	25
Figure 2.11.	Derivatives of $ S_{21} $ with respect to W in the inductive metallic obstacle example.	25

Figure 2.12.	The single-resonator filter.....	26
Figure 2.13.	Top view of the single-resonator filter structure in MEFiSTo.	26
Figure 2.14.	Johns boundaries of the single-resonator filter.	28
Figure 2.15.	Magnitude of S_{11} of the single-resonator filter.....	29
Figure 2.16.	Phase of S_{11} of the single-resonator filter.....	30
Figure 2.17.	Magnitude of S_{21} of the single-resonator filter.	30
Figure 2.18.	Phase of S_{21} of the single-resonator filter.	31
Figure 2.19.	Derivatives of $ S_{11} $ with respect to W in the single-resonator filter example.....	32
Figure 2.20.	Derivatives of $ S_{21} $ with respect to W in the single-resonator filter example.....	32
Figure 3.1.	TLM-based AVM probes at the obstacle boundaries (assume increasing W) in the metallic obstacle example.	46
Figure 3.2.	Derivatives of $ S_{11} $ with respect to D in the inductive metallic obstacle example.....	46
Figure 3.3.	Derivatives of $ S_{21} $ with respect to D in the inductive metallic obstacle example.....	47
Figure 3.4.	Derivatives of $ S_{11} $ with respect to W in the inductive metallic obstacle example.....	47
Figure 3.5.	Derivatives of $ S_{21} $ with respect to W in the inductive metallic obstacle example.....	48

Figure 3.6.	TLM-based AVM probes at the right septum (assume increasing D) in the single-resonator filter example.	49
Figure 3.7.	TLM-based AVM probes at the right septum (assume increasing W) in the single-resonator filter example.	49
Figure 3.8.	Derivatives of $ S_{11} $ with respect to D in the single-resonator filter example.	50
Figure 3.9.	Derivatives of $ S_{21} $ with respect to D in the single-resonator filter example.	50
Figure 3.10.	Derivatives of $ S_{11} $ with respect to W in the single-resonator filter example.	51
Figure 3.11.	Derivatives of $ S_{21} $ with respect to W in the single-resonator filter example.	51
Figure 3.12.	The six-resonator H -plane filter and its nominal design.	52
Figure 3.13.	S -parameters of the six-resonator H -plane filter.	54
Figure 3.14.	Derivatives of $ S_{11} $ with respect to L_1 in the H -plane filter example.	55
Figure 3.15.	Derivatives of $ S_{21} $ with respect to L_1 in the H -plane filter example.	55
Figure 3.16.	Derivatives of $ S_{11} $ with respect to W_4 in the H -plane filter example. ...	56
Figure 3.17.	Derivatives of $ S_{21} $ with respect to W_4 in the H -plane filter example. ...	56
Figure 3.18.	The single-section waveguide impedance transformer.	57
Figure 3.19.	S -parameters of the single-section waveguide impedance transformer. ...	59

Figure 3.20.	Derivatives of $ S_{11} $ respect to L in the waveguide impedance transformer example.	61
Figure 3.21.	Derivatives of $ S_{21} $ respect to L in the waveguide impedance transformer example.	62
Figure 3.22.	Convergence analysis of the derivatives of $ S_{11} $ with respect to L in the waveguide impedance transformer example.	63
Figure 3.23.	Convergence analysis of the derivatives of $ S_{21} $ with respect to L in the waveguide impedance transformer example.	63
Figure 3.24.	Convergence analysis of the derivatives of $ S_{11} $ with respect to W in the waveguide impedance transformer example.	64
Figure 3.25.	Convergence analysis of the derivatives of $ S_{21} $ with respect to W in the waveguide impedance transformer example.	64
Figure 3.26.	Derivatives of $ S_{11} $ with respect to L in the waveguide impedance transformer example (parameter sweep of L).	65
Figure 3.27.	Derivatives of $ S_{21} $ with respect to L in the waveguide impedance transformer example (parameter sweep of L).	66
Figure 3.28.	Derivatives of $ S_{11} $ with respect to W in the waveguide impedance transformer example (parameter sweep of W).	66
Figure 3.29.	Derivatives of $ S_{21} $ with respect to W in the waveguide impedance transformer example (parameter sweep of W).	67

Figure 3.30. Convergence analysis of the error with respect to W in the waveguide impedance transformer example.	68
Figure 4.1. H -plane view of the 2D TLM and FDTD mesh.	83
Figure 4.2. FDTD-based AVM probes (marked with circles) at the right septum (assume increasing D) in the single-resonator filter example.	86
Figure 4.3. FDTD-based AVM probes (marked with circles) at the right septum (assume increasing W) in the single-resonator filter example.	87
Figure 4.4. Derivatives of $ S_{11} $ with respect to D in the single-resonator filter example.	87
Figure 4.5. Derivatives of $ S_{21} $ with respect to D in the single-resonator filter example.	88
Figure 4.6. Derivatives of $ S_{11} $ with respect to W in the single-resonator filter example.	88
Figure 4.7. Derivatives of $ S_{21} $ with respect to W in the single-resonator filter example.	89
Figure 4.8. FDTD-based AVM probes (marked with circles) at the matching section boundaries (assume increasing L) in the waveguide impedance transformer example.	90
Figure 4.9. Derivatives of $ S_{11} $ with respect to L in the waveguide impedance transformer example.	91

Figure 4.10.	Derivatives of $ S_{21} $ with respect to L in the waveguide impedance transformer example.	91
Figure 4.11.	Convergence analysis of the derivatives of $ S_{11} $ with respect to L in the waveguide impedance transformer example.....	93
Figure 4.12.	Convergence analysis of the derivatives of $ S_{21} $ with respect to L in the waveguide impedance transformer example.....	93
Figure 4.13.	Convergence analysis of the derivatives of $ S_{11} $ with respect to W in the waveguide impedance transformer example.....	94
Figure 4.14.	Convergence analysis of the derivatives of $ S_{21} $ with respect to W in the waveguide impedance transformer example.....	94
Figure 4.15.	Convergence analysis of the error with respect to W in the waveguide impedance transformer example.	95
Figure 4.16.	Derivatives of $ S_{11} $ with respect to L in the waveguide impedance transformer example (parameter sweep of L).	96
Figure 4.17.	Derivatives of $ S_{21} $ with respect to L in the waveguide impedance transformer example (parameter sweep of L).	97
Figure 4.18.	Derivatives of $ S_{11} $ with respect to W in the waveguide impedance transformer example (parameter sweep of W).	97
Figure 4.19.	Derivatives of $ S_{21} $ with respect to W in the waveguide impedance transformer example (parameter sweep of W).	98

Figure 4.20.	H -plane view of the dielectric-resonator filter.....	100
Figure 4.21.	S -parameters of the dielectric-resonator filter.....	102
Figure 4.22.	FDTD-based AVM probes (marked with circles) at the post boundaries (left post assume increasing w , right post assume decreasing w) in the dielectric-resonator filter example.	102
Figure 4.23.	Derivatives of $ S_{11} $ with respect to w in the dielectric-resonator filter example.	103
Figure 4.24.	Derivatives of $ S_{21} $ with respect to w in the dielectric-resonator filter example.	104
Figure 4.25.	Derivatives of $ S_{11} $ with respect to s in the dielectric-resonator filter example.	104
Figure 4.26.	Derivatives of $ S_{21} $ with respect to s in the dielectric-resonator filter example.	105
Figure 4.27.	Derivatives of $ S_{11} $ with respect to w in the dielectric-resonator filter example (parameter sweep of w).	106
Figure 4.28.	Derivatives of $ S_{21} $ with respect to w in the dielectric-resonator filter example (parameter sweep of w).	107
Figure 4.29.	Derivatives of $ S_{11} $ with respect to s in the dielectric-resonator filter example (parameter sweep of s).	107

Figure 4.30.	Derivatives of $ S_{21} $ with respect to s in the dielectric-resonator filter example (parameter sweep of s).	108
Figure 4.31.	Derivatives of $ S_{11} $ with respect to w in the dielectric-resonator filter example (parameter sweep of s).	108
Figure 4.32.	Derivatives of $ S_{21} $ with respect to w in the dielectric-resonator filter example (parameter sweep of s).	109
Figure 4.33.	Derivatives of $ S_{11} $ with respect to s in the dielectric-resonator filter example (parameter sweep of w).	109
Figure 4.34.	Derivatives of $ S_{21} $ with respect to s in the dielectric-resonator filter example (parameter sweep of w).	110
Figure 4.35.	The dielectric-resonator antenna and its nominal design.....	112
Figure 4.36.	The return loss of the dielectric-resonator antenna.....	112
Figure 4.37.	The derivative $ S_{11} $ with respect to c of the dielectric-resonator antenna.	115
Figure 5.1.	The structure of the 1D lossy-medium example.....	123
Figure 5.2.	Derivative of $ S_{11} $ with respect to the conductivity σ_2 of the central layer in the 1D lossy medium example.....	125
Figure 5.3.	Derivative of $ S_{21} $ with respect to the length L of the central layer in the 1D lossy medium example.....	126
Figure 5.4.	Top view of the structure in the 2D example.....	127

Figure 5.5.	Derivatives of $ F_{P_k R} $, $k = 1, 2, 3$, with respect to σ_3 of the central object for a sweep of σ_3 at 0.9 GHz.	129
Figure 5.6.	Derivatives of $ F_{P_1 R} $ with respect to the width W of the central object for a sweep of W at 2.6 GHz.....	130

LIST OF TABLES

Table 2.1.	Setup of the inductive metallic obstacle simulation	21
Table 2.2.	Setup of the single-resonator filter simulation.....	27
Table 3.1.	Setup of the H -plane filter simulation.....	53
Table 3.2.	Setup of the single-section waveguide impedance transformer simulation	58
Table 4.1.	CPU time for the dielectric-resonator filter example.....	99
Table 4.2.	Setup of the dielectric-resonator filter simulation	101
Table 4.3.	CPU time for the dielectric-resonator filter example.....	111
Table 4.4.	Setup of the dielectric-resonator antenna. simulation.....	113
Table 5.1.	Setup of the 1D lossy-medium example simulation	124
Table 5.2.	Setup of the 2D lossy layered medium example simulation.....	128

Chapter 1

INTRODUCTION

The design sensitivity analysis of dynamic distributed systems [1],[2] has become increasingly important since the advent of a variety of numerical techniques for transient solutions. These techniques enable the software for broadband analysis and design. However, they are time-intensive to an extent, which often makes the design cycle prohibitively slow. To address this problem, many researchers work on the acceleration of the analysis methods. In contrast, we focus on the extraction of additional information from the field solution, namely, the response derivatives (sensitivities) with respect to the design shape and material parameters. The sensitivities, together with the responses, double our knowledge of the system behaviour in the design parameter space. They offer a measure of the system tolerances, and, when properly used, reduce the number of simulation calls from the optimizer. They can also be used to provide a sufficiently good initial guess for the solution to inverse microwave imaging problems arising in biomedical diagnostics and non-destructive testing.

Recently, significant progress in the sensitivity analysis of transient electromagnetic (EM) systems has been made. An exact adjoint-variable expression was

proposed for high-frequency problems [3]-[6]. Examples included 2D waveguide structures analyzed with unstructured-grid finite-element time-domain (FE-TD) [4] and finite-difference time-domain discrete surface integral (FDTD-DSI) [3], [5] techniques. The response of interest was the transmitted or reflected energy through a port. The major drawback of the exact approach is the requirement for analytical system matrix derivatives, which confines its applicability to unstructured-grid solvers. On the other hand, the widely used time-domain solvers are based on structured grids, e.g., the FDTD [7] and the transmission-line matrix (TLM) [8], [9] methods.

An alternative was proposed by Bakr *et al.* [10] and Nikolova *et al.* [11] for TLM and FDTD analyses, respectively. Discrete sensitivity expressions are derived based on the time-domain (TD) TLM method in [10] and the E -field vector wave equation in [11], respectively. They do not need analytical system matrix derivatives and allow sensitivity computations in a discrete design parameter space, i.e., on structured grids. Very good accuracy was demonstrated for functions of the energy type.

In all adjoint-sensitivity approaches, [3] (FDTD-DSI based), [10] (TD-TLM based) and [11] (Yee-FDTD based), an adjoint simulation is required for the derivatives of the energy response. The computational load of the adjoint simulation is equivalent to that of the usual EM simulation and constitutes the major part of the overhead of the sensitivity calculation. Another complication arises from the excitation of the adjoint simulation – its distribution in space-time is response-dependent. As a result, it is difficult to set up in a commercial solver. This limits the applicability to in-house codes.

In microwave design, the S -parameters are essential. Bakr *et al.* have demonstrated their sensitivity analysis with in-house TLM solvers, where the solution is in terms of incident voltages [12]. Furthermore, in [13] they showed that self-adjoint TLM formulation is possible for the case of loss-free homogeneous structures, where no adjoint simulations are necessary.

In this thesis, we propose a general self-adjoint approach to S -parameter sensitivity computation, which is based on either TLM [10] or FDTD [11] discretization schemes. It is general in the sense that in both schemes we use the E -field solution. This solution is available with any time-domain commercial EM solver, such as MEFiSTo-3D Pro [14] or XFDTD [15]. Adjoint simulations are not needed. The only requirement is the ability of the simulator to export the field solution at user-defined points. Our algorithm is implemented in MATLAB [16]. The FDTD-based self-adjoint approach is valid for lossy inhomogeneous structures, while the TLM-based approach is so far limited to a homogeneous medium.

The author's contributions include:

- 1) The implementation of the TLM-based self-adjoint sensitivity analysis with commercial simulators where the E -field is the state variable.
- 2) The development of the FDTD-based self-adjoint sensitivity analysis for S -parameters and its implementation with a TLM-based simulator.
- 3) The implementation of the FDTD-based self-adjoint approach in lossy dielectric inhomogeneous structures.

Some of this work has been submitted or accepted for publication [17]-[19].

Chapter 2 introduces the S -parameter calculation and the de-embedding technique in the time-domain. We also review briefly the TLM and FDTD methods, which are used as discretization schemes in our self-adjoint sensitivity analysis.

Chapter 3 discusses the TLM-based self-adjoint approach [15]. We begin with a summary of the TLM-based discrete adjoint-variable method (AVM) [10] and its application to S -parameter sensitivity computation [12]. Next, we outline the self-adjoint approach [13], i.e., how to derive the S -parameter adjoint-field solutions from the original problem solutions and how to use them in the discrete sensitivity formula. Then, we describe in detail the algorithm which converts the E -field and H -field quantities to TLM voltages. Finally, we illustrate our approach by 2D waveguide examples developed with the TLM-based commercial solver MEFiSTo-3D Pro [14].

Chapter 4 focuses on the FDTD-based self-adjoint approach to the computation of the S -parameter derivatives with respect to shape parameters [18]. We introduce the FDTD-AVM theory [11] first. Then we develop the self-adjoint approach for the FDTD-based discretization scheme. The conversion method from the TLM mesh to the FDTD mesh is addressed. It allows for the use of the TLM-based solutions with the FDTD-AVM. The approach is validated by the same hollow waveguide structures considered in Chapter 3, as well as loss-free dielectric waveguide and antenna structures. We discuss the CPU time and storage requirements in the examples.

Chapter 5 investigates the FDTD-based self-adjoint approach in lossy inhomogeneous structures [19]. The response derivatives are obtained with respect to

both the shape and constitutive parameters. The approach is verified through 1D and 2D examples where the inhomogeneous medium features high permittivities and losses.

The thesis concludes in Chapter 6 with a summary and suggestions for further research.

References

- [1] E.J. Haug, K.K. Choi and V. Komkov, *Design Sensitivity Analysis of Structural Systems*. Orlando: Academic Press Inc., 1986, pp. 70-77, pp. 167-178.
- [2] E.J. Haug and J. C  a, eds., *Optimization of Distributed Parameter Structures*. Alphen aan den Rijn, the Netherlands: Sijthoff & Noordhoff, 1981.
- [3] Y. Chung, C. Cheon, I. Park, and S. Hann, "Optimal shape design of microwave device using FDTD and design sensitivity analysis," *IEEE Trans. Microwave Theory Tech.*, vol. 48, pp. 2289-2296, Dec. 2000.
- [4] Y. Chung, J. Ryu, C. Cheon, I. Park and S. Hahn, "Optimal design method for microwave device using time domain method and design sensitivity analysis – part I: FETD case," *IEEE Trans. Magnetice*s, vol. 37, pp. 3289-3293, Sep. 2001.
- [5] Y. Chung, J. Ryu, C. Cheon, I. Park and S. Hahn, "Optimal design method for microwave device using time domain method and design sensitivity analysis – part II: FDTD case," *IEEE Trans. Magnetice*s, vol. 37, pp. 3255-3259, Sep. 2001.
- [6] N.K. Nikolova, J.W. Bandler, and M.H. Bakr, "Adjoint techniques for sensitivity analysis in high-frequency structure CAD," *IEEE Trans. Microwave Theory Tech.*, vol. 52, pp. 403-419, Jan. 2004.

- [7] A. Taflove, S.C. Hagness, *Computation Electrodynamics: The Finite Difference Time-Domain Method*, 2nd ed. Boston: Artech House, 2000.
- [8] C. Christopoulos, *The Transmission-Line Modeling Method TLM*. Oxford: IEEE/Oxford University Press, 1995.
- [9] W.J.R. Hoefer, "The transmission-line matrix method – theory and applications," *IEEE Trans. Microwave Theory Tech.*, vol. MTT-33, pp. 882-893, Oct. 1985.
- [10] M.H. Bakr and N.K. Nikolova, "An adjoint variable method for time domain TLM with fixed structured grids," *IEEE Trans. Microwave Theory Tech.*, vol. 52, pp. 554-559, Feb. 2004.
- [11] N.K. Nikolova, H.W. Tam, and M.H. Bakr, "Sensitivity analysis with the FDTD method on structured grids," *IEEE Trans. Microwave Theory Tech.*, vol. 52, pp. 1207-1216, April 2004.
- [12] M.H. Bakr and N.K. Nikolova, "Efficient estimation of adjoint-variable *S*-parameter sensitivities with time domain TLM," *Int. J. of Numerical Modelling: Electronic Networks, Devices and Fields*, vol. 18, no. 2, March/April 2005, pp. 171-187.
- [13] M.H. Bakr, N.K. Nikolova, and P.A.W. Basl, "Self-adjoint *S*-parameter sensitivities for lossless homogeneous TLM problems," *Int. J. of Numerical Modelling: Electronic Networks, Devices and Fields*, vol. 18, no. 6, Nov. 2005, pp. 441-455.
- [14] MEFiSTo-3D[®] Pro v. 4, *User Guide and Operating Manual*, 6th ed., Faustus Scientific, Jan. 2003, <http://www.faustcorp.com/products/mefisto3dpro/> .

- [15] XFDTD[®] v. 6.2, *Reference Manual*, Remcom, 2004,
<http://www.remcom.com/xfDTD6/> .
- [16] MATLAB[®] v. 7, The MathWorks, Inc.,
<http://www.mathworks.com/products/matlab/> .
- [17] Ying Li, N.K. Nikolova, and M.H. Bakr, “TLM-based self-adjoint sensitivities of S-parameters with time-domain electromagnetic solvers”, accepted by *IEEE MTT-S International Microwave Symposium*, 2006.
- [18] N.K. Nikolova, Ying Li, Yan Li, and M.H. Bakr, “Sensitivity analysis of scattering parameters with electromagnetic time-domain simulators,” *IEEE Trans. Microwave Theory Tech.*, vol. 54, no. 4, pp. 1598-1610, April 2006.
- [19] Ying Li, Yan Li, N.K. Nikolova, and M.H. Bakr, “Time domain sensitivity analysis of lossy dielectric structures,” accepted by *Frontiers in Applied Computational Electromagnetics*, 2006.

Chapter 2

COMPUTATION OF *S*-PARAMETERS FROM TIME-DOMAIN FIELD SOLUTIONS

2.1 Introduction

Most EM solvers are able to compute the *S*-parameters for a given structure. In this chapter, we first define the *S*-parameters in a *K*-port waveguide structure and the related de-embedding technique. Second, we briefly outline the basics of the FDTD and TLM methods. Third, we describe the detailed procedures to set up a correct solution in the TLM-based commercial solver MEFiSTo-3D Pro [1]. Waveguide examples are given. Their *S*-parameters generated by the solver are presented and compared with two other reference sets of data. They contain the *S*-parameters computed in MATLAB [2] with the field responses of MEFiSTo and the *S*-parameters produced directly by the frequency-domain solver HFSS [3]. Their finite-difference derivatives with different mesh sizes are also presented to ensure convergence and good accuracy. We later use these derivatives as a reference for our self-adjoint sensitivity computations. We conclude with a summary.

2.2 Scattering Parameters

The scattering parameters, or S -parameters, are the complex reflection and transmission coefficients dependent on the incident and reflected waves. They describe the behaviour of a device in the microwave frequency range. The S -parameters offer a complete description of the device performance in the microwave frequency range. They can also be converted to other parameters such as hybrid (H) or admittance (Y) parameters.

In a K -port structure, if the q th port is excited, the S_{pq} parameter for the mode ν at the frequency ω_0 is

$$S_{pq}^{(\nu, \omega_0)} = \sqrt{\frac{Z_q^{(\nu, \omega_0)}}{Z_p^{(\nu, \omega_0)}}} \cdot \frac{\tilde{F}_{pq}^{(\nu, \omega_0)}}{\tilde{F}_q^{(\nu, \omega_0)}} \quad (2.1)$$

$$\tilde{F}_{pq}^{(\nu, \omega_0)} = \int_0^{T_{\max}} \iint_{A_p} \mathbf{E}_{q\perp}^{ou}(x'_p, y'_p, t) \cdot \mathbf{e}_{p\perp}^{(\nu)}(x'_p, y'_p) dx'_p dy'_p \cdot e^{-j\omega_0 t} dt \quad (2.2)$$

$$\tilde{F}_q^{(\nu, \omega_0)} = \int_0^{T_{\max}} \iint_{A_q} \mathbf{E}_{q\perp}^{in}(x'_q, y'_q, t) \cdot \mathbf{e}_{q\perp}^{(\nu)}(x'_q, y'_q) dx'_q dy'_q \cdot e^{-j\omega_0 t} dt. \quad (2.3)$$

Here, \mathbf{E}_q is the field solution when port q is excited, x'_ξ and y'_ξ ($\xi = p, q$) are the local coordinates at the ξ th port plane, ω_0 is the frequency at which the S -parameters are computed, $Z_\xi^{(\nu, \omega_0)}$ is the wave impedance of the ξ th port. The superscripts *in* and *ou* denote an incoming and an outgoing wave, respectively. The subscript \perp denotes the field, which is transverse to the direction of propagation. The modal vector of the ξ th

port $\mathbf{e}_\xi^{(\nu)}$ gives the normalized distribution of the field across the port. In particular, the modal vector of the dominant TE_{z10} mode in a rectangular waveguide port is [4]

$$\mathbf{e}^{(\text{TE}_{10})}(x', y') = \hat{\mathbf{y}} \sqrt{\frac{2}{ab}} \sin\left(\frac{\pi}{a} x'\right) \quad (2.4)$$

where a and b denote the width and height of the port, respectively.

Differentiating (2.1) with respect to the design parameter p_n , we obtain

$$\frac{\partial S_{pq}^{(\nu, \omega_0)}}{\partial p_n} = \sqrt{\frac{Z_q^{(\nu, \omega_0)}}{Z_p^{(\nu, \omega_0)}}} \cdot \frac{1}{\tilde{F}_q^{(\nu, \omega_0)}} \cdot \frac{\partial \tilde{F}_{pq}^{(\nu, \omega_0)}}{\partial p_n}. \quad (2.5)$$

Here, $Z_p^{(\nu, \omega_0)}$, $Z_q^{(\nu, \omega_0)}$, and $\tilde{F}_q^{(\nu, \omega_0)}$ do not depend on p_n .

The sensitivities of the real and imaginary parts of the S_{pq} parameter $\partial \text{Re}(S_{pq})/\partial p_n$ and $\partial \text{Im}(S_{pq})/\partial p_n$ can be derived according to (2.5). Then, the sensitivities of the magnitude and phase of S_{pq} can be calculated as

$$\frac{\partial |S_{pq}|}{\partial p_n} = \frac{1}{|S_{pq}|} \left(\text{Re} S_{pq} \frac{\partial \text{Re} S_{pq}}{\partial p_n} + \text{Im} S_{pq} \frac{\partial \text{Im} S_{pq}}{\partial p_n} \right) \quad (2.6)$$

$$\frac{\partial (\text{Angle} S_{pq})}{\partial p_n} = \frac{1}{|S_{pq}|^2} \left(\text{Re} S_{pq} \frac{\partial \text{Im} S_{pq}}{\partial p_n} - \text{Im} S_{pq} \frac{\partial \text{Re} S_{pq}}{\partial p_n} \right). \quad (2.7)$$

2.3 De-embedding Techniques

The extracted S -parameters have a phase difference with respect to the reference plane because a port has to be located away from a discontinuity to guarantee an accurate

solution [5]. In Figure 2.1, the de-embedding plane, i.e. the reference plane, can be anywhere along the waveguide. The phase de-embedding modifications to (2.5) in different cases are as follows.

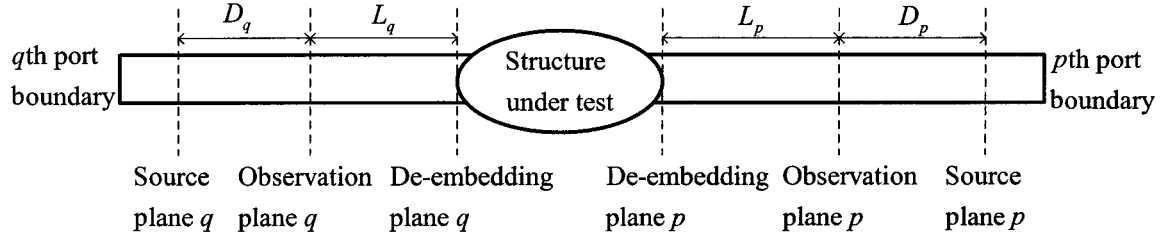


Figure 2.1. Illustration of the source, observation and de-embedding planes in the waveguide ports of a 2-port structure when the de-embedding of the S-parameter is with respect to the outermost discontinuities of the structure.

Case 1: De-embedding plane coincides with the source plane:

$$\frac{\partial S_{pq}}{\partial p_n} = \sqrt{\frac{Z_q}{Z_p}} \cdot \frac{1}{\tilde{F}_q^{obs}} \cdot \frac{\partial \tilde{F}_{pq}^{obs}}{\partial p_n} \cdot e^{(-\gamma_p D_p - \gamma_q D_q)}. \quad (2.8)$$

The superscript *obs* denotes the solution recorded at the observation plane. D_p and D_q are the distances between the source planes and the observation planes at the p th and q th port, respectively. γ_p and γ_q ($\gamma_\xi = \alpha_\xi + j\beta_\xi$, $\xi = p, q$) are the complex propagation constants of the p th and q th ports, respectively. In lossless cases, $\gamma_\xi = j\beta_\xi$. In free space,

$$\beta_\xi(f_m) = \sqrt{(2\pi f_m / c_0)^2 - (\pi / a_\xi)^2} \text{ for the TE}_{10} \text{ mode in the } \xi \text{ th port.}$$

Case 2: De-embedding plane coincides with the observation plane:

$$\frac{\partial S_{pq}}{\partial p_n} = \sqrt{\frac{Z_q}{Z_p}} \cdot \frac{1}{\tilde{F}_q^{obs}} \cdot \frac{\partial \tilde{F}_{pq}^{obs}}{\partial p_n}. \quad (2.9)$$

Case 3: De-embedding plane coincides with the discontinuity plane:

$$\frac{\partial S_{pq}}{\partial p_n} = \sqrt{\frac{Z_q}{Z_p}} \cdot \frac{1}{\tilde{F}_q^{obs}} \cdot \frac{\partial \tilde{F}_{pq}^{obs}}{\partial p_n} \cdot e^{(\gamma_p L_p + \gamma_q L_q)}. \quad (2.10)$$

L_p and L_q are the distances between the observation plane and the discontinuity plane at the p th and q th port, respectively. The de-embedding factor for the general case when the de-embedding plane is placed anywhere along the waveguide can be derived similarly.

2.4 FDTD Basics

The FDTD method is a numerical method for the solution of Maxwell's equations directly in the time domain over a properly discretized problem (the FDTD space). In 1966, K. S. Yee presented a numerical algorithm for the time domain solution of Maxwell's equations [6] and Taflov *et al.* gave it the name FDTD method [7]. The FDTD method can be applied to problems containing complex high frequency (HF) structures that may be difficult to solve using analytical methods. The transient responses are obtained from the field solution in space and in time. Fourier transform is applied to the transient data in order to obtain the frequency responses over a wide spectrum. The FDTD method can be applied to any inhomogeneous, lossy, anisotropic, time varying and dispersive media. That is why the FDTD method has been widely used for solving electromagnetic problems.

An EM problem in a linear medium can be described by the vector wave equation for the E -field

$$\nabla \times \mu^{-1} \nabla \times \mathbf{E} + \epsilon \frac{\partial^2 \mathbf{E}}{\partial t^2} + \sigma \frac{\partial \mathbf{E}}{\partial t} = -\frac{\partial \mathbf{J}}{\partial t} \quad (2.11)$$

where ϵ , μ and σ are the medium permittivity, permeability and conductivity, respectively. For a unique solution, zero boundary conditions and initial conditions are specified.

In Yee's FDTD grid, the positions of the electric components are half a spatial step away from the respective magnetic components. The allocation of the field components at the Yee cell is shown in Figure 2.2.

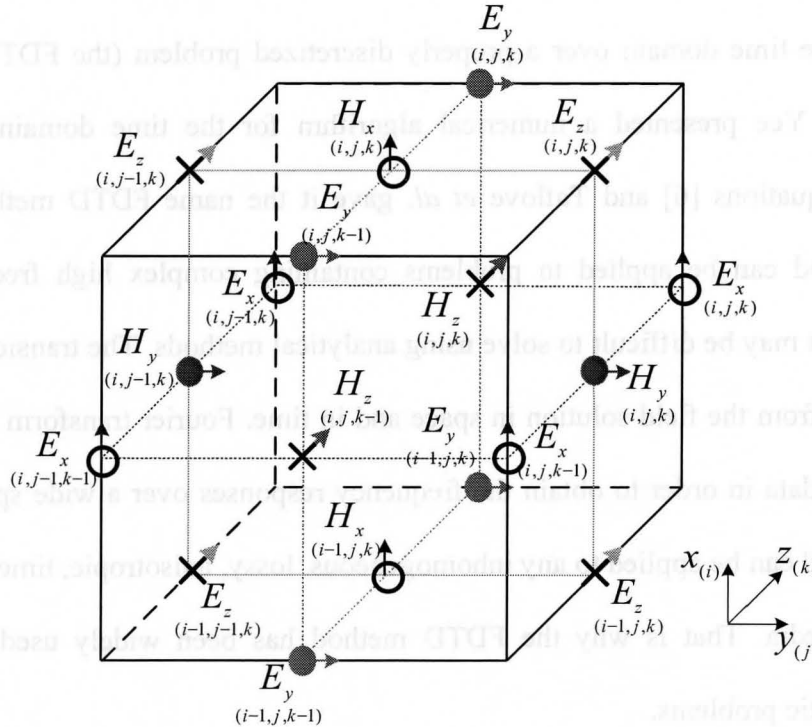


Figure 2.2. Allocation of the electric and magnetic field components on the Yee cell.

In order to ensure the numerical stability of the leap-frog algorithm for a general 3-D FDTD grid, Courant's stability criterion must be satisfied [8]. Equivalently, a numerical constant q is introduced, which must satisfy:

$$q = \frac{\Delta h}{c \cdot \Delta t} \geq \sqrt{3} \quad (2.12)$$

where Δt is the discrete time step and $\Delta h = \min(\Delta x, \Delta y, \Delta z)$. Here, Δx , Δy and Δz are the discretization steps along the x , y and z axes, respectively. c is the minimum velocity of propagation in any of the media in the problem.

In addition to the time-step constraint, the selection of the size of the Yee cell is also considered. In order to obtain sufficient spatial resolution of the computational domain, the cell size should be small enough corresponding to the highest frequency of interest:

$$\Delta h < \frac{\lambda_{min}}{18\sqrt{3}} \approx \frac{\lambda_{min}}{32}. \quad (2.13)$$

Also, for structures containing fine geometrical details, Δh must be chosen sufficiently small to represent them accurately and to allow for accurate representation of possible field singularities.

If Δh and Δt are chosen in accordance with the conditions in (2.12) and (2.13), the FDTD method will generate accurate and reliable responses. They are also the criterion that we set up our simulation in the commercial solvers.

2.5 TLM Basics

The transmission-line modelling (TLM), otherwise known as the transmission-line-matrix method, is a time-domain numerical technique for solving field problems using circuit equivalents. It is based on the equivalence between Maxwell's equations and the equations for voltages and currents on a mesh of continuous two-wire transmission lines. The main feature of this method is the simplicity of formulation and programming for a wide range of application [8].

The TLM method carries out a sequence of scattering and connection steps. The scattering relation of the j th node at the k th time step is given by

$$\mathbf{V}_{j,k}^R = \mathbf{S}^j \mathbf{V}_{j,k} \quad (2.14)$$

where $\mathbf{V}_{j,k}$ is the vector of incident impulses at the j th node, $\mathbf{V}_{j,k}^R$ is the vector of reflected impulses at the j th node, and \mathbf{S}^j is the scattering matrix of the j th node.

We assume that the computational domain is discretized into a total of N nodes with the node size Δl . We denote the total number of TLM links associated with the N nodes by N_L . One TLM step is given by

$$\mathbf{V}_{k+1} = \mathbf{C} \mathbf{S} \mathbf{V}_k + \mathbf{V}_k^S + \sum_{k'=0}^k \mathbf{G}(k-k') \mathbf{V}_{k'}^R \quad (2.15)$$

where $\mathbf{V}_k \in \mathbb{R}^{N_L}$ and $\mathbf{V}_k^R \in \mathbb{R}^{N_L}$ are the vectors of incident and reflected impulses, respectively, for all nodes at the k th time step. The matrix $\mathbf{S} \in \mathbb{R}^{N_L \times N_L}$ is the scattering matrix for all nodes and is assumed time-invariant. $\mathbf{C} \in \mathbb{R}^{N_L \times N_L}$ is the connection matrix describing how reflected impulses connect to neighboring nodes or non-dispersive

boundaries. The vector $V_k^S \in \mathbb{R}^{N_L}$ is the excitation vector at the k th time step. The last term in (2.15) represents the contribution of the Johns matrix boundary. The matrix $G(k) \in \mathbb{R}^{N_L \times N_L}$ is the k th time layer of the three dimensional Johns matrix. Here, we assume that the medium is reciprocal and thus the matrix $G(k)$ is symmetric $\forall k$. The simulation carries out N_t steps where $T_s = N_t \Delta t$ is the total simulation time.

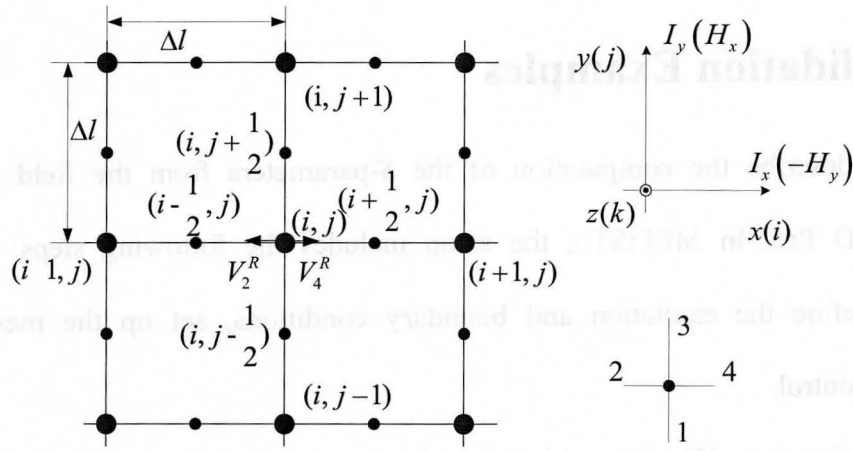


Figure 2.3 2D TLM shunt node.

In the 2D TLM shunt node, as in Figure 2.3, we have the following correspondences at any time and grid point:

$$V_z \equiv E_z, I_y \equiv H_x, I_x \equiv -H_y, 2C \equiv \varepsilon, L \equiv \mu \quad (2.16)$$

where ε and μ are the permittivity and permeability of the medium. The intrinsic impedance can be expressed as

$$Z_L = \sqrt{2\mu \varepsilon} \quad (2.17)$$

The nodes with an integer index are the actual nodes in the mesh where the E and H field quantities can be derived. Each node has 4 links which means 4 incident or reflected impulses. The incident impulses can be derived from the reflected impulses with the scattering and connection matrices [8]. In 3D problems, the symmetrical condensed node (SCN) is commonly used. All field components are co-located and computed at the center of the SCN.

2.6 Validation Examples

We describe the computation of the S -parameters from the field solution of MEFiSTo-3D Pro. In MEFiSTo, the setup includes the following steps: set up the structure, define the excitation and boundary conditions, set up the mesh and the simulation control.

We give two 2D waveguide examples to explain the procedure. We set “2D mode” editor and “GSCN (Generalized Symmetrical Condensed Node) mesh for H -plane” in MEFiSTo-3D Pro for the simulation. After we set the cell size Δh and define the mesh, the discrete time step Δt is determined automatically by the software, so that $q = \Delta h / c \Delta t = 2$. The results for the S -parameters are validated by HFSS.

The finite-difference (FD) approximation is a common way to calculate the derivatives. It is also used as a reference for our self-adjoint sensitivity results in the following chapters. For the S -parameters, the central finite-difference (CFD) approximation is given by

$$\left. \frac{\partial S(p, \varpi)}{\partial p} \right|_{CFD} \approx \frac{S(p + \Delta p, \varpi) - S(p - \Delta p, \varpi)}{2\Delta p}. \quad (2.18)$$

The forward finite-difference (FFD) approximation is defined as

$$\left. \frac{\partial S(p, \varpi)}{\partial p} \right|_{FFD} \approx \frac{S(p + \Delta p, \varpi) - S(p, \varpi)}{\Delta p}. \quad (2.19)$$

The backward finite-difference (BFD) approximation is defined as

$$\left. \frac{\partial S(p, \varpi)}{\partial p} \right|_{BFD} \approx \frac{S(p, \varpi) - S(p - \Delta p, \varpi)}{\Delta p} \quad (2.20)$$

where S may be any complex S -parameter, or its magnitude, or its phase; ϖ is the frequency; p is the design parameter. The smaller the perturbation Δp is, the more accurate and close to each other the 3 derivatives are. FFD and BFD have first-order accuracy while CFD is second-order. If the curves of the 3 approaches do not agree well, the cell size of the mesh in the time-domain simulation, which is also the step of the perturbation, might be too large.

2.6.1 Inductive Metallic Obstacle

The structure of the inductive metallic obstacle in a parallel-plate waveguide is given in Figure 2.4. The designable parameters are the dimensions of the obstacle $[D \ W]^T$. The dominant mode propagating along the waveguide is a TEM wave. The top view of the structure in the edit window of MEFiSTo is shown in Figure 2.5. The setup of the MEFiSTo simulation of the inductive metallic obstacle example is summarized in Table 2.1. In practice, the sources are located next to the input ports. The

observation points are located 2 cells away from their respective ports. Otherwise, de-embedding techniques in section 2.3 must be implemented.

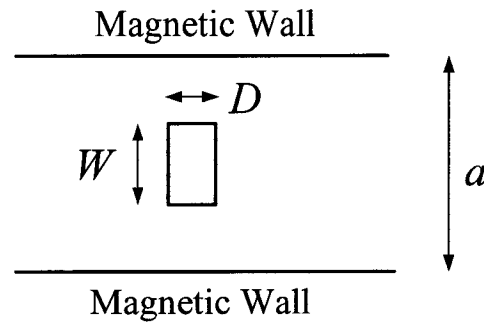


Figure 2.4. The inductive metallic obstacle example.

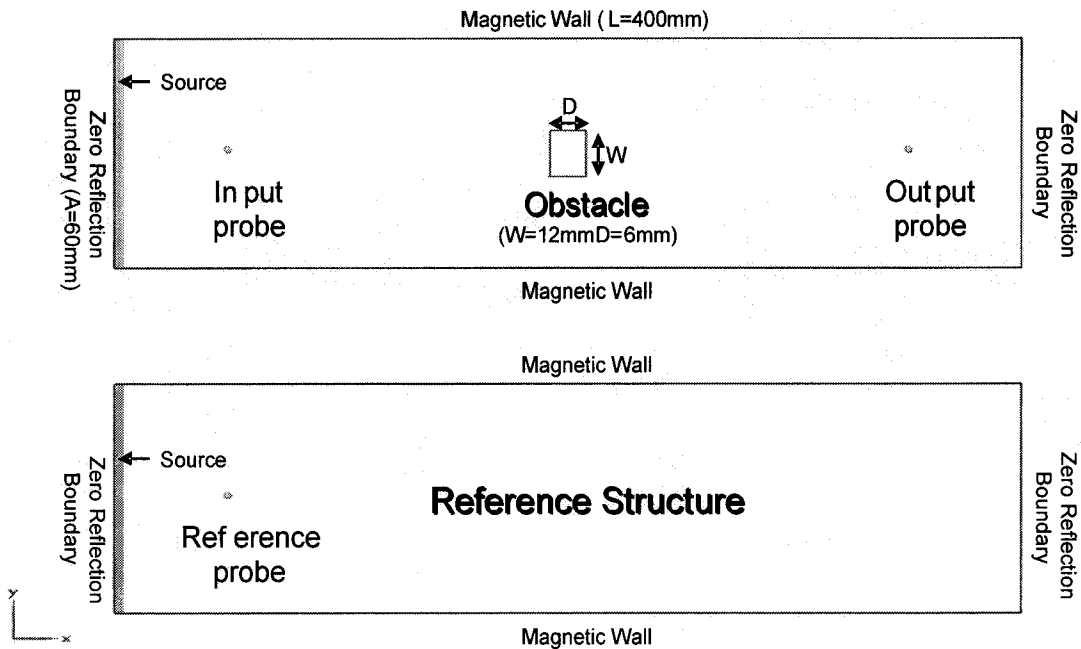


Figure 2.5. Top view of the inductive metallic obstacle structure in MEFiSTo.

Table 2.1. Setup of the inductive metallic obstacle simulation

Constant	Cell size Δh	1 mm
	Time step Δt	1.6678205 psec
Computational domain	Width of port a	60 mm (60 Δh)
	Length of the waveguide L_w	400 mm (400 Δh)
	Length of the obstacle D	6 Δh
	Width of the obstacle W	12 Δh
	Computational domain in space	400 $\Delta h \times 60 \Delta h$
	Total time steps	20,000 Δt
Port	Boundary condition	TEM wave absorbing boundary
	Modal distribution	Constant
	Cut-off frequency of the port	0 GHz
Excitation	Waveform	Gaussian modulated sinusoidal wave
	Spectrum	1-3 GHz, central frequency at 2 GHz
	Port distribution	Constant
Probes	Distance from the respective port	2 Δh

With the correct configuration in MEFiSTo-3D, we can run the simulation to get the S -parameters and the E -field in separate response windows. To verify the S -parameters, which we obtain directly from MEFiSTo, we utilize two references. The first reference is from another EM solver, HFSS, which is a 3D simulator in the frequency domain. Our second reference uses MATLAB to compute the S -parameters with (2.1) from the E -field response of MEFiSTo at the ports. We use the label “Matlab” referring to it in the figures. Figure 2.6 - Figure 2.9 show the comparison of the magnitude and phase of the S -parameters from these 3 methods for the inductive metallic obstacle.

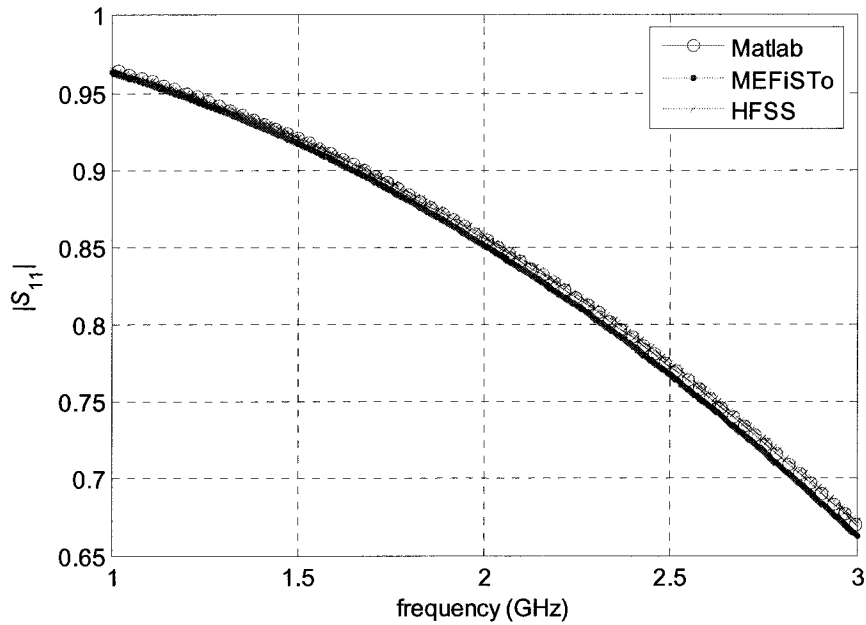


Figure 2.6. Magnitude of S_{11} of the inductive metallic obstacle.

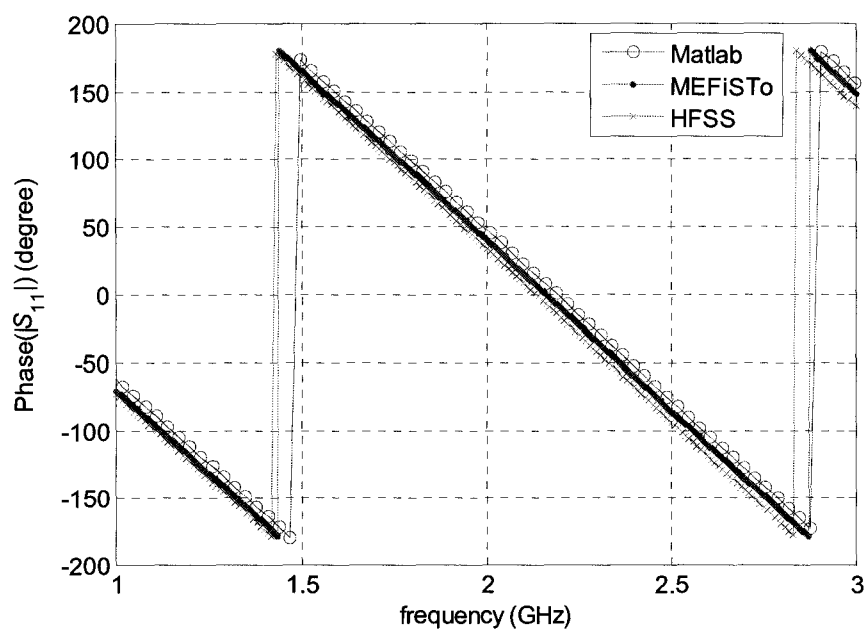


Figure 2.7. Phase of S_{11} of the inductive metallic obstacle.

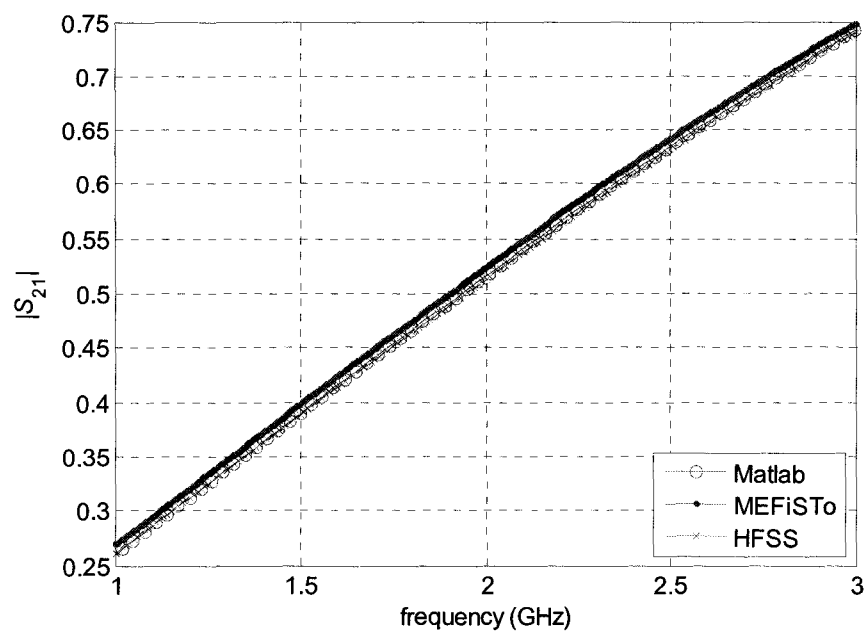


Figure 2.8. Magnitude of S_{21} of the inductive metallic obstacle.

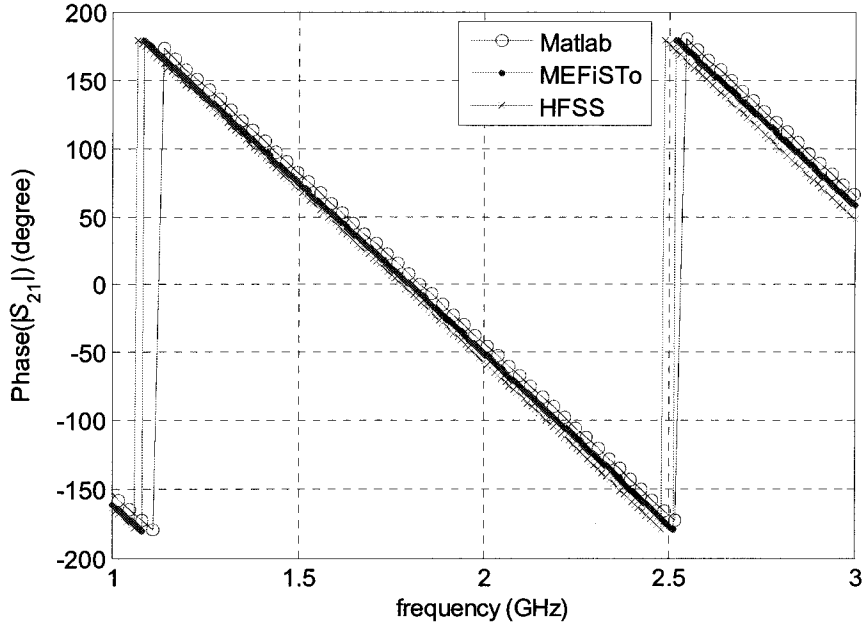


Figure 2.9. Phase of S_{21} of the inductive metallic obstacle.

From the comparison, we can see that the S -parameters derived from the 3 methods are close, which means that the result derived from MEFiSTo is acceptable.

The finite-difference derivatives of $|S_{11}|$ and $|S_{21}|$ in the inductive metallic obstacle example simulated with MEFiSTo with the cell size of 2 mm and 1 mm are shown in Figure 2.10 and Figure 2.11, respectively.

The “CFD”, “FFD” and “BFD” results are close for the cell size of 2 mm, and even closer for the cell size of 1 mm. It means that the selection of mesh size and other set up parameters in Table 2.1, like the total simulation time, are acceptable.

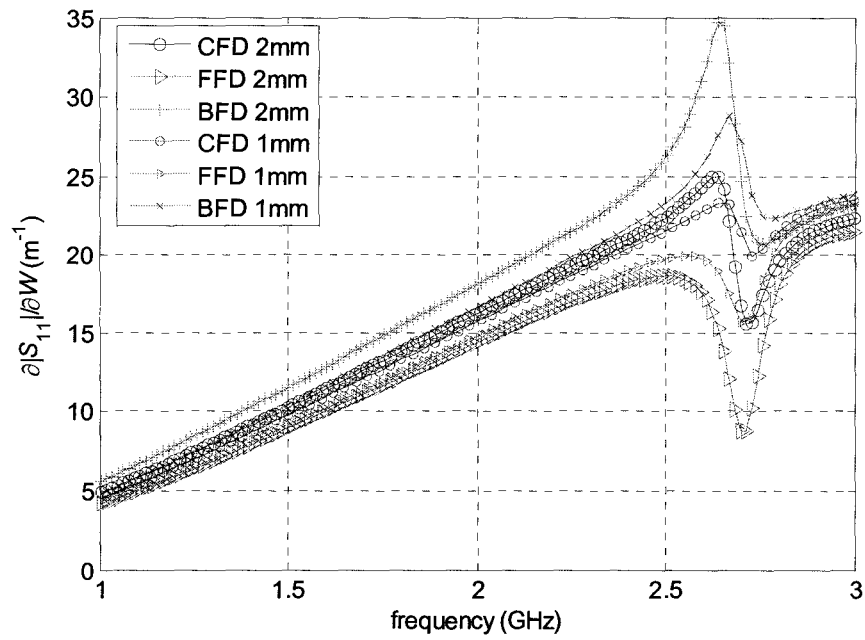


Figure 2.10. Derivatives of $|S_{11}|$ with respect to W in the inductive metallic obstacle example.

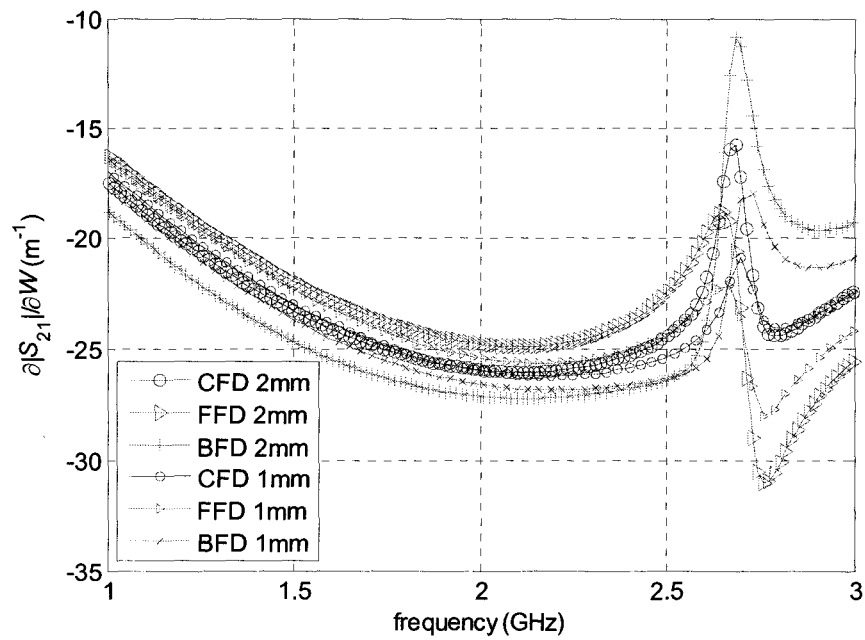


Figure 2.11. Derivatives of $|S_{21}|$ with respect to W in the inductive metallic obstacle example.

2.6.2 Single-resonator Filter

The structure of the single-resonator filter is given in Figure 2.12. The designable parameters are the length of the resonator D and the width of the septum W . $[D \ W]^T$

The dominant mode is a TE_{10} mode.

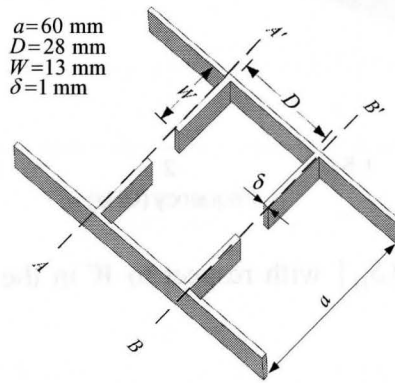


Figure 2.12. The single-resonator filter

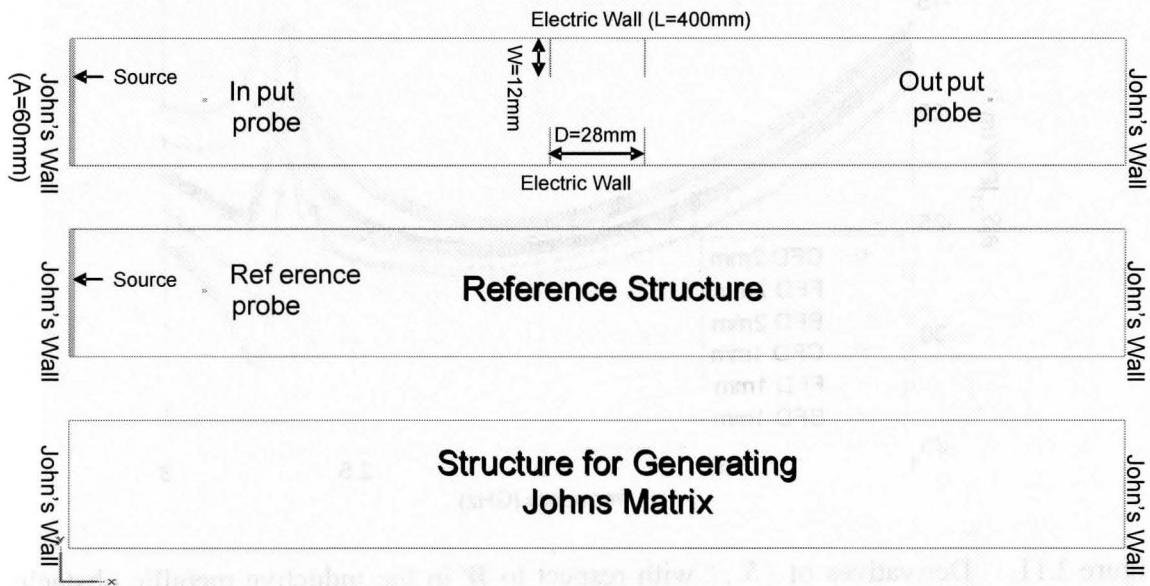


Figure 2.13 Top view of the single-resonator filter structure in MEFiSTo.

The top view of the structure in the edit window of MEFiSTo is shown in Figure 2.13. The setup of the MEFiSTo simulation of the inductive metallic obstacle example is summarized in Table 2.2

Table 2.2. Setup of the single-resonator filter simulation

Constant	Cell size Δh	1 mm
	Time step Δt	1.6678205 psec
Computational domain	Width of port a	60 mm ($60 \Delta h$)
	Length of the waveguide L_w	400 mm ($400 \Delta h$)
	Length of the resonator D	$28 \Delta h$
	Width of the septum W	$12 \Delta h$
	Computational domain in space	$400 \Delta h \times 60 \Delta h$
	Total time steps	$20,000 \Delta t$
Port	Boundary condition	Johns wall
	Modal distribution	Half-sine
	Cut-off frequency of the port	2.5 GHz
Excitation	Waveform	Gaussian modulated sinusoidal wave
	Spectrum	3-5 GHz, central frequency at 4 GHz
	Port distribution	Half-sine
Probes	Distance from the respective port	$20 \Delta h$

For the single-resonator filter example, we should setup the properties of their Johns wall boundaries as in Figure 2.14. The notation JM1L means left Johns matrix in structure 1, and JM2R means right Johns matrix in structure 2. For the right-hand port of the third structure denoted by “Self-Generating” JM3R, we should use “self-generating” in the property window and “Johns data” in the Johns Matrix window for the generation of the Johns matrix. For all other boundaries, JM1L, JM1R, JM2L, JM2R and JM3L, we should use “reference to another Johns matrix” in the property window and “response” in the Johns Matrix window with JM3R as the reference.

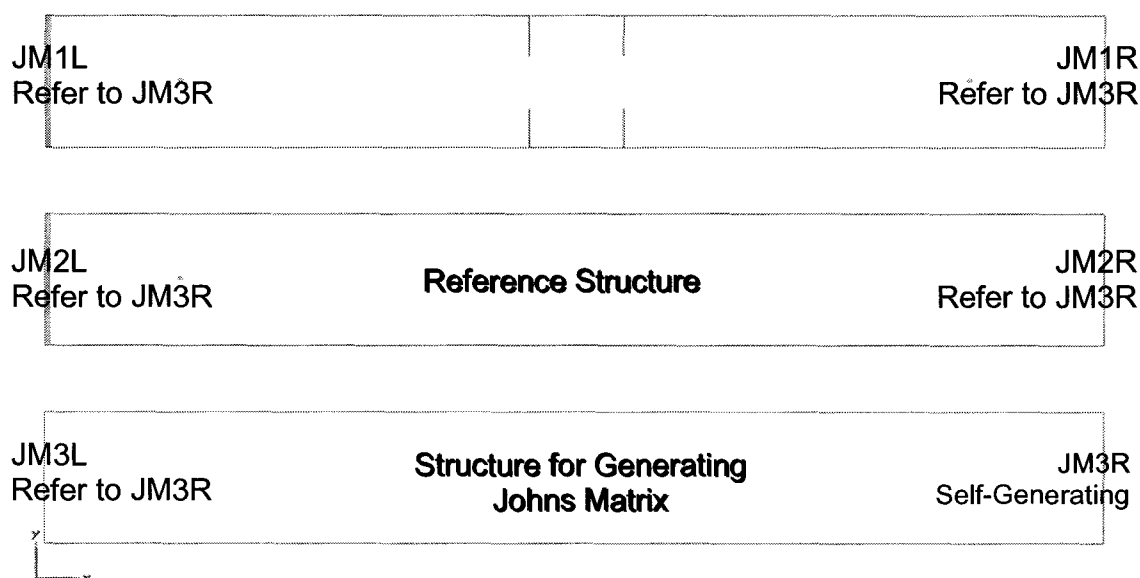


Figure 2.14. Johns boundaries of the single-resonator filter.

We compare the magnitude and phase of the S -parameters of the single-resonator filter generated by the 3 methods: computed in MATLAB from the E -field response of MEFiSTo, directly derived from MEFiSTo and directly from HFSS. The comparison is shown in Figure 2.15 - Figure 2.18. “Matlab”, “MEFiSTo” and “HFSS” denote the 3 methods, respectively.

From the comparison, we can see that the S -parameters derived from the 3 methods are close, which means that the result derived from MEFiSTo is acceptable. If we use the result of HFSS as a reference, we can conclude that the result computed by MATLAB using the field response of MEFiSTo is a little more accurate than the directly derived one, see the resonant frequency in Figure 2.15. We decide to use the MATLAB computed one for our future work.

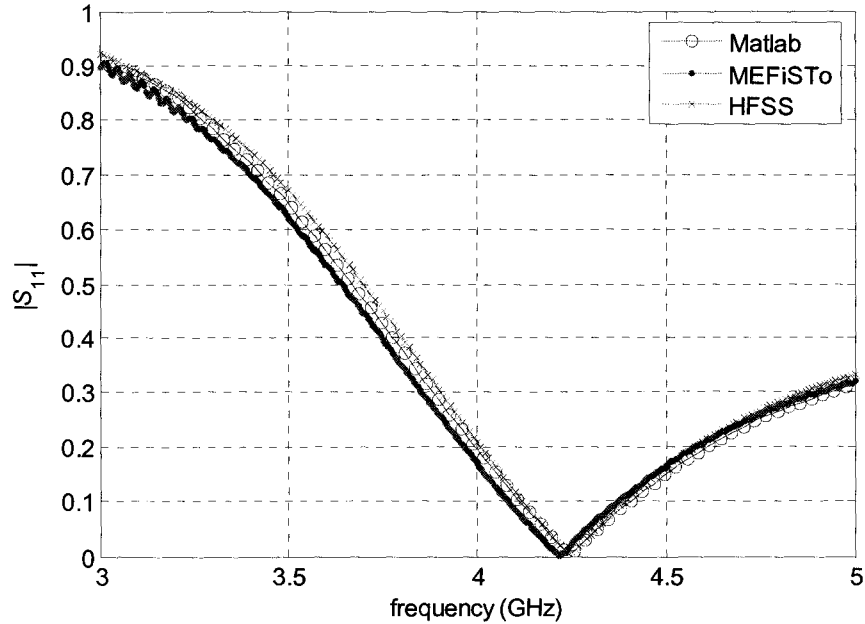


Figure 2.15. Magnitude of S_{11} of the single-resonator filter.

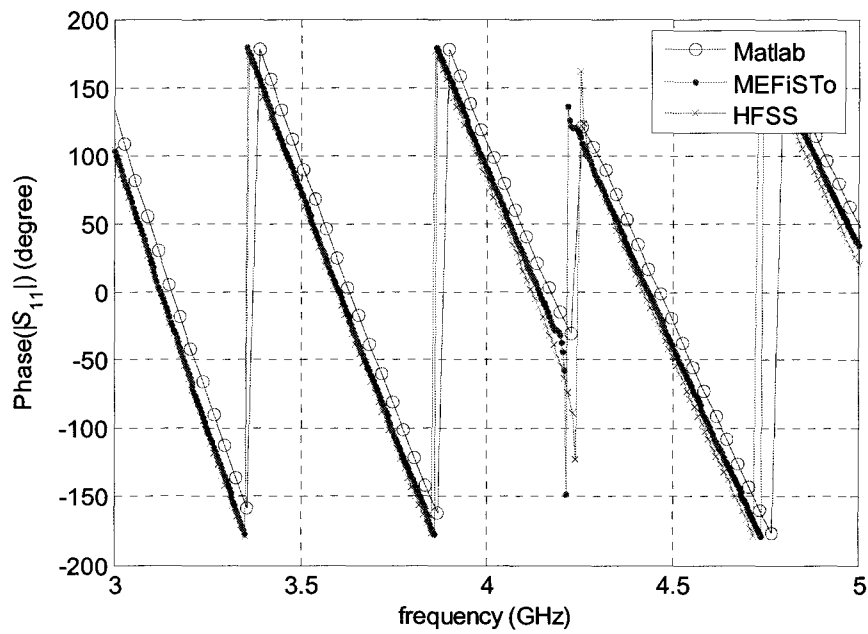


Figure 2.16. Phase of S_{11} of the single-resonator filter.

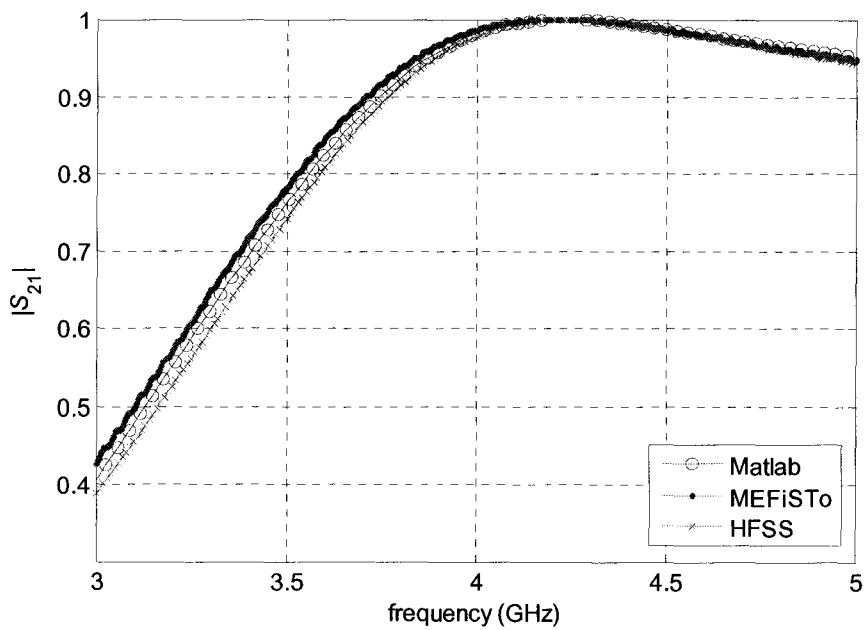


Figure 2.17. Magnitude of S_{21} of the single-resonator filter.

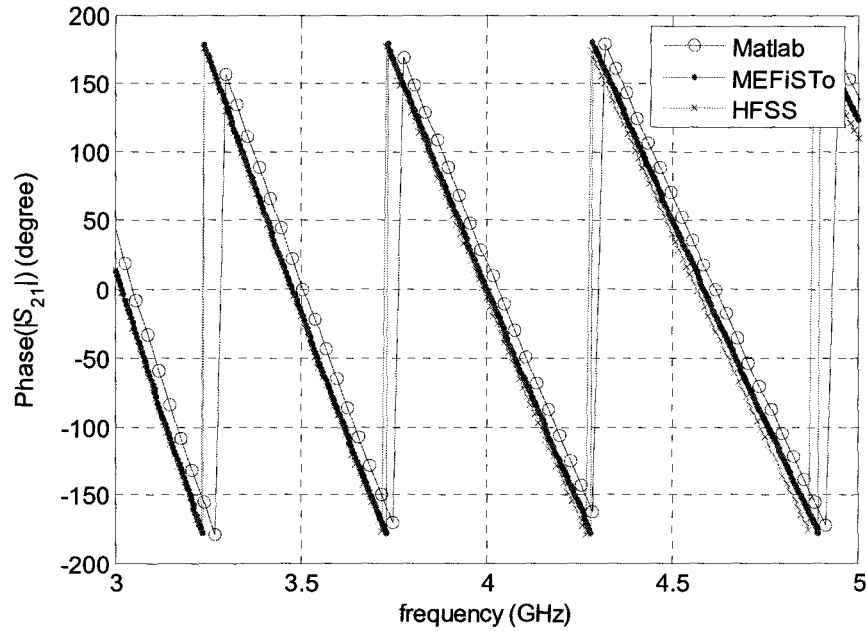


Figure 2.18. Phase of S_{21} of the single-resonator filter.

As for the phase, there will be great phase delays, if the distances between the observation points and the phase reference planes are long. They can be adjusted by the de-embedding technique described in subsection 2.3.

The finite-difference derivatives of $|S_{11}|$ and $|S_{21}|$ in the single-resonator filter example with the cell size of 2 mm and 1 mm are shown in Figure 2.19 and Figure 2.20, respectively. Similar conclusion can be drawn as in the last example: the mesh cell size is fine enough and the total simulation time is long enough.

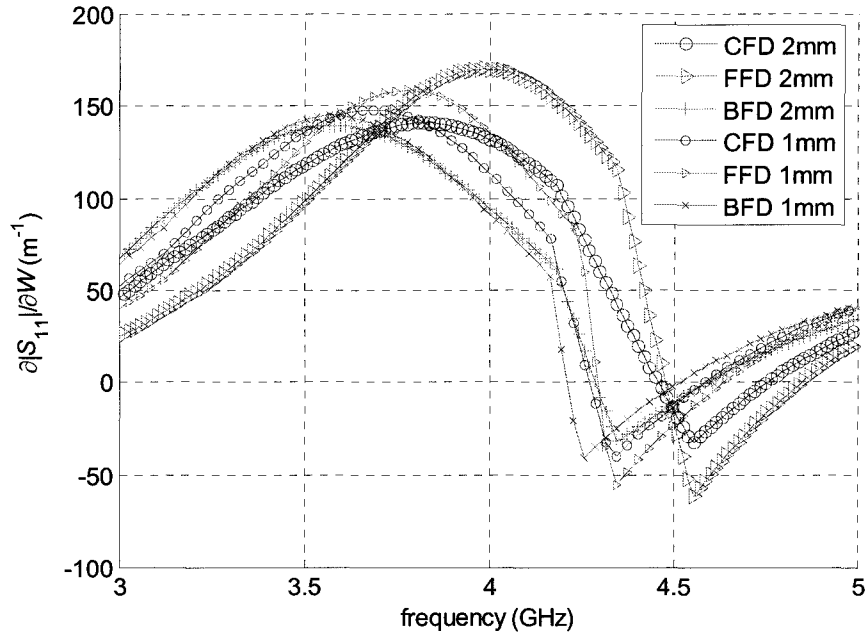


Figure 2.19. Derivatives of $|S_{11}|$ with respect to W in the single-resonator filter example.

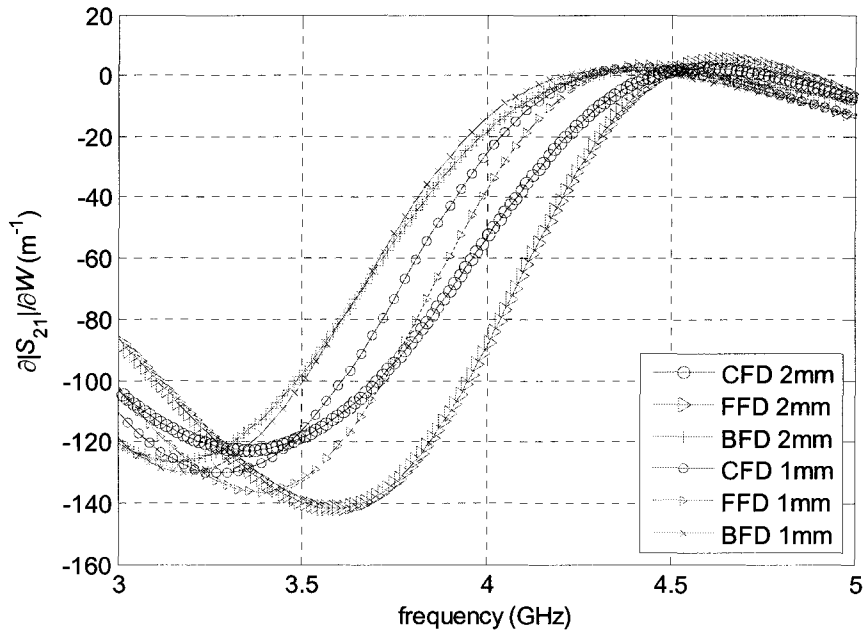


Figure 2.20. Derivatives of $|S_{21}|$ with respect to W in the single-resonator filter example.

2.7 Summary

The S -parameters derived from MEFiSTo are acceptable compared to the reference results from the MATLAB calculation and from HFSS. All the results are in agreement. This validates our set up for the simulations in MEFiSTo. If we regard the S -parameters of HFSS as the reference, the result calculated using the field response of MEFiSTo and our MATLAB code is a little more accurate than the one directly given by the solver.

From the plots of the FD sensitivity of the S -parameters, the cell size of the mesh is fine enough for the given examples. These derivative curves then can be used as reference sensitivities for verifying our sensitivity analysis with the adjoint variable methods (AVM).

2.8 References

- [1] MEFiSTo-3D[®] Pro v. 4, *User Guide and Operating Manual*, 6th ed., Faustus Scientific, Jan. 2003, <http://www.faustcorp.com/products/mefisto3dpro/> .
- [2] MATLAB[®] v. 7, The MathWorks, Inc.,
<http://www.mathworks.com/products/matlab/> .
- [3] HFSS[®] v. 9.0, Ansoft, <http://www.ansoft.com/products/hf/hfss/> .
- [4] N. Marcuvitz, *Waveguide Handbook*. London, UK: Peter Peregrinus Ltd., 1993 reprint, Chapter 2.

- [5] Y. Qian and T. Itoh, *FDTD Analysis and Design of Microwave Circuits and Antennas: Software and Applications*, Realize Inc., Tokyo, 1999.
- [6] K. S. Yee, "Numerical solution of initial boundary value problems involving Maxwell's equations in isotropic media," *IEEE Transactions on Antennas and Propagation*, vol. AP-14, pp.302-307, 1966.
- [7] Allen Taflov, *Computational Electrodynamics: The Finite-Difference Time-Domain Method*. Artech House, Inc., 1995.
- [8] Matthew N.O. Sadiku. *Numerical Techniques in Electromagnetics*. 2nd edition, 2001.

Chapter 3

TLM-BASED SELF-ADJOINT SENSITIVITY ANALYSIS

3.1 Introduction

We present a self-adjoint approach to S -parameter sensitivity computation with time-domain electromagnetic (EM) simulators based on the transmission-line matrix (TLM) discretization scheme. The method is applicable with any EM simulator, which can export either the electric field or the incident TLM voltages at user defined points. Our technique converts the electric and magnetic field solution into TLM voltages if the latter are not available. The S -parameter derivatives are computed as an independent post-process whose computational requirements are negligible compared to the full-wave system analysis. Adjoint simulations are not needed if the problem is homogeneous. Our approach is illustrated through waveguide problems solved with a commercial TLM solver.

We start by giving a concise summary of the general adjoint variable method (AVM) approach for TLM. The self-adjoint AVM algorithm for estimating the S -

parameter sensitivities at multi-frequency points is described afterwards. The method to convert field quantities to TLM incident impulses is then given in detail. The validation of the algorithm is carried out through 2D waveguide examples. Our self-adjoint S -parameter sensitivities are computed with respect to shape design parameters and are compared with finite-difference approximations. Good match is obtained between the two sets of data. The results are additionally verified with HFSS [1]. We discuss the CPU time and storage requirements and delineate the advantages and the limitations of the technique. We conclude with a summary.

3.2 Adjoint Variable Method for Time-domain TLM Method

The AVM offers an efficient way to perform sensitivity analysis, which uses only two simulations, of the original and the adjoint problems, to obtain the derivatives with respect to all designable parameters regardless of their number [2].

The AVM approach for the time-domain Transmission Line Modeling (TLM) is used to derive complex frequency-dependent S -parameter sensitivities commonly used in microwave design. For a structure with N_p ports, the technique requires additional N_p adjoint simulations to obtain the derivatives of the S -parameters with respect to all design parameters. A wideband excitation is utilized for all the adjoint simulations. Discrete Fourier Transform (DFT) is then employed to estimate the S -parameter sensitivities over the desired range of frequencies.

The AVM efficiently estimates the gradient of a response function with respect to the designable parameters $\mathbf{p} \in \mathbb{R}^n$ at a given set of values \mathbf{p}^0 . The real objective function is of the form

$$F = \int_0^{T_s} \psi(\mathbf{p}, \mathbf{V}) dt \quad (3.1)$$

where \mathbf{V} is the vector of continuous functions of time corresponding to the discrete set of incident impulses \mathbf{V}_k , $k=1, \dots, N_t$. Here, N_t is the number of time steps in the simulation.

One forward-running TLM step is given by

$$\mathbf{V}_{k+1} = \mathbf{C}\mathbf{S}\mathbf{V}_k + \mathbf{V}_k^S + \sum_{k'=0}^k \mathbf{G}(k-k')\mathbf{V}_{k'}^R \quad (3.2)$$

where \mathbf{V}_k and \mathbf{V}_k^R are the vectors of incident and reflected impulses, respectively. \mathbf{S} is the scattering matrix, and \mathbf{C} is the connection matrix. The vector \mathbf{V}_k^S is the original excitation vector. The matrix $\mathbf{G}(k)$ is the k th time layer of the three dimensional Johns matrix. $T_s = N_t \Delta t$ is the total simulation time.

The sensitivities of the objective function F with respect to all designable parameters can be obtained by simulating the backward-running adjoint system

$$\lambda_{k-1} = \mathbf{S}^T \mathbf{C}^T \lambda_k + \mathbf{S}^T \sum_{k'=k}^{N_t} \mathbf{G}^T(k'-k) \lambda_{k'} - \mathbf{V}_k^{S,\lambda}, \quad \lambda(T_s) = \mathbf{0} \quad (3.3)$$

where the adjoint excitation is

$$\mathbf{V}_k^{S,\lambda} = \Delta t (\partial \psi / \partial \mathbf{V})_{k\Delta t}. \quad (3.4)$$

The adjoint simulation (3.3) provides the adjoint state-variable vector λ at all time steps. With the solution of (3.2) and (3.3), the sensitivity of F with respect to the n th parameter can be expressed by [2]

$$\begin{aligned} \frac{\partial F}{\partial p_n} &= \frac{\partial^e F}{\partial p_n} - \int_0^{T_s} \lambda^T \frac{\Delta \mathbf{A}_n}{\Delta p_n} \mathbf{V} dt \approx \frac{\partial^e F}{\partial p_n} - \Delta t \sum_k \lambda_k^T \left(\frac{\Delta \mathbf{A}_n}{\Delta p_n} \mathbf{V}_k \right) \\ &= \frac{\partial^e F}{\partial p_n} - \Delta t \sum_{k=0}^{N_t} \lambda_k^T \boldsymbol{\eta}_k = \frac{\partial^e F}{\partial p_n} - \Delta t \sum_{k=0}^{N_t} \sum_{j \in \mathcal{S}_n} \tilde{\lambda}_{j,k}^p \boldsymbol{\eta}_{j,k}^q \end{aligned} \quad (3.5)$$

where $\Delta \mathbf{A}_n$ is the forward finite difference of the matrix $\mathbf{A} = (\mathbf{C}\mathbf{S} - \mathbf{I})/\Delta t$ due to a perturbation Δp_n in the n th parameter. The set \mathcal{S}_n contains the indices of the links at the p_n -related perturbation points [2]. The matrix $\Delta \mathbf{A}_n$ contains only few nonzero elements. It follows that we need to store only the vector $\lambda_{j,k}$, where at the j th node $\Delta \mathbf{A}_n$ is nonzero. Thus $\lambda_{j,k}$ contains only a small subset of the components of λ_k . The general expression for the m th component of the vector $\boldsymbol{\eta}_{j,k}$ is given by

$$\boldsymbol{\eta}_{j,k}^m = \frac{1}{\Delta p_n \Delta t} (\alpha V_{m,k+1}^R + \beta V_{l,k+1}^R) \quad (3.6)$$

where l is the index of the link connecting to the m th link. The parameters α and β are 0, -1 or 1, depending on the change of the connection of the m th link [2].

3.3 TLM-based Adjoint Variable Method for S -parameters

From the definition of the S -parameters in section 2.2, the S_{pq} derivative is determined by the derivative of the response \tilde{F}_{pq} :

$$\frac{\partial S_{pq}}{\partial p_n} = \sqrt{\frac{Z_q}{Z_p}} \frac{\partial \tilde{F}_{pq}}{\partial p_n} / \tilde{F}_{qref}, \quad n=1, 2, \dots, N_p. \quad (3.7)$$

Below, we focus on the sensitivity of the p th port output spectrum $\partial \tilde{F}_{pq} / \partial p_n$. The sensitivities of the real and imaginary parts of the output spectrum at a frequency f_m is given by [3]

$$\begin{aligned} \frac{\partial \operatorname{Re} \tilde{F}_{pq}(f_m)}{\partial p_n} &\approx -\Delta t \sum_{k=0}^{N_t} \tilde{\lambda}_{j,k}^{p,R}(f_m) \boldsymbol{\eta}_{j,k}^q \\ \frac{\partial \operatorname{Im} \tilde{F}_{pq}(f_m)}{\partial p_n} &\approx -\Delta t \sum_{k=0}^{N_t} \tilde{\lambda}_{j,k}^{p,I}(f_m) \boldsymbol{\eta}_{j,k}^q \end{aligned} \quad (3.8)$$

where $\boldsymbol{\eta}_{j,k}^q$ is computed from (3.6) with the solution of the original impulse of the j th link at the k th time step when the original excitation is applied at the q th port. $\tilde{\lambda}_{j,k}^{p,R}$ and $\tilde{\lambda}_{j,k}^{p,I}$ are the real and imaginary parts of $\tilde{\lambda}_{j,k}^p$, which is the predicted spectrum of the adjoint impulse of the j th link at the k th time step when the adjoint excitation is applied at the p th port. We derive its expression as follows.

The excitation applied to the j th node of the q th port at the k th time step is given by

$$\mathbf{V}_k^{s,j} = \frac{\mathbf{a}}{\|\mathbf{a}\|^2} E_q(j) h_0(k\Delta t), \quad q=1, 2, \dots, N_p \quad (3.9)$$

where $E_q(j)$ is the transversal mode distribution at the j th node of the q th port, and $h_0(k\Delta t)$ is the time sequence of the excitation of the original problem. The vector \mathbf{a}

relates the incident impulses of the observed field component by $E = \mathbf{a}^T \mathbf{V}$, where $\mathbf{a} = [0.5 \ 0.5 \ 0.5 \ 0.5]^T$ in the 2D case.

The sensitivities of the scattering parameter S_{pq} over the desired range of frequencies can be obtained by exciting the p th port of the same structure with the wideband adjoint excitation [3]

$$\mathbf{V}_n^{S,\lambda} = \frac{\mathbf{a}}{\|\mathbf{a}\|^2} E_p(j) h_a(n\Delta\tau) \quad (3.10)$$

where $\tau = n\Delta\tau = T_s - t$ is the time variable of the backward-running adjoint simulation. $h_a(n\Delta\tau)$ is the time waveform of the excitation of the adjoint problem. $E_p(j)$ is the transversal mode distribution at the j th node of the p th port.

For a structure where the dominant modes of the p th and q th port are the same $E_p(j) = E_q(j)$, we can derive a simple transformation from the original solution to the adjoint solution as follows.

For the frequency f_m , the corresponding complex spectral component of the excitation $h(\tau)$ is approximated by

$$\tilde{H}(f_m) \approx \sum_{n=1}^{N_t} h(n\Delta\tau) \exp[-2\pi j(m-1)(n-1)/N_t] \quad (3.11)$$

where $f_m = (m-1)\Delta f$, $\Delta f = 1/(N_t\Delta t)$. The corresponding complex spectral component of the adjoint impulse $\lambda_{j,k}^p$ is approximated by

$$\tilde{\lambda}_j^p(f_m) \approx \sum_{n=1}^{N_t} \lambda_{j,k}^p(n\Delta\tau) \exp[-2\pi j(m-1)(n-1)/N_t] \quad (3.12)$$

where $n = N_t - k$, $\Delta\tau = \Delta t$, Δt is the discrete time step.

Because of the assumed linearity of the medium, the predicted spectra of the adjoint impulses $\tilde{\lambda}_{j,k}^{p,R}$ and $\tilde{\lambda}_{j,k}^{p,I}$ due to the adjoint excitation in (3.10) at f_m can be expressed as

$$\begin{aligned}\tilde{\lambda}_{j,k}^{p,R}(k\Delta t) &= \Delta t \Delta s \|\mathbf{a}\|^2 \frac{|\tilde{\lambda}_j^p(f_m)|}{|\tilde{H}(f_m)|} \cos\left[2\pi f_m(-k)\Delta t + \angle\tilde{\lambda}_j^p(f_m) - \angle\tilde{H}(f_m)\right] \\ \tilde{\lambda}_{j,k}^{p,I}(k\Delta t) &= \Delta t \Delta s \|\mathbf{a}\|^2 \frac{|\tilde{\lambda}_j^p(f_m)|}{|\tilde{H}(f_m)|} \cos\left[2\pi f_m(-k)\Delta t + \angle\tilde{\lambda}_j^p(f_m) - \angle\tilde{H}(f_m) - \pi/2\right]\end{aligned}\quad (3.13)$$

where Δs is the area of a port surface element; $\Delta s = \Delta l^2$ in the 2D case. The vector \mathbf{a} is the same as in (3.9). The result for $\tilde{\lambda}_{j,k}^{p,R}$ and $\tilde{\lambda}_{j,k}^{p,I}$ is substituted in (3.8) to calculate the sensitivities of the output spectrum at f_m . Finally, we use (3.7) to compute the sensitivities of the S -parameters at the desired set of frequency points.

3.4 TLM-based Self-adjoint Sensitivity Theory

With a commercial TLM solver, we can not always perform backward-running simulation as required by the TLM-AVM approach above. Moreover, for a number of responses, the adjoint simulations can be avoided. This case is addressed by the self-adjoint approach, which obtains the adjoint impulses in [3] from the forward-running simulations of the original problem.

For lossless, homogenous and isotropic structures, the TLM S -parameter analysis is a self-adjoint problem. An isomorphism is established between the adjoint problem and

the corresponding transformed original problem. The adjoint TLM impulses needed at every time step are determined from the original TLM impulses. The additional N_p adjoint simulations are thus eliminated [4].

For a lossless and homogenous problem, the dielectric properties are the same in all nodes. In this case, the nodal scattering matrix satisfies

$$\mathbf{S}^T = \mathbf{S} = \mathbf{S}^{-1}. \quad (3.14)$$

Using (3.14) and with the symmetry of the Johns matrix at each time step, equation (3.3) can be rewritten as

$$\lambda_{k-1} = \mathbf{S} \mathbf{C} \lambda_k + \mathbf{S} \sum_{k'=k}^{N_t} \mathbf{G}(k'-k) \lambda_{k'} - \mathbf{V}_k^{S,\lambda}, \quad \lambda(T_s) = \mathbf{0}. \quad (3.15)$$

Using the transformation

$$\mathbf{V}_{j,k}^R = \mathbf{S}^j \mathbf{V}_{j,k} \quad (3.16)$$

the original simulation (3.2) can be expressed in terms of the reflected impulses as

$$\mathbf{V}_{k+1}^R = \mathbf{S} \mathbf{C} \mathbf{V}_k^R + \mathbf{S} \sum_{k'=0}^k \mathbf{G}(k-k') \mathbf{V}_{k'}^R + \mathbf{V}_k^{S,R}, \quad \mathbf{V}_0^R = \mathbf{0}. \quad (3.17)$$

Comparing (3.15) and (3.17), if we assume that the original and the adjoint simulations are excited with the same temporal and spatial distribution, $h_0(t) = h_a(\tau)$ and $E_p(j) = E_q(j)$, we have a relationship between the adjoint and original impulses as

$$\lambda(\tau) = -\mathbf{V}^R(t), \quad \lambda_{N_t-k} = -\mathbf{V}_k^R. \quad (3.18)$$

It follows that the adjoint impulses λ_{N_t-k} obtained from (3.15) by exciting the p th port can be deduced from the values of the original impulses \mathbf{V}_k^R obtained from the forward-

running simulation (3.17) when the same p th port is excited. The additional N_p adjoint simulations can be eliminated.

3.5 Conversion from Field Quantities to Incident Impulses

Another difficulty for the AVM-TLM algorithm in the framework of commercial software is that normally the software provides only the responses of the field quantities of each node while we need incident impulses at certain links to get the sensitivities, see (3.8). MEFiSTo-3D Pro [5] does provide the incident impulses, which simplifies our work; however, to get the reflected impulses for the proposed AVM algorithm; we need more probes than the conversion algorithm we adopt now. In this section, we explain the method to derive the incident or reflected impulses needed in the AVM algorithm from the field quantities, which makes our algorithm efficient as well as generally applicable to a variety of time-domain simulators.

We illustrate the conversion method using the 2D TLM shunt node, as in Figure 2.3 in section 2.5 [6]. The 2D mode in the commercial solver MEFiSTo-3D is discretized in the same way. To get the impulses at a certain link, we need the E and H field components at that node and the E field components at its adjacent nodes.

For instance, to get the reflected voltage at the 2nd link of the central node at the n th time step ${}_nV_2^R(i, j)$, we need the E_z field components at the points (i, j) and

$(i, j+1)$, and the H_y field component at (i, j) . The algorithm in discrete form is expressed as follows:

$$\begin{aligned}
 {}_nE_z^+(i+1/2, j) &= -{}_{n-1}E_z^+(i+1/2, j) + {}_nE_z(i, j) + {}_nE_z(i+1, j) \\
 {}_nE_z^-(i+1/2, j) &= -{}_{n-1}E_z^-(i+1/2, j) + {}_nE_z(i, j) - {}_nE_z(i+1, j) \\
 {}_nV_4^R(i, j) &= [{}_nE_z^+(i+1/2, j) + {}_nE_z^-(i+1/2, j)]/2 \\
 {}_nV_2^R(i, j) &= {}_nV_4^R(i, j) + {}_nH_y(i, j) \cdot Z_L
 \end{aligned} \tag{3.19}$$

where $Z_L = \sqrt{2\mu/\varepsilon}$ is the intrinsic impedance of the 2D TLM mesh link. In (3.19), the first two equations are updated iteratively to get the intermediate variables E_z^+ and E_z^- . Then we can compute the reflected voltage at the 4th link V_4^R . Using H_y and V_4^R , we finally obtain V_2^R , which is needed in (3.8) and (3.12). The reflected impulses at other links can be derived similarly. The incident impulses can be derived from the reflected impulses with the scattering and connection matrices.

3.6 Validation Examples

The examples focus on the sensitivity calculations with respect to the shape parameters in 2-D waveguide (in the dominant TE_{10} mode) problems. We set “2D mode” editor and “GSCN (Generalized Symmetrical Condensed Node) mesh for H -plane” in MEFiSTo-3D Pro for the simulation. After we set the cell size Δh and define the mesh, the discrete time step Δt is determined automatically by the software, so that $q = \Delta h/c\Delta t = 2$. The sources are located next to the port boundaries. The observation points are located 2 cells away from the respective port boundaries.

These examples have been analyzed with the self-adjoint TLM-AVM algorithm and an in-house TLM solver [3]; however, this time we use the commercial solver MEFiSTo and its field solution instead of the incident voltages.

In all plots, the derivative curves obtained with our time-domain self-adjoint sensitivity analysis approach are marked as TLM-SASA, while the curves obtained through parameter perturbations and finite differencing of the S -parameters are marked as BFD, CFD and FFD for the backward, central, and forward finite differences, respectively. Response finite differences are used with both commercial solvers, MEFiSTo-3D Pro and HFSS, in order to acquire reference sensitivity curves and compare them with the TLM-SASA results.

3.6.1 Inductive Metallic Obstacle

The structure of the inductive metallic obstacle in a parallel-plate waveguide is given in Figure 2.4. The setup of the MEFiSTo simulation is shown in Table 2.1. The designable parameters are the dimensions of the obstacle $[D \ W]^T$. The probes whose field solution should be recorded for AVM calculation are around the perturbation boundaries. The probe fields we need to record and the TLM impulses, which we calculate with the conversion method in section 3.5, are illustrated in Figure 3.1, where we assume an increase of the width W . The case of increasing the length D is similar.

The sensitivities of $|S_{11}|$ and $|S_{21}|$ with respect to D and W are presented in Figure 3.2, Figure 3.3, Figure 3.4 and Figure 3.5, respectively.

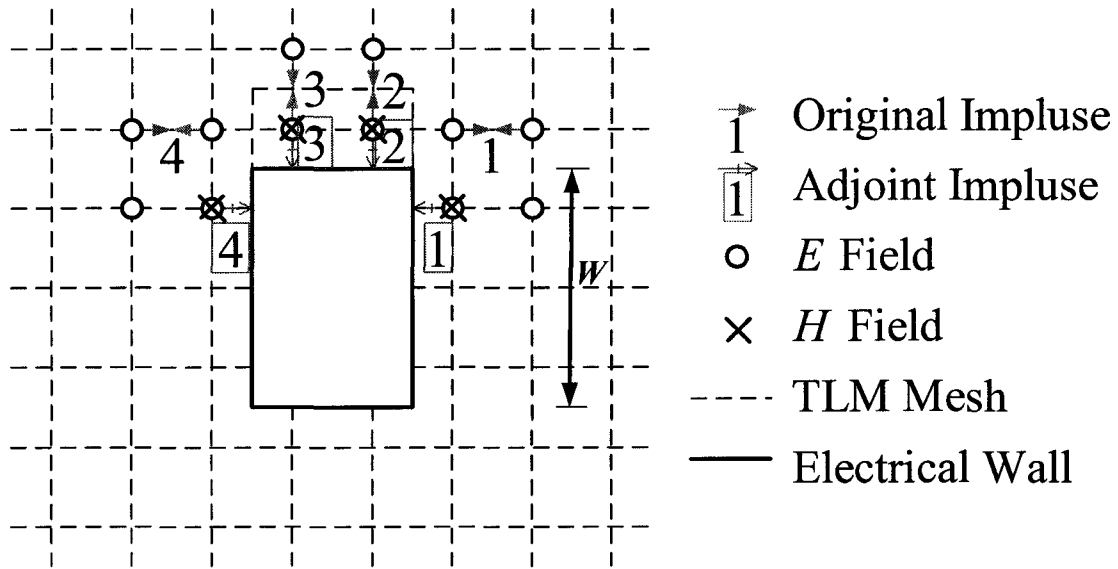


Figure 3.1. TLM-based AVM probes at the obstacle boundaries (assume increasing W) in the metallic obstacle example.

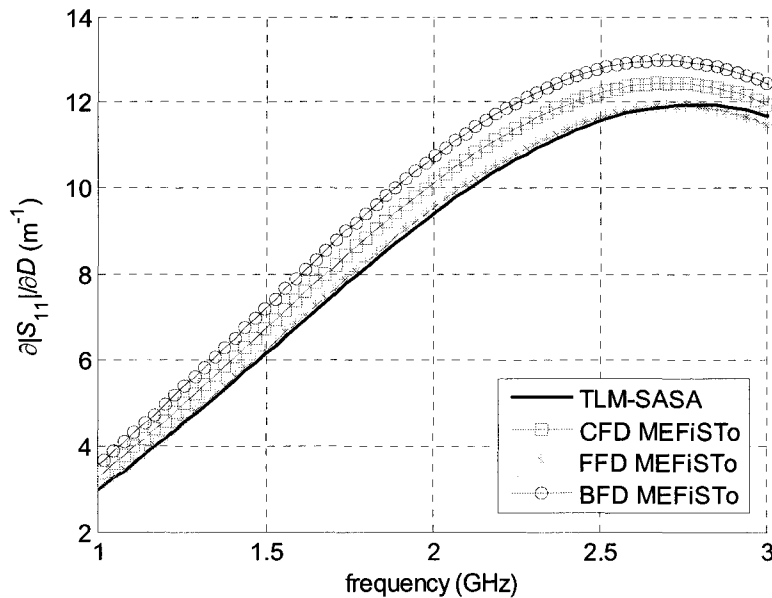


Figure 3.2. Derivatives of $|S_{11}|$ with respect to D in the inductive metallic obstacle example.

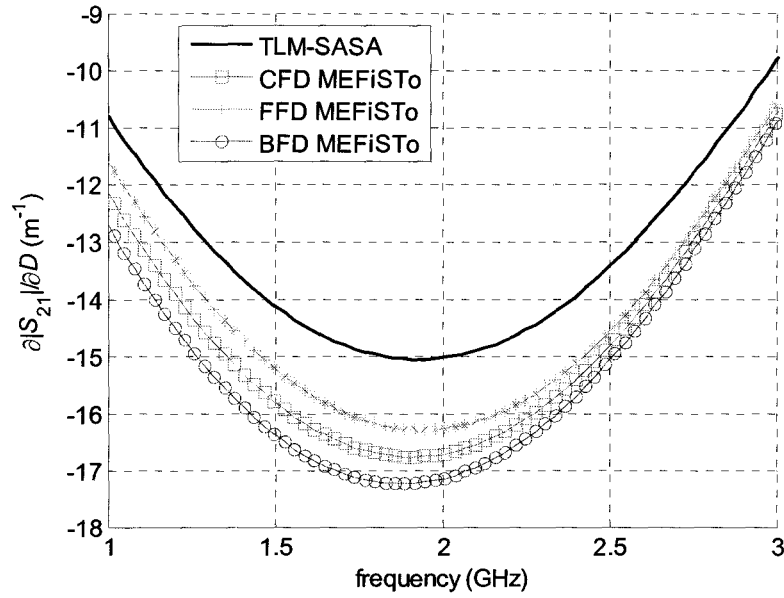


Figure 3.3. Derivatives of $|S_{21}|$ with respect to D in the inductive metallic obstacle example.

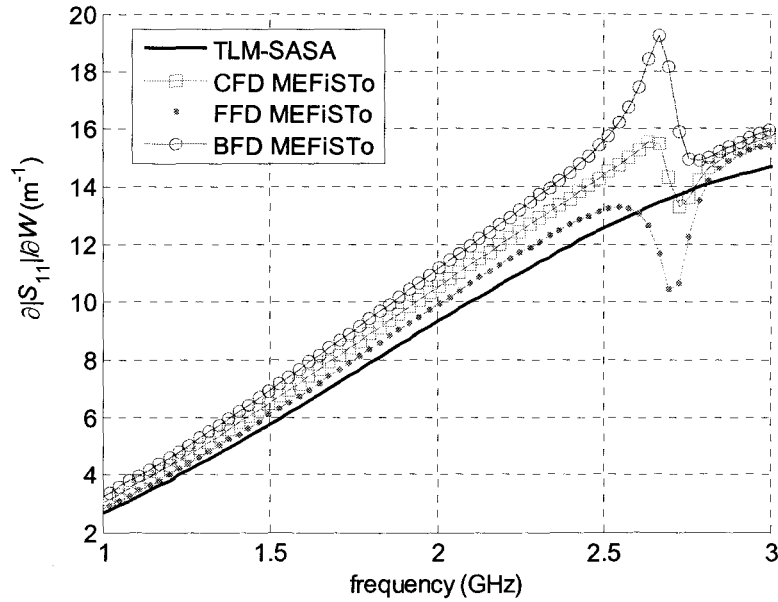


Figure 3.4. Derivatives of $|S_{11}|$ with respect to W in the inductive metallic obstacle example.

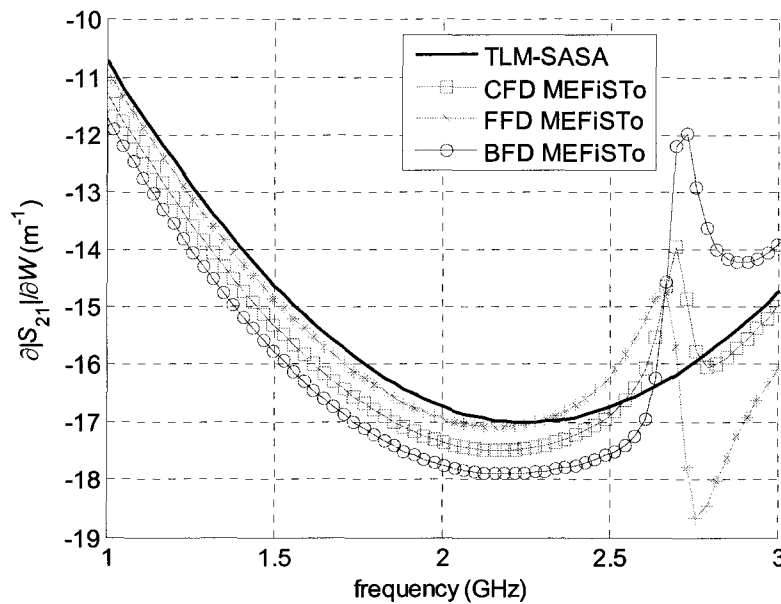


Figure 3.5. Derivatives of $|S_{21}|$ with respect to W in the inductive metallic obstacle example.

3.6.2 Single-resonator Filter

The structure of the single-resonator filter is shown in Figure 2.12. The setup of the MEFiSTo simulation is shown in Table 2.2. The designable parameters are the length of the resonator D and the width of the septum W : $[D \ W]^T$. The probe field and the TLM impulses needed are illustrated in Figure 3.6 and Figure 3.7, when we assume increasing length of the resonator D and its septum width W , respectively.

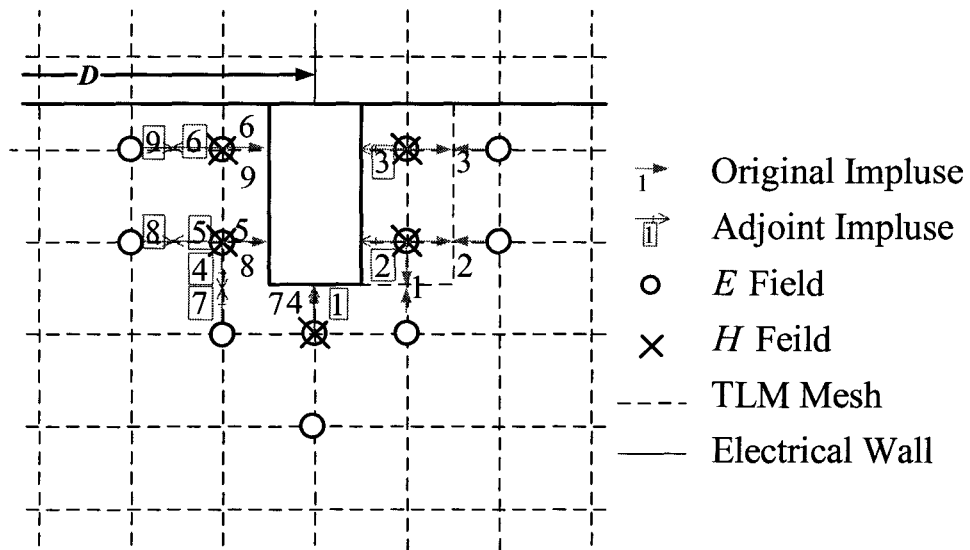


Figure 3.6. TLM-based AVM probes at the right septum (assume increasing D) in the single-resonator filter example.

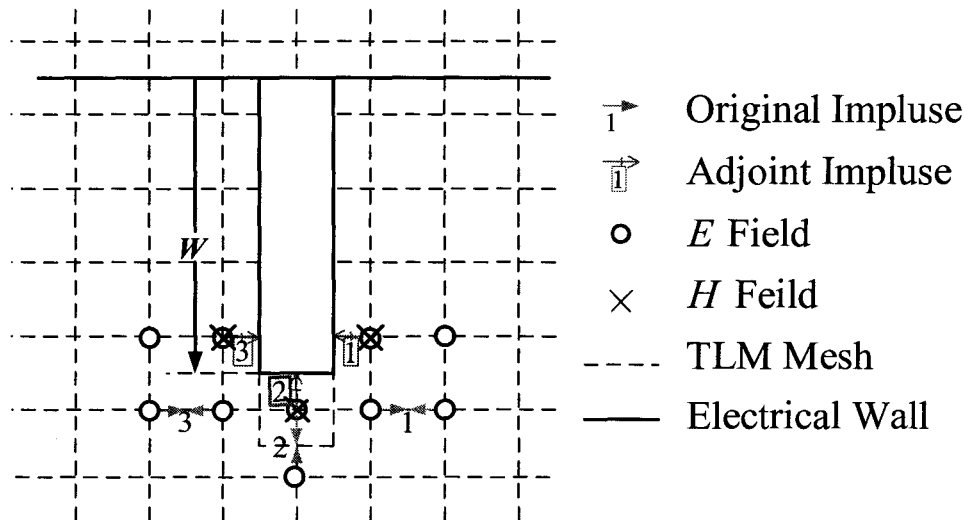


Figure 3.7. TLM-based AVM probes at the right septum (assume increasing W) in the single-resonator filter example.

The sensitivities of $|S_{11}|$ and $|S_{21}|$ with respect to D and W are presented in Figure

3.8, Figure 3.9, Figure 3.10 and Figure 3.11, respectively.

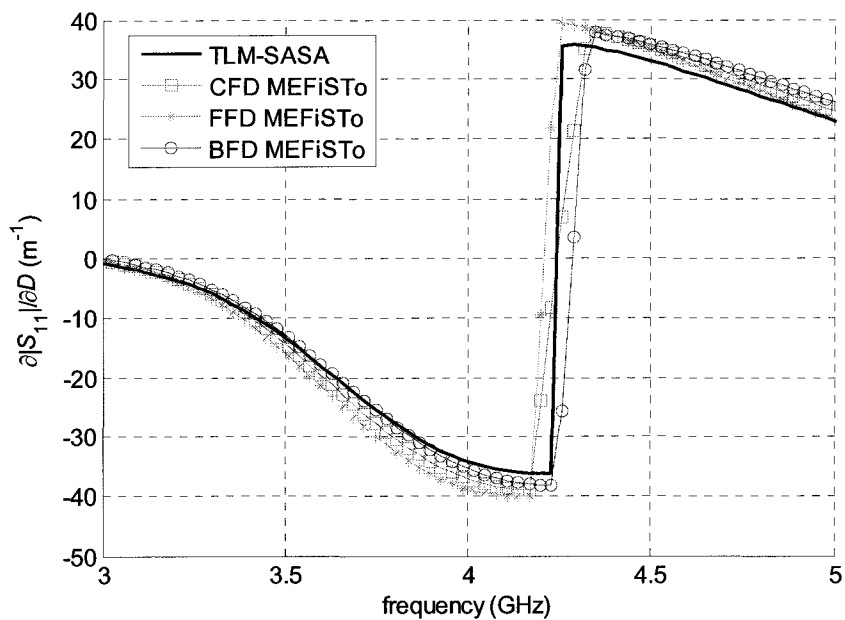


Figure 3.8. Derivatives of $|S_{11}|$ with respect to D in the single-resonator filter example.

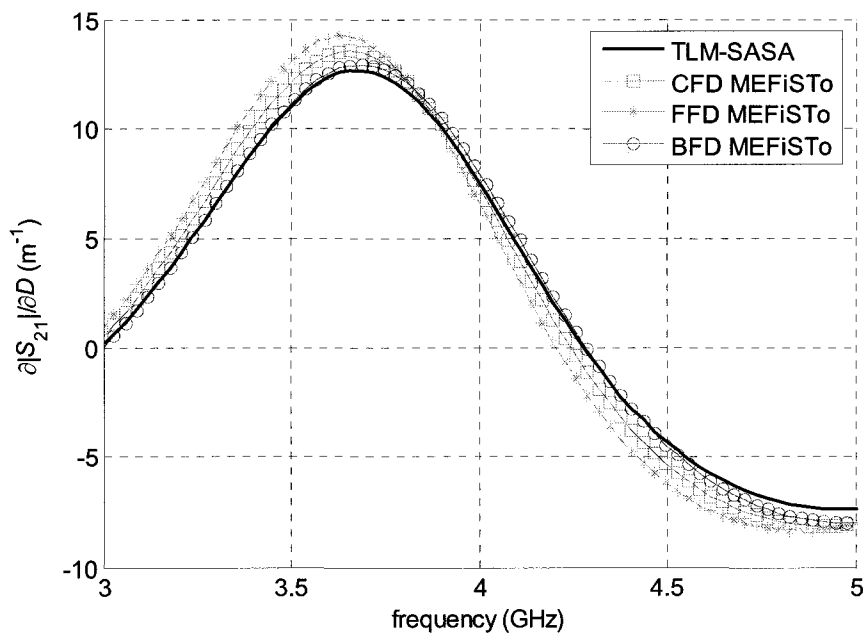


Figure 3.9. Derivatives of $|S_{21}|$ with respect to D in the single-resonator filter example.

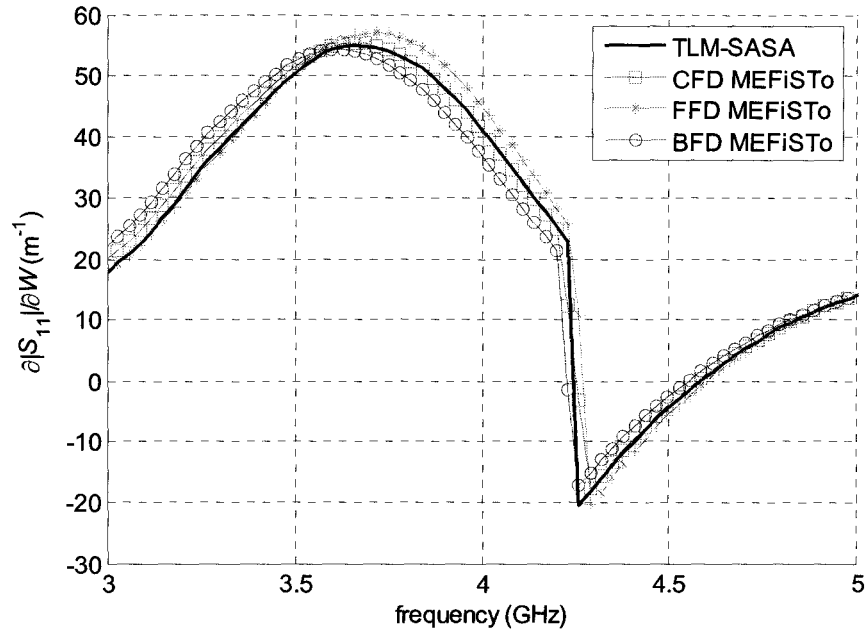


Figure 3.10. Derivatives of $|S_{11}|$ with respect to W in the single-resonator filter example.

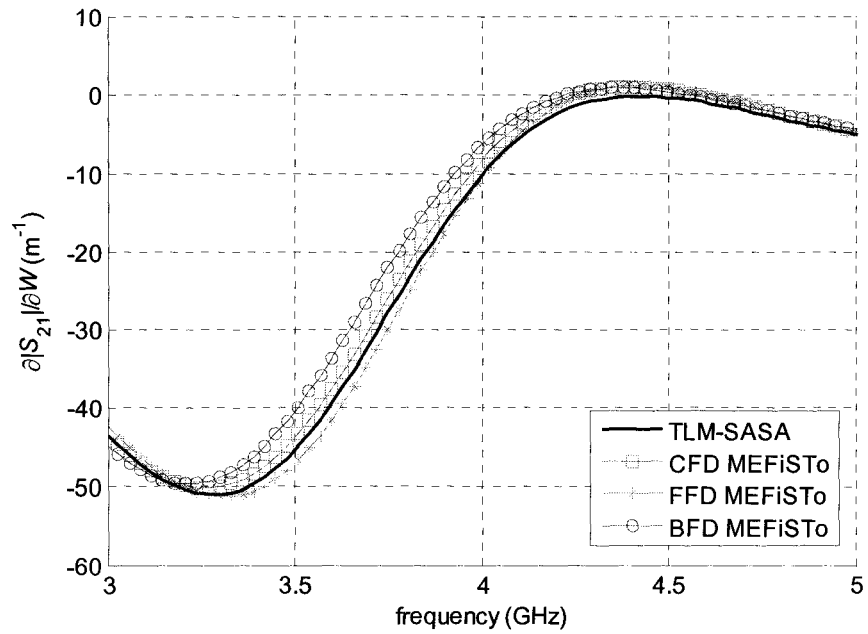


Figure 3.11. Derivatives of $|S_{21}|$ with respect to W in the single-resonator filter example.

3.6.3 *H*-plane Filter

The six-resonator *H*-plane filter and its nominal design are shown in Figure 3.12. The designable parameters are the widths of the septa and the lengths of the resonators $[W_1 \ W_2 \ W_3 \ W_4 \ L_1 \ L_2 \ L_3]$. The *S*-parameters of the nominal design computed from the field solution of MEFiSTo and those computed by HFSS are compared in Figure 3.13. The setup of the MEFiSTo simulation is summarized in Table 3.1. The AVM probes needed are similar to those in the single-resonator filter example, as in Figure 3.6 and Figure 3.7.

With a single MEFiSTo-3D simulation, we obtain the *S*-parameters and their derivatives with respect to all 7 design parameters, while to obtain the same results with central finite differences, we need 14 more simulations.

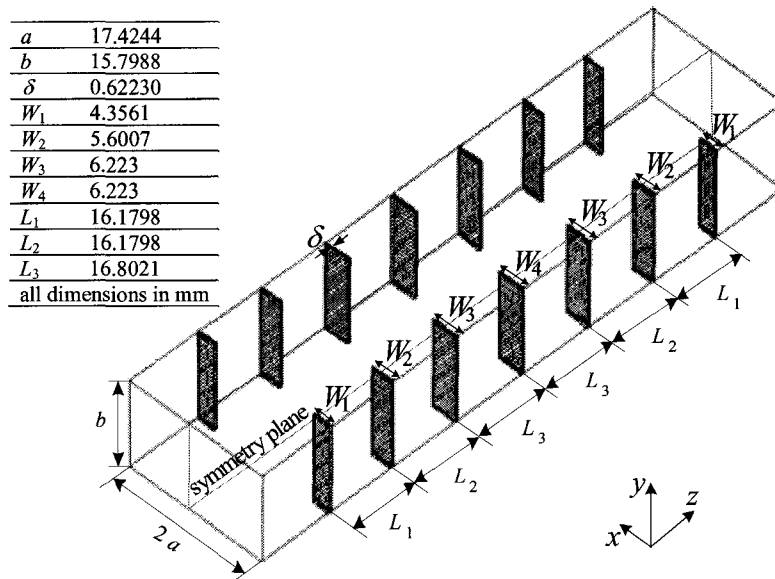


Figure 3.12. The six-resonator *H*-plane filter and its nominal design.

Table 3.1. Setup of the H -plane filter simulation

Constant	Cell size Δh	0.6223 mm
	Time step Δt	1.0378847 psec
Computational domain	Width of port 2 a	34.8488 mm ($56 \Delta h$)
	Length of the waveguide L_w	435.561 mm ($700 \Delta h$)
	Length of the resonators $[L_1 \ L_2 \ L_3]$	$[26\Delta h \ 26\Delta h \ 27\Delta h]$
	Width of the septa $[W_1 \ W_2 \ W_3 \ W_4]$	$[7\Delta h \ 9\Delta h \ 10\Delta h \ 10\Delta h]$
	Computational domain in space	$700 \Delta h \times 56 \Delta h$
	Total time steps	20,000 Δt
Port	Boundary condition	Johns wall
	Modal distribution	Half-sine
	Cut-off frequency of the port	4.3 GHz
Excitation	Waveform	Gaussian modulated sinusoidal wave
	Spectrum	5-10 GHz, central frequency at 7.5 GHz
	Port distribution	Half-sine
Probes	Distance from the respective port	$20 \Delta h$

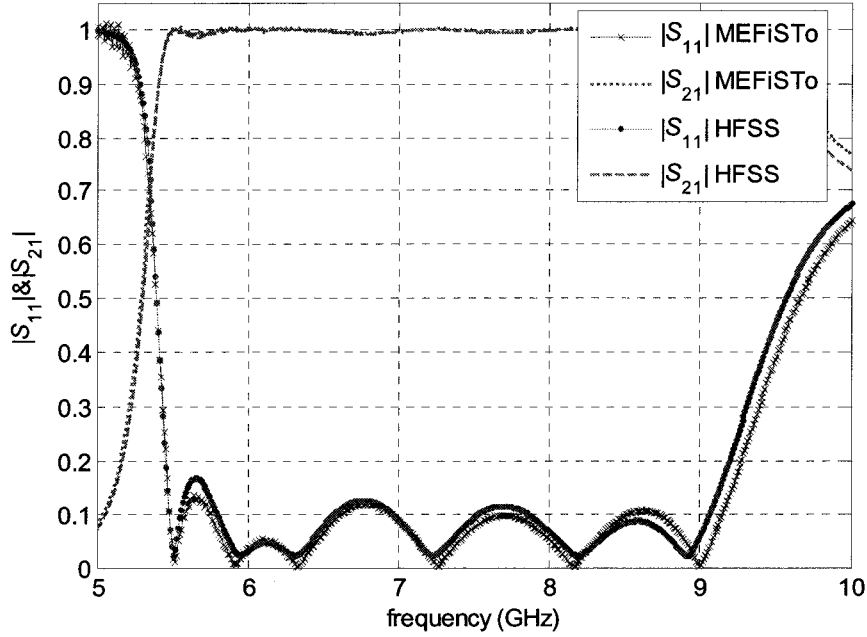


Figure 3.13. S -parameters of the six-resonator H -plane filter.

The derivatives of $|S_{11}|$ and $|S_{21}|$ of the H -plane filter at 7 GHz with respect to L_1 for a parameter sweep of L_1 are presented in Figure 3.14 and Figure 3.15, respectively. The derivatives of $|S_{11}|$ and $|S_{21}|$ with respect to the septum width W_4 for a parameter sweep of W_4 are presented in Figure 3.16 and Figure 3.17, respectively. All other parameters are at the nominal values as in Figure 3.12.

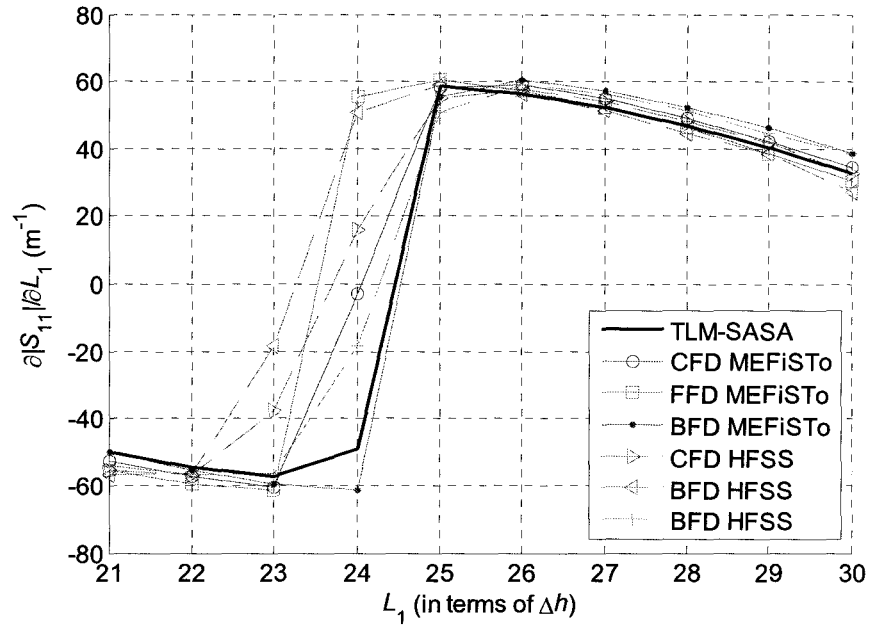


Figure 3.14. Derivatives of $|S_{11}|$ with respect to L_1 in the H -plane filter example.

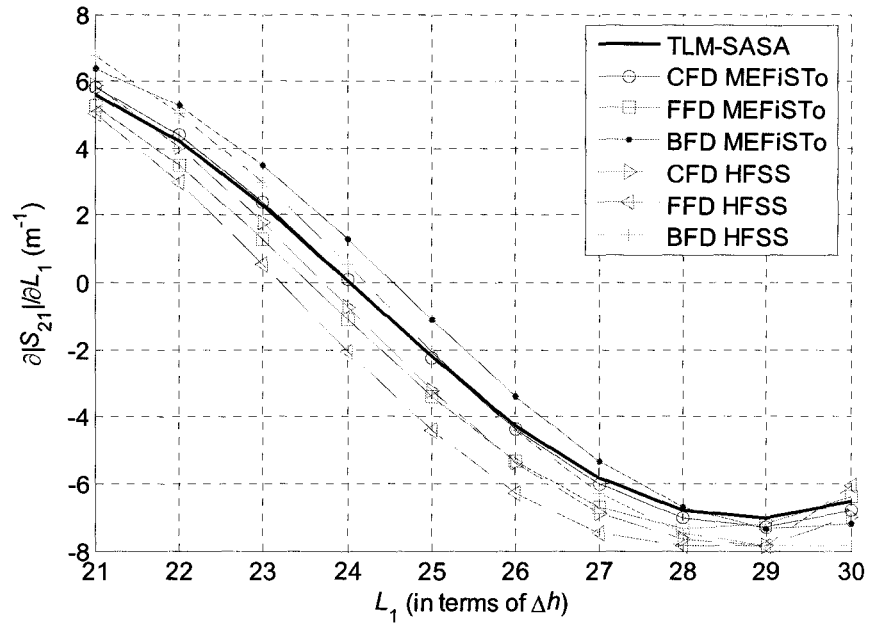


Figure 3.15. Derivatives of $|S_{21}|$ with respect to L_1 in the H -plane filter example.

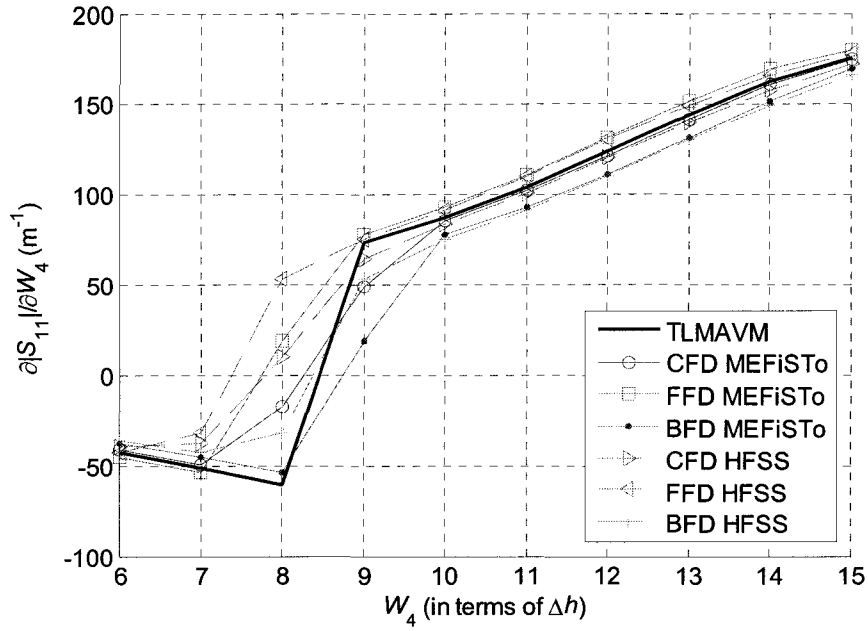


Figure 3.16. Derivatives of $|S_{11}|$ with respect to W_4 in the H -plane filter example.

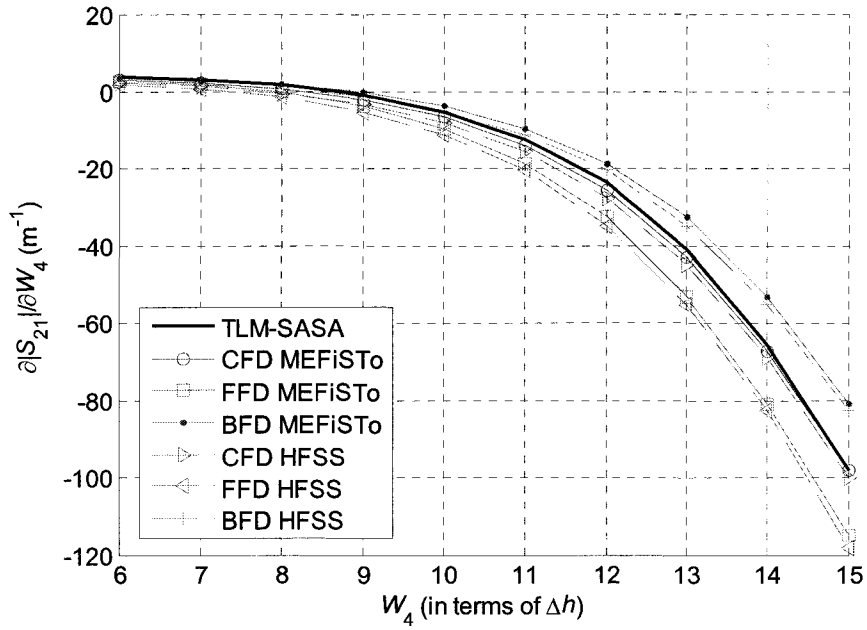


Figure 3.17. Derivatives of $|S_{21}|$ with respect to W_4 in the H -plane filter example.

3.6.4 Single-section Waveguide Impedance Transformer

The single-section waveguide impedance transformer [7] is shown in Figure 3.18. The designable parameters are the dimensions of the matching section $[W \ L]^T$. The S -parameters of the nominal design computed from the field solution of MEFiSTo and by HFSS are compared in Figure 3.19. The setup of the MEFiSTo simulation is summarized in Table 3.2. The AVM probes needed are similar to those in the metallic obstacle example, as in Figure 3.1.

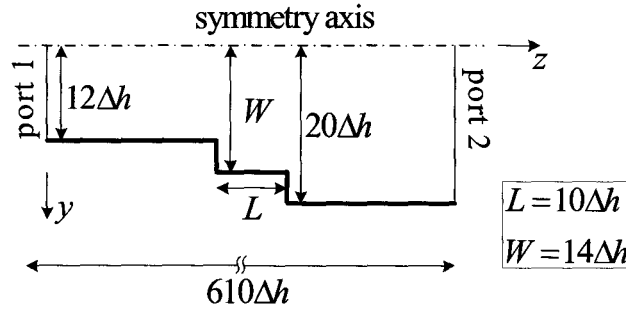


Figure 3.18. The single-section waveguide impedance transformer.

Table 3.2. Setup of the single-section waveguide impedance transformer simulation

Constant	Cell size Δh	1.26 mm
	Time step Δt	2.1014538 psec
Computational domain	Width of port 1 a_1	30.24 mm ($24 \Delta h$)
	Width of port 2 a_2	50.4 mm ($40 \Delta h$)
	Length of the waveguide L_w	768.6 mm ($610 \Delta h$)
	Lengths of the matching section L	$10 \Delta h$
	Half width of the matching section W	$14 \Delta h$
	Computational domain in space	$700 \Delta h \times 56 \Delta h$
	Total time steps	$20,000 \Delta t$
Port	Boundary condition	Johns wall
	Modal distribution	Half-sine
Excitation	Cut-off frequency of the port 1	4.957 GHz
	Cut-off frequency of the port 2	2.974 GHz
	Waveform	Gaussian modulated sinusoidal wave
	Spectrum	6-8 GHz, central frequency at 7 GHz
	Port distribution	Half-sine
Probes	Distance from the respective port	$2 \Delta h$

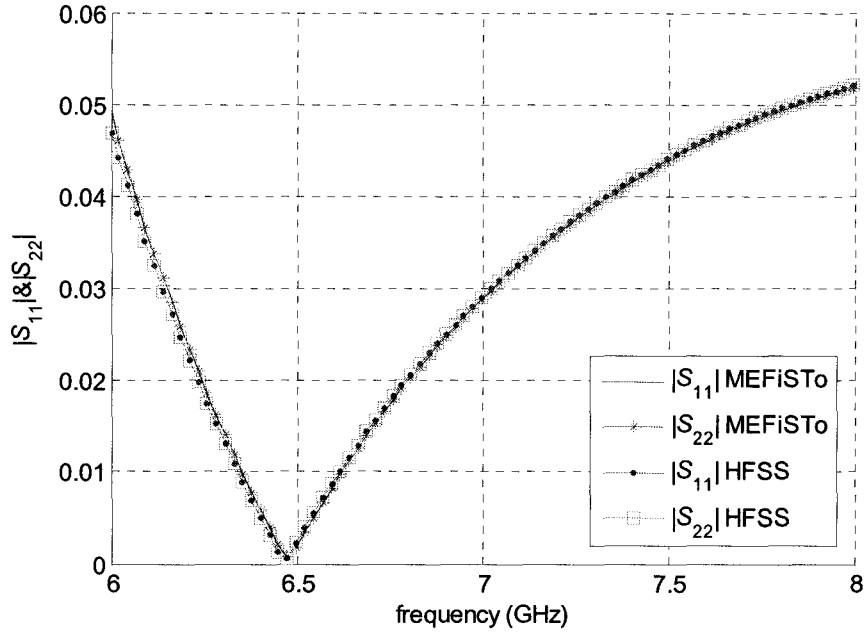


Figure 3.19. S -parameters of the single-section waveguide impedance transformer.

The S -parameter curves in Figure 3.19 show that the nominal design is optimal at about $f=6.48$ GHz. The two ports of the impedance transformer have different wave impedances. Thus, the computation of S_{21} and S_{12} as well as the computation of their derivatives require their values at each frequency of interest. $Z_1^{\text{TE}_{10}}$ and $Z_2^{\text{TE}_{10}}$ are computed analytically:

$$\frac{Z_1^{\text{TE}_{10}}}{Z_2^{\text{TE}_{10}}} = \sqrt{\left(\frac{w}{c_0}\right)^2 \varepsilon_{r2} - \left(\frac{\pi}{a_2}\right)^2} \bigg/ \sqrt{\left(\frac{w}{c_0}\right)^2 \varepsilon_{r1} - \left(\frac{\pi}{a_1}\right)^2}. \quad (3.20)$$

Here, $Z_1^{\text{TE}_{10}}$, ε_{r1} and a_1 are the characteristic impedance, the relative dielectric constant and the width of port 1, respectively, while $Z_2^{\text{TE}_{10}}$, ε_{r2} and a_2 are the corresponding

characteristics of port 2; ω is the angular frequency and c_0 is the velocity of light in vacuum.

We aim to test our technique with the S -parameter sensitivity with respect to W and L at the optimal solution. We expect maximum power transfer at the optimal solution for W , L and f , where S_{11} of the transformer is minimum. Then we vary W and L around their optimal values at f to get the sensitivity of the S -parameters.

To derive the optimal solution of the transformer, we approximate the midsection as a transmission line with a characteristic impedance Z_c and length L . It is connected directly to the input and output waveguides with characteristic impedances Z_{in} and Z_{out} , respectively. According to the theoretical calculation, to obtain maximum power transfer,

$$Z_c = \sqrt{Z_{in}Z_{out}}, \quad L = \lambda_g / 4. \quad (3.21)$$

We calculate the discrete optimal solution as $[W \quad L \quad f]^T = [14\Delta h \quad 13\Delta h \quad 6.36 \text{ GHz}]^T$.

However, the physical model of the transformer is more complicated than the direct connection of transmission lines. The connection to the midsection should be modeled as a 2-port network as well. We use the optimal solution of HFSS as a reference. We sweep the parameters $[W \quad L \quad f]^T$ for the smallest S_{11} . The discrete optimal solution is found to be $[W \quad L \quad f]^T = [14\Delta h \quad 10\Delta h \quad 6.48 \text{ GHz}]^T$.

We first compute the sensitivity at the optimal W and L with a frequency sweep around the optimal f . The derivatives of $|S_{11}|$ and $|S_{21}|$ with respect to the section length L

are shown in Figure 3.20 and Figure 3.21. The results are compared with the HFSS finite-difference sensitivities.

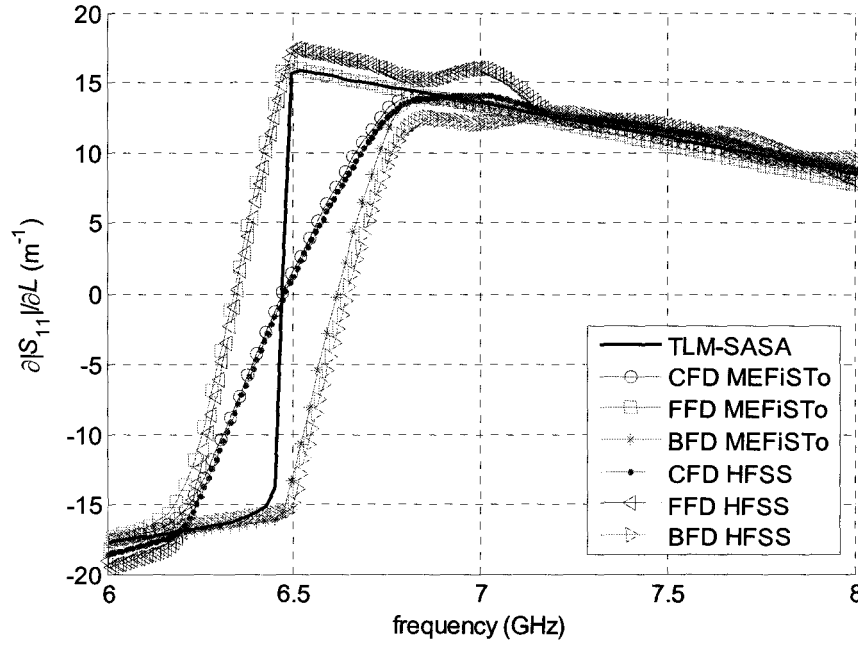


Figure 3.20. Derivatives of $|S_{11}|$ with respect to L in the waveguide impedance transformer example.

In Figure 3.20, the FFD and BFD curves clearly show the inferior accuracy of the first-order finite-difference approximations. For a given cell size, our results are less likely to suffer from an insufficiently refined grid. This is due to their second-order accuracy comparable to that of the CFD approximation.

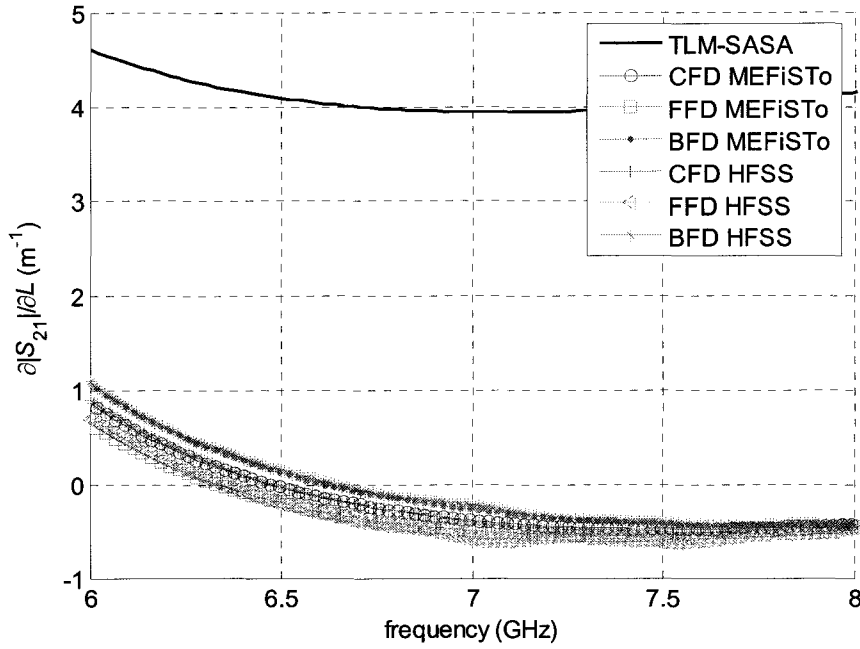


Figure 3.21. Derivatives of $|S_{21}|$ with respect to L in the waveguide impedance transformer example.

Then, we perform convergence analysis to illustrate the superior accuracy of the sensitivities computed with our approach as compared to those obtained by response-level finite differences. The derivatives of $|S_{11}|$ and $|S_{21}|$ with respect to the section length L and W with convergent mesh sizes are shown in Figure 3.22, Figure 3.23, Figure 3.24 and Figure 3.25, respectively.

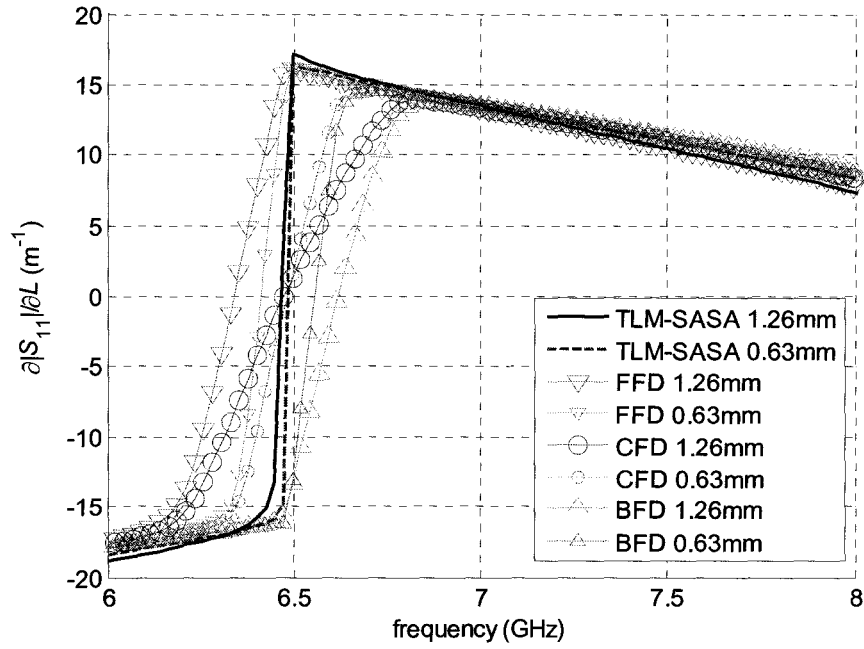


Figure 3.22. Convergence analysis of the derivatives of $|S_{11}|$ with respect to L in the waveguide impedance transformer example.

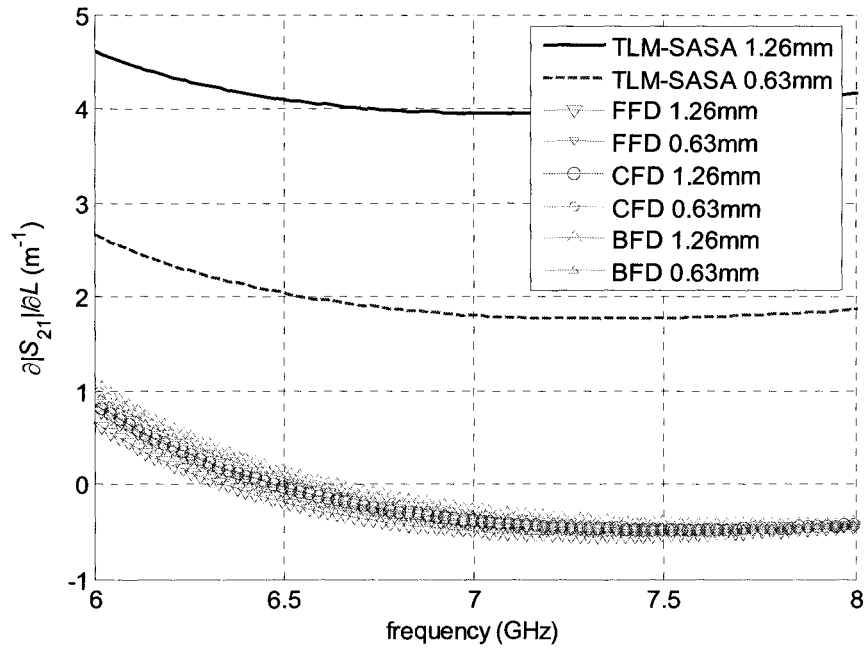


Figure 3.23. Convergence analysis of the derivatives of $|S_{21}|$ with respect to L in the waveguide impedance transformer example.

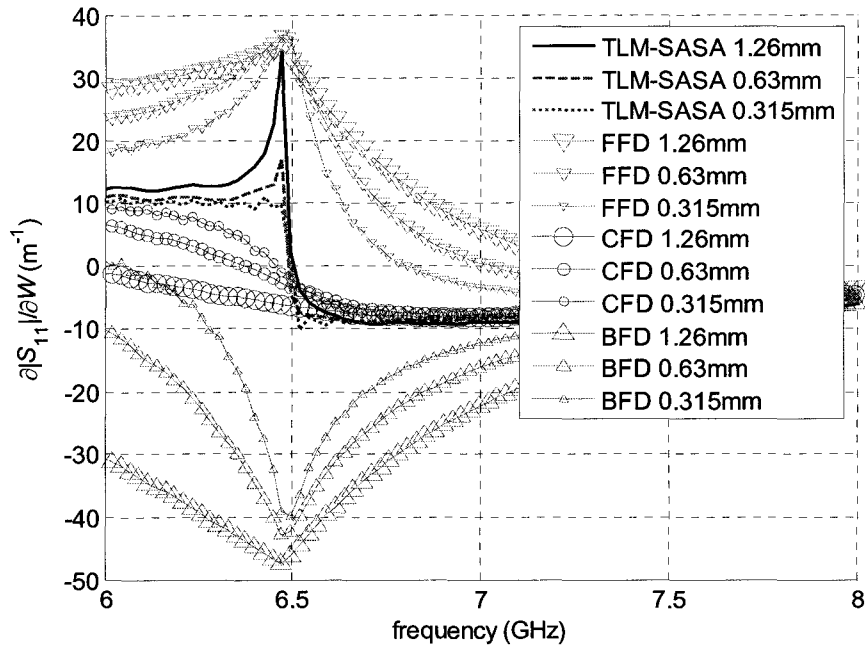


Figure 3.24. Convergence analysis of the derivatives of $|S_{11}|$ with respect to W in the waveguide impedance transformer example.

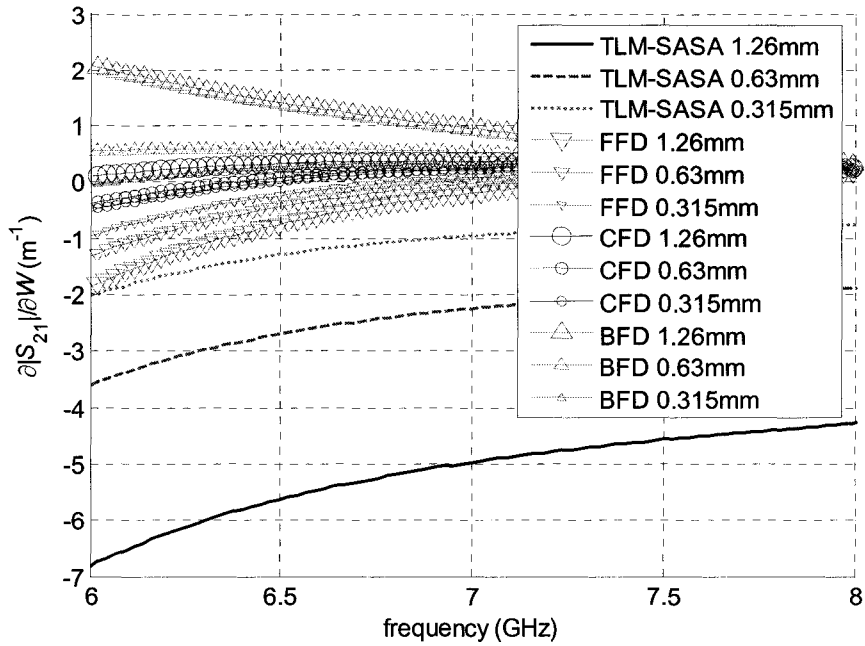


Figure 3.25. Convergence analysis of the derivatives of $|S_{21}|$ with respect to W in the waveguide impedance transformer example.

As the mesh is refined twice and then four-fold, the TLM-SASA curve changes little and consistently shows zero derivatives at our estimated optimal frequency $f = 6.48$ GHz. The CFD curves converge toward the TLM-SASA curves as the mesh is refined. When the cell size becomes too small, all finite-difference curves start to exhibit fluctuations, which is an indication that further reduction of the cell size will make the finite-difference estimates unreliable.

Finally, we perform a parameter sweep and compare the derivatives of the TLM-SASA technique and the MEFiSTo/HFSS finite-difference approximation. We vary L around its optimal value at the optimal W and f . The sensitivities of $|S_{11}|$ and $|S_{21}|$ are shown in Figure 3.26 and Figure 3.27, respectively. We then sweep W . The sensitivities of $|S_{11}|$ and $|S_{21}|$ are shown in Figure 3.28 and Figure 3.29, respectively.

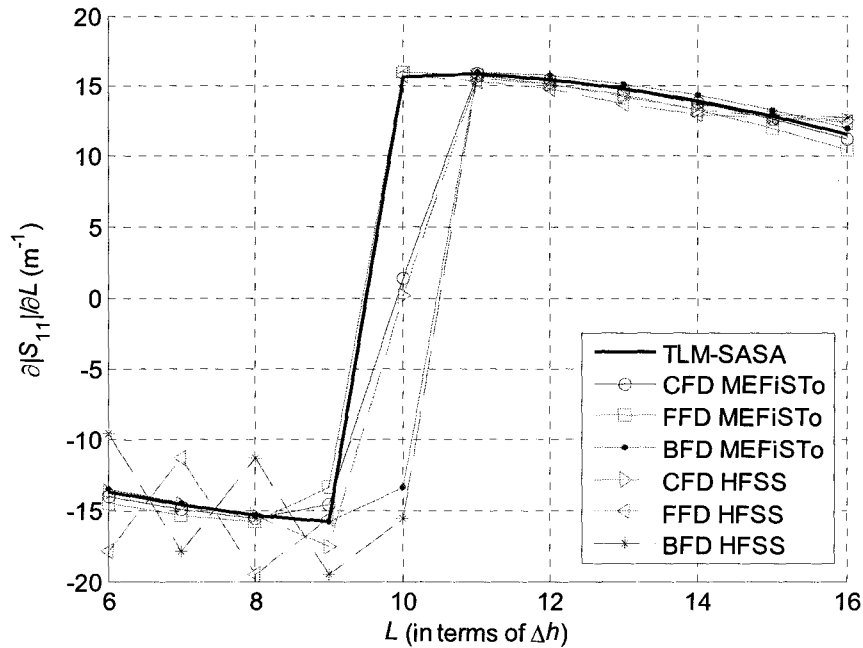


Figure 3.26. Derivatives of $|S_{11}|$ with respect to L in the waveguide impedance transformer example (parameter sweep of L).

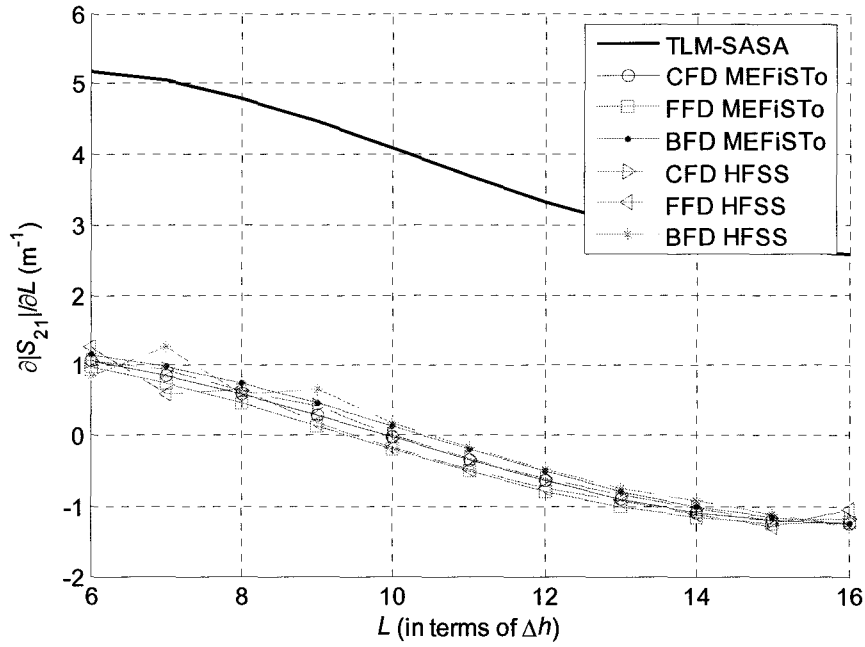


Figure 3.27. Derivatives of $|S_{21}|$ with respect to L in the waveguide impedance transformer example (parameter sweep of L).

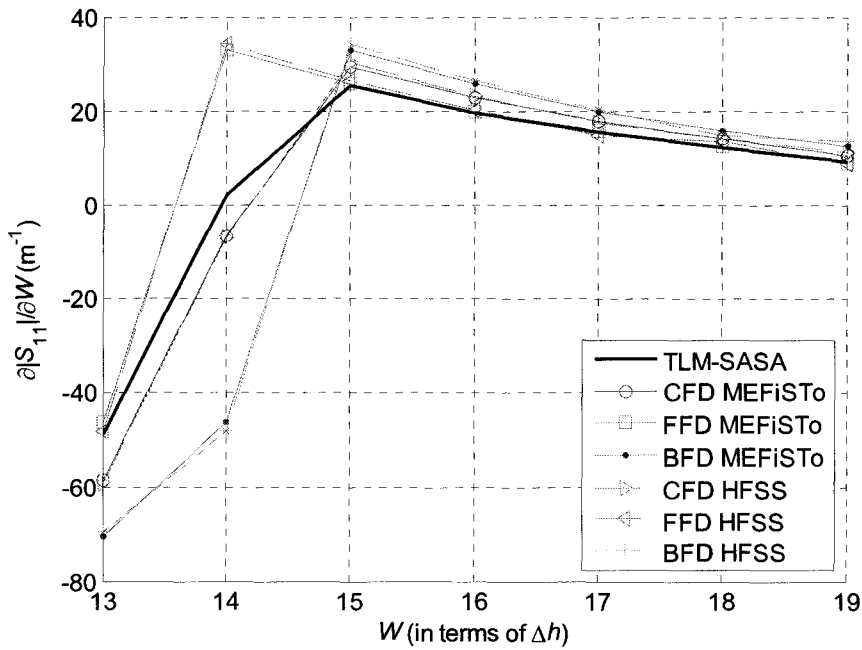


Figure 3.28. Derivatives of $|S_{11}|$ with respect to W in the waveguide impedance transformer example (parameter sweep of W).

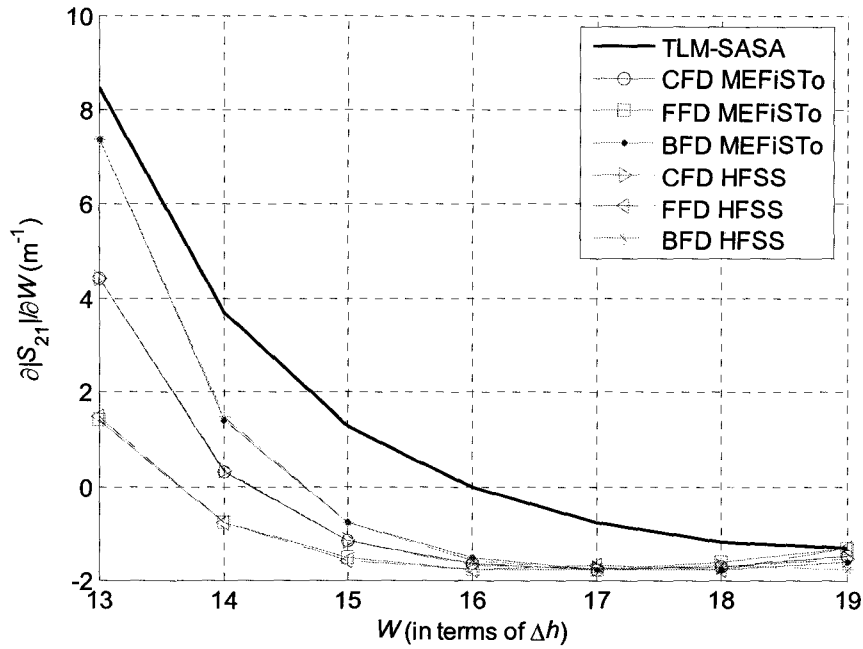


Figure 3.29. Derivatives of $|S_{21}|$ with respect to W in the waveguide impedance transformer example (parameter sweep of W).

In the lossless case, for a 2-port structure, we have $|S_{11}|^2 + |S_{21}|^2 = 1$, so we define an error function to estimate the accuracy of the S -parameter sensitivities of different techniques:

$$Err = |S_{11}| \frac{\partial |S_{11}|}{\partial p_n} + |S_{21}| \frac{\partial |S_{21}|}{\partial p_n}. \quad (3.22)$$

Here, p_n is the design parameter. We can compute the error from the sensitivity results we obtained above. We show the error of the S -parameter derivatives with respect to W in the waveguide impedance transformer example with a convergence analysis in Figure 3.30.

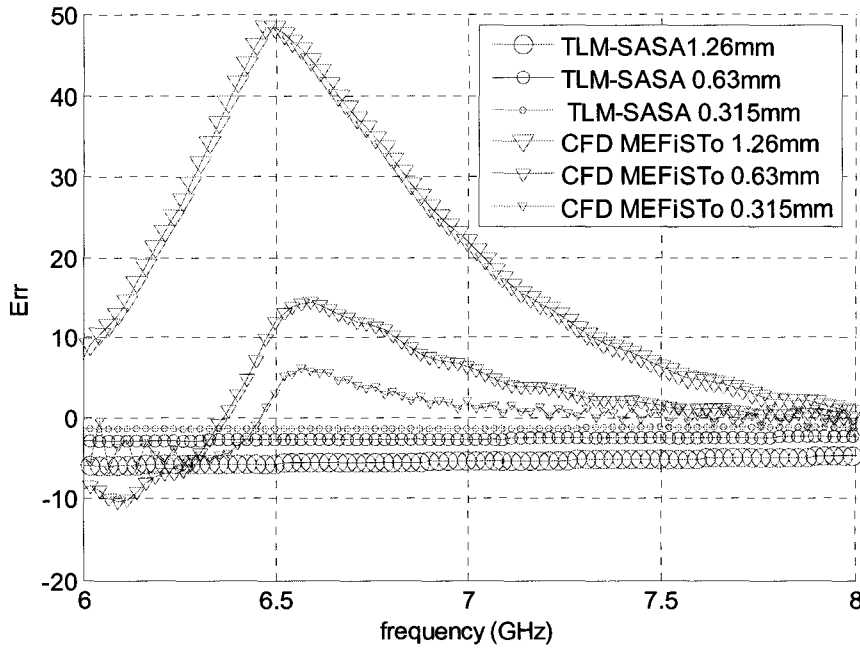


Figure 3.30. Convergence analysis of the error in S -parameter derivatives with respect to W in the waveguide impedance transformer example.

3.7 Summary

We developed an efficient method for S -parameter sensitivity analysis with commercial time-domain EM solvers based on a TLM self-adjoint sensitivity expression. The method converts the field quantities into reflected TLM voltages to make the expression applicable to commercial solvers providing field solution only. With commercial solvers, our current application is limited to loss-free homogenous structures.

Our approach is illustrated through the computation of the S -parameter sensitivities in the desired frequency band with respect to the shape parameters of waveguide discontinuities. Our results exhibit superior accuracy and efficiency than those

of the finite differences. The S -matrix and its derivatives with respect to all design parameters are obtained through a single system analysis. The overhead of the sensitivity computation is negligible compared to the computational intensity of the time-domain full-wave simulation. The memory requirements of the sensitivity analysis are mostly due to the field waveforms recorded at the perturbation points. The number of these probes can be reduced by one-third when we use conversion from field quantities instead of the incident voltages directly.

3.8 References

- [1] HFSS[®] v. 9.0, Ansoft, <http://www.ansoft.com/products/hf/hfss/> .
- [2] M.H. Bakr, N.K. Nikolova, “An adjoint variable method for time-domain transmission-line modeling with fixed structured grids,” *IEEE Trans. Microwave Theory Tech.*, vol. 52, no. 2, pp. 554–559, Feb. 2004.
- [3] M.H. Bakr, N.K. Nikolova, “Efficient estimation of adjoint-variable S -parameter sensitivities with time-domain TLM,” *International Journal of Numerical Modeling: Electronic Networks, Devices and Fields*, vol. 18, no.2, pp. 171-187, March/April 2005.
- [4] M.H. Bakr, N.K. Nikolova, and P.A.W. Basl, “Self-adjoint S -parameter sensitivities for lossless homogeneous TLM Problems,” *Int. J. of Numerical Modeling: Electronic Networks, Devices and Fields*, vol.18, pp. 441-455, Nov. 2005.

- [5] MEFiSTo-3D[®] Pro v. 4, *User Guide and Operating Manual*, 6th ed., Faustus Scientific, Jan. 2003, <http://www.faustcorp.com/products/mefisto3dpro/> .
- [6] Z. Chen, M.M. Ney, W.J.R. Hoefer, “A new finite-difference time-domain formulation and its equivalence with TLM symmetrical condensed node,” *IEEE Trans. Microwave Theory Tech.*, vol. 39, no. 12, pp. 2160–2169, Dec. 1991.
- [7] N.K. Nikolova, H.W. Tam, and M.H. Bakr, “Sensitivity analysis with the FDTD method on structured grids,” *IEEE Trans. Microwave Theory Tech.*, vol. 52, pp. 1207-1216, April 2004.

Chapter 4

FDTD-BASED SELF-ADJOINT SENSITIVITY ANALYSIS

4.1 Introduction

We present a self-adjoint approach to S -parameter sensitivity computation with time-domain electromagnetic (EM) simulators based on the finite-difference time-domain method (FDTD) discretization scheme. The method is applicable with any EM simulator, which can export the E -field at user defined points. The S -parameter derivatives are computed as an independent post-process whose computational requirements are negligible compared to the full-wave system analysis. Adjoint simulations are not needed even if the problem is lossy and inhomogeneous.

This algorithm is applicable to all time-domain commercial solvers, where the field solution is available, while the TLM-based adjoint variable method (AVM) approach needs to convert the field solution to incident voltages. Meanwhile, the FDTD-AVM algorithm is valid for lossy inhomogeneous structures, while the self-adjoint TLM-based AVM approach is limited to the loss-free homogeneous case. To apply it in the

framework of a TLM-based commercial solver (e.g. MEFiSTo-3D pro [1]), we propose a method to convert the field solution at the TLM mesh nodes into a field solution at the Yee-cell FDTD nodes, because the two discretization grids are displaced in space by half a cell along each axis.

We start by giving a concise summary of the E -field vector wave equation and the general FDTD-AVM approach. The self-adjoint FDTD-based AVM algorithm for evaluating the S -parameter sensitivities is illustrated after that. Then the method to convert field solutions from the TLM mesh to FDTD-mesh field solutions is given. The de-embedding technique for the AVM is explained in detail. The validation of the algorithm is carried out through waveguide and antenna examples. Our self-adjoint S -parameter sensitivities are computed with respect to shape design parameters over a desired frequency band or over a parameter sweep at a certain frequency point. The AVM results are compared with finite-difference approximations. Good agreement is obtained between the two sets of data. The results are additionally verified with HFSS [2]. We discuss the CPU time and storage requirements and delineate the advantages and the limitations of the technique. We conclude with a summary.

4.2 Adjoint Variable Method for the FDTD Method

An EM problem in a linear medium can be described by the vector wave equation for the E -field

$$\nabla \times \boldsymbol{\mu}^{-1} \nabla \times \mathbf{E} + \varepsilon \frac{\partial^2 \mathbf{E}}{\partial t^2} + \boldsymbol{\sigma} \frac{\partial \mathbf{E}}{\partial t} = -\frac{\partial \mathbf{J}}{\partial t} \quad (4.1)$$

where ε , μ and σ are the medium permittivity, permeability and conductivity, respectively. For a unique solution, zero boundary conditions and initial conditions are specified.

Applying central finite differences to (4.1), we obtain

$$\mathcal{C}^2 \mathbf{E} - \alpha \cdot D_{tt} \mathbf{E} - s \cdot D_{t2} \mathbf{E} = \mathbf{G} \quad (4.2)$$

where

$$\mathbf{G} = \beta \cdot D_t \mathbf{J} \quad (4.3)$$

is the excitation term, and

$$\alpha = \varepsilon_r \left(\frac{\Delta h}{c \Delta t} \right)^2, \quad \beta = \mu_0 \frac{\Delta h^2}{\Delta t}, \quad s = \frac{\sigma \mu_0 \Delta h^2}{2 \Delta t} \quad (4.4)$$

are numerical constants. Here, c is the speed of light in vacuum, μ_0 is the permeability of vacuum, ε_r is the relative permittivity, Δt is the discretization step in time, and Δh is the smallest cell size, $\Delta h = \min(\Delta x, \Delta y, \Delta z)$. The difference operators in time are as follows:

$$D_t \mathbf{J}(t_0) = \mathbf{J}(t_0 + \Delta t / 2) - \mathbf{J}(t_0 - \Delta t / 2) \quad (4.5)$$

$$D_{t2} \mathbf{E}(t_0) = \mathbf{E}(t_0 + \Delta t) - \mathbf{E}(t_0 - \Delta t) \quad (4.6)$$

$$D_{tt} \mathbf{E}(t_0) = \mathbf{E}(t_0 + \Delta t) + \mathbf{E}(t_0 - \Delta t) - 2 \cdot \mathbf{E}(t_0). \quad (4.7)$$

The difference between the first-order operators (4.5) and (4.6) is due to the specifics of the FDTD scheme where the E -field and the current density are sampled at points, which are mutually displaced by one-half time step. The finite-difference double curl operator

\mathcal{C}^2 produces three vector components; e.g., in rectangular coordinates, its x -component in a magnetically homogeneous medium is

$$(\mathcal{C}^2 \mathbf{E})_x = h_y^2 D_{yy} E_x + h_z^2 D_{zz} E_x - h_y h_x D_{yx} E_y - h_z h_x D_{zx} E_z \quad (4.8)$$

where

$$h_x = \Delta h / \Delta x, \quad h_y = \Delta h / \Delta y, \quad h_z = \Delta h / \Delta z. \quad (4.9)$$

The second-order operators in space use central differences, e.g.,

$$D_{yy} E_x(x_0, y_0, z_0) = E_x(x_0, y_0 + \Delta y, z_0) + E_x(x_0, y_0 - \Delta y, z_0) - 2 \cdot E_x(x_0, y_0, z_0) \quad (4.10)$$

$$\begin{aligned} D_{yx} E_y(x_0, y_0, z_0) = & \left[E_y(x_0 + \Delta x / 2, y_0 + \Delta y / 2, z_0) - E_y(x_0 - \Delta x / 2, y_0 + \Delta y / 2, z_0) \right] \\ & - \left[E_y(x_0 + \Delta x / 2, y_0 - \Delta y / 2, z_0) - E_y(x_0 - \Delta x / 2, y_0 - \Delta y / 2, z_0) \right]. \end{aligned} \quad (4.11)$$

The y and z components of $\mathcal{C}^2 \mathbf{E}$ can be obtained from $(\mathcal{C}^2 \mathbf{E})_x$ in (4.8) using the cyclic substitution $x \rightarrow y \rightarrow z \rightarrow x$.

The EM response in the time-domain sensitivity analysis is a functional of the field solution [3]:

$$F(\mathbf{E}, \mathbf{p}) = \int_0^{T_{\max}} \iiint_{\Omega} f(\mathbf{E}, \mathbf{p}) d\Omega dt. \quad (4.12)$$

Here, Ω is the computational volume and T_{\max} is the simulation time. We refer to the integrand $f(\mathbf{E}, \mathbf{p})$ as the local response. It depends on \mathbf{p} implicitly through the field solution \mathbf{E} .

The response sensitivity is defined by the gradient row-vector

$$\nabla_{\mathbf{p}} F = \left[\frac{\partial F}{\partial p_1} \quad \dots \quad \frac{\partial F}{\partial p_N} \right] \quad (4.13)$$

where $\mathbf{p} = [p_1 \cdots p_N]^T$ is the vector of design parameters.

A discrete adjoint-sensitivity formula based on (4.1) was developed in [3]:

$$\frac{\partial F}{\partial p_n} \approx \frac{\partial^e F}{\partial p_n} - \int_0^{T_{\max}} \iiint_{\Omega} (\hat{\mathbf{E}})_n \cdot \frac{\Delta_n R(\bar{\mathbf{E}})}{\Delta p_n} d\Omega dt, \quad n=1, \dots, N, \quad (4.14)$$

$$\frac{\Delta_n R(\bar{\mathbf{E}})}{\Delta p_n} = \frac{\Delta_n \mathcal{C}^2}{\Delta p_n} \cdot \bar{\mathbf{E}} - \frac{\Delta_n \alpha}{\Delta p_n} \cdot D_{tt} \bar{\mathbf{E}} - \frac{\Delta_n s}{\Delta p_n} \cdot D_{t2} \bar{\mathbf{E}} - \frac{\Delta_n \mathbf{G}}{\Delta p_n}. \quad (4.15)$$

In (4.14), $\partial^e F / \partial p_n$ is the explicit derivative, $\bar{\mathbf{E}}$ is the solution of (4.2) in the nominal state, and $(\hat{\mathbf{E}})_n$ is the solution of the adjoint problem in the n th perturbed state. The nominal state is described by (4.2) when the designable parameters are at their nominal values. In the n th perturbed state, $p_n, n \in \{1, \dots, N\}$, is changed and all other parameters are kept at their nominal values.

The sensitivity expression (4.14) in a discrete form is

$$\frac{\partial \tilde{F}_p}{\partial p_n} \approx - \frac{\Delta t}{\Delta p_n} \sum_{n_t=1}^{N_{\max}} \sum_{P \in \mathcal{S}_n} \left[(\hat{\mathbf{E}}_{pq}^{(n_t)}) \cdot \Delta_n R(\bar{\mathbf{E}}_q^{(n_t)}) \cdot \Delta x \Delta y \Delta z \right]_P \quad (4.16)$$

where $t = n_t \Delta t$, $T_{\max} = N_{\max} \Delta t$, \mathcal{S}_n is the set of points where $\Delta_n R(\bar{\mathbf{E}}_q^{(n_t)})$ is non-zero for the n th perturbation. $\Delta_n R(\bar{\mathbf{E}}_q^{(n_t)})$ is given in (4.15). The derivative is not dependent on p_n explicitly if the port is not affected by the changes of p_n .

For cases where the system coefficients have analytical derivatives, the adjoint-sensitivity formula in (4.14)-(4.15) becomes [4]

$$\frac{\partial F}{\partial p_n} \approx \frac{\partial^e F}{\partial p_n} - \int_0^{T_{\max}} \iiint_{\Omega} \hat{\mathbf{E}} \cdot \frac{\partial_n R(\bar{\mathbf{E}})}{\partial p_n} d\Omega dt, \quad n=1, \dots, N, \quad (4.17)$$

$$\frac{\partial_n R(\bar{\mathbf{E}})}{\partial p_n} = \frac{\partial_n \mathcal{C}^2}{\partial p_n} \cdot \bar{\mathbf{E}} - \frac{\partial_n \alpha}{\partial p_n} \cdot D_{tt} \bar{\mathbf{E}} - \frac{\partial_n s}{\partial p_n} \cdot D_{t2} \bar{\mathbf{E}} - \frac{\partial_n \mathbf{G}}{\partial p_n}. \quad (4.18)$$

Here $\hat{\mathbf{E}}$ is the solution of the unperturbed adjoint problem.

If a design variable represents the constitutive parameters of an object, the equation coefficients are simple analytical functions of ε_r and σ . The implementation of the adjoint-variable method is relatively straightforward for the EM system (4.1). In regions where the constitutive parameters change,

$$\begin{aligned} \frac{\partial R(\bar{\mathbf{E}})}{\partial \varepsilon_r} &= -\frac{\partial \alpha}{\partial \varepsilon_r} \cdot D_{tt} \bar{\mathbf{E}} = -\left(\frac{\Delta h}{c \Delta t} \right)^2 \cdot D_{tt} \bar{\mathbf{E}} \\ \frac{\partial R(\bar{\mathbf{E}})}{\partial \sigma} &= -\frac{\partial s}{\partial \sigma} \cdot D_{t2} \bar{\mathbf{E}} = -\left(\frac{\mu_0 \Delta h^2}{2 \Delta t} \right) \cdot D_{t2} \bar{\mathbf{E}} \end{aligned} \quad (4.19)$$

as per (4.4). Outside of the perturbed regions, the derivatives of α and s in (4.14) are zero, and so are the expressions in (4.19).

The derivatives of the system coefficients of (4.2) with respect to shape parameters cannot be derived analytically. In this case, we resort to finding their differences (4.15) in the nominal (unperturbed) state and the n th perturbed state. The shape parameters belong to a discrete space and thus their change is always a multiple of the cell size. We assume the smallest change of one cell size, e.g., $\Delta p_n = \Delta h$ on a uniform grid. With the change of p_n , the coefficients of (4.2) experience a stepwise change at a few grid points surrounding the changing object. We refer to these points as perturbation grid points. Only at these points, the term in (4.15) has non-zero values.

To achieve computational advantage of the adjoint-variable approach, we perform only one adjoint simulation for the N perturbed states, where the adjoint solution around

the n th perturbation $(\hat{\mathbf{E}})_n$ is approximated by a simple shift in space of the unperturbed problem solution $\hat{\mathbf{E}}$ in the direction of the assumed perturbation [3].

The adjoint problem, whose solution $\hat{\mathbf{E}}$ we seek, is a quasi-EM problem governed by the vector wave equation

$$\nabla \times [\boldsymbol{\mu}^{-1}]^T \nabla \times \hat{\mathbf{E}} + \boldsymbol{\varepsilon}^T \frac{\partial^2 \hat{\mathbf{E}}}{\partial \tau^2} + \boldsymbol{\sigma}^T \frac{\partial \hat{\mathbf{E}}}{\partial \tau} = \frac{\partial \hat{\mathbf{J}}}{\partial \tau} \quad (4.20)$$

complemented by the same boundary conditions as in the original problem (4.1), and by zero terminal conditions. Here, τ is the inverse-time variable, $\tau = T_{\max} - t$. The adjoint current density is defined by [3]

$$\beta D_t \hat{\mathbf{J}}_{(x_0, y_0, z_0, t_0)} = \left(\hat{\mathbf{x}} \frac{\partial f}{\partial E_x} + \hat{\mathbf{y}} \frac{\partial f}{\partial E_y} + \hat{\mathbf{z}} \frac{\partial f}{\partial E_z} \right)_{(x_0, y_0, z_0, t_0)} \quad (4.21)$$

where β has already been defined in (4.4) and f is the local response of the integral in (4.12). In order to solve (4.20) in τ -time, the time sequence of $\hat{\mathbf{J}}$ obtained from (4.21) has to be applied backwards.

4.3 FDTD-based Self-adjoint Sensitivity Theory

Comparing the original and adjoint systems (4.1) and (4.20), if the adjoint and original excitation current density $\hat{\mathbf{J}}_p$ and \mathbf{J}_p at the p th port have identical distributions across the ports and in their respective times but with a minus sign, i.e.,

$$(-\hat{\mathbf{J}}_p)(x'_p, y'_p, \tau) = \mathbf{J}_p(x'_p, y'_p, t) \quad (4.22)$$

then the respective equivalence between the original and adjoint solutions is

$$\hat{\mathbf{E}}_p(x'_p, y'_p, \tau) = \mathbf{E}_p(x'_p, y'_p, t), \quad \tau = T_{\max} - t. \quad (4.23)$$

It follows that the adjoint solution $\hat{\mathbf{E}}_p(x'_p, y'_p, \tau)$ obtained from (4.20) by exciting the p th port can be deduced from the values of the original solution $\mathbf{E}_p(x'_p, y'_p, t)$ obtained from the forward-running simulation (4.1) when the p th port is excited. Thus, the adjoint simulations can be eliminated. The details are explained below.

The S_{pq} is defined in Chapter 2 (2.1). The derivative of S_{pq} with respect to the parameter p_n is

$$\frac{\partial S_{pq}}{\partial p_n} = \sqrt{\frac{Z_q}{Z_p}} \cdot \frac{1}{\tilde{F}_q} \cdot \frac{\partial \tilde{F}_p}{\partial p_n}. \quad (4.24)$$

Typically, the port waveguides are not subjected to design changes. This makes Z_p , Z_q and \tilde{F}_q independent of p_n . Thus, the S_{pq} derivative is determined by the derivative of the response $F = \tilde{F}_p$, $\partial F_p / \partial p_n$ (4.16).

The adjoint current density is given by (4.21), for which we need to identify $f(\mathbf{E}, \mathbf{p})$. The comparison of (2.2) and (4.12) shows that the local response function for \tilde{F}_p is

$$f(x'_p, y'_p, t) = \frac{\mathbf{E}_{q\perp}^{ou}(x'_p, y'_p, t) \cdot \mathbf{e}_{p\perp}(x'_p, y'_p)}{\Delta z_p} \cdot e^{-j\omega_0 t} \quad (4.25)$$

at the p th port, and is zero elsewhere. Here, Δz_p is the longitudinal cell size at the p th port. It takes care of the dimensionality of the integrand in the surface integration (2.2) as compared to that of the volume integral in (4.12). Also, it is clear that in the case of the S -parameters, f has no explicit dependence on p_n , i.e., $\partial^e S_{pq} / \partial p_n = 0$, $n = 1, \dots, N$.

According to (4.21), the derivative of the response (4.25) with respect to the field at the p th port gives the adjoint current density, which excites the adjoint problem at the p th port:

$$\beta \cdot D_t \hat{\mathbf{J}}_{pq}(x'_p, y'_p, t) = \mathbf{e}_{p\perp}(x'_p, y'_p) \cdot e^{-j\omega_0 t} / \Delta z_p. \quad (4.26)$$

The difference time operator can be replaced with its analytical counterpart: $\beta \cdot D_t \leftrightarrow \beta \Delta t \cdot \partial / \partial t$. When the integration in time is performed, the result for the real and the imaginary parts of $\hat{\mathbf{J}}_{pq}$ can be written as

$$(-\hat{\mathbf{J}}_{pq})_R(x'_p, y'_p, t) = \mathbf{e}_{p\perp}(x'_p, y'_p) \cdot \hat{g}_R^{\omega_0}(t) \quad (4.27)$$

$$(-\hat{\mathbf{J}}_{pq})_I(x'_p, y'_p, t) = \mathbf{e}_{p\perp}(x'_p, y'_p) \cdot \hat{g}_I^{\omega_0}(t) \quad (4.28)$$

where

$$\hat{g}_R^{\omega_0}(t) = \frac{\sin(\omega_0 t)}{\omega_0 \beta \Delta t \Delta z_p}, \quad \hat{g}_I^{\omega_0}(t) = \frac{\cos(\omega_0 t)}{\omega_0 \beta \Delta t \Delta z_p}. \quad (4.29)$$

The adjoint excitation is taken with a minus in order to obtain the adjoint field with the correct sign. The real part of the adjoint solution $(\hat{\mathbf{E}}_{pq})_R$, due to $(-\hat{\mathbf{J}}_{pq})_R$, is used in the computation of the derivative of $\text{Re}S_{pq}$, and the imaginary part $(\hat{\mathbf{E}}_{pq})_I$, due to $(-\hat{\mathbf{J}}_{pq})_I$, is used for the derivative of $\text{Im}S_{pq}$. $(\hat{\mathbf{E}}_{pq})_R$ and $(\hat{\mathbf{E}}_{pq})_I$ are needed only at the perturbation grid points [3].

As illustrated in (4.22)-(4.23), when the adjoint problem is excited by $-\hat{\mathbf{J}}_{pq}$ and runs backwards in time, it is equivalent to the original problem as far as the adjoint electric field $\hat{\mathbf{E}}_{pq}$ is concerned. The field solutions of the two problems are identical (in

their respective times) if their excitations, $-\hat{\mathbf{J}}_{pq}(x'_p, y'_p, \tau)$ and $\mathbf{J}_p(x'_p, y'_p, t)$, have identical distributions across the port and in time. From (4.27)-(4.28), it is clear that the adjoint current distribution across the port is the same as the original port distribution since the latter is set as

$$\mathbf{J}_p(x'_p, y'_p, t) = J_p \cdot \mathbf{e}_{p\perp}(x'_p, y'_p) \cdot g(t) \quad (4.30)$$

for S -parameter analysis. Here, J_p is a scaling factor, e.g., $J_p = \sqrt{a_p b_p / 2}$ for the dominant TE_{z10} mode if the magnitude of \mathbf{J}_p is set to 1. $\mathbf{e}_{p\perp}$ is the transverse modal vector defined in (2.4). $g(t)$ is the excitation waveform.

Also, (4.27)-(4.28) show that the adjoint excitations and fields are harmonic. It is then possible, in a linear medium, to obtain an adjoint field solution from an original field by properly manipulating its spectral component at ω_0 . We emphasize that for the sensitivity of the S_{pq} parameter, the original excitation is at port q , while the adjoint one is at port p , see (4.25)-(4.26). However, in full scattering matrix characterization, the field solution with the port p excitation is available as well. Thus, we seek the proper relation between $(\hat{\mathbf{E}}_{pq})_R$ and $(\hat{\mathbf{E}}_{pq})_I$ on one hand and the ω_0 spectral component of the original (p -port) field solution \mathbf{E}_p on the other.

The time waveform of the original excitation is $g(t)$. To make the adjoint simulation in τ -time identical to the original one in forward t -time, we excite the former by the reversed pulse $\hat{g}(t) = g(T_{\max} - t)$. This is equivalent to $\hat{g}(\tau) = g(t)$. The ω_0 spectral component of the forward pulse $g(t)$,

$$\underline{G} = \int_0^{T_{\max}} g(t) \cdot e^{-j\omega_0 t} dt = G_m \cdot e^{j\varphi_g} \quad (4.31)$$

is related to that of the reversed pulse $g(T_{\max} - t) = \hat{g}(t)$ as

$$\hat{\underline{G}} = \int_0^{T_{\max}} g(T_{\max} - t) \cdot e^{-j\omega_0 t} dt = \underline{G}^* \cdot e^{-j\omega_0 T_{\max}} = G_m \cdot e^{-j(\omega_0 T_{\max} + \varphi_g)}. \quad (4.32)$$

Here, \underline{G}^* is the conjugate of \underline{G} , and G_m is the magnitude of \underline{G} as per (4.31). Thus, the ω_0 spectral component of $\hat{g}(t)$ is

$$\hat{g}^{\omega_0}(t) = G_m \cos(\omega_0 t - \varphi_g - \omega_0 T_{\max}). \quad (4.33)$$

Due to the equivalence between the original and the backward-running adjoint problem, the so obtained adjoint field is related to the original one as $\hat{\mathbf{E}}_{pq}(P, T_{\max} - t) = \mathbf{E}_p(P, t)$ at a point P , and its ω_0 spectral component is

$$\hat{E}_{\zeta pq}^{\omega_0}(P, t) = |E_{\zeta p(P)}^{\omega_0}| \cos(\omega_0 t - \varphi_{e\zeta p(P)} - \omega_0 T_{\max}), \quad \zeta = x, y, z. \quad (4.34)$$

Here, ζ denotes the vector component; $|E_{\zeta p(P)}^{\omega_0}|$ and $\varphi_{e\zeta p(P)}$ are the magnitude and the phase of the ω_0 spectral component of the original $E_{\zeta p}$ waveform at P .

We now compare the desired adjoint excitation waveforms in (4.29) with the ω_0 component of the adjoint pulse (4.33). Their magnitudes and phase angles relate as

$$|\hat{g}_R^{\omega_0}| = |\hat{g}_I^{\omega_0}| = \frac{|\hat{g}^{\omega_0}|}{G_m \omega_0 \beta \Delta t \Delta z_p}, \quad (4.35)$$

$$\text{Angle}\{\hat{g}_R^{\omega_0}\} = \text{Angle}\{\hat{g}^{\omega_0}\} + \varphi_g + \omega_0 T_{\max} - \pi/2, \quad (4.36)$$

$$\text{Angle}\{\hat{g}_I^{\omega_0}\} = \text{Angle}\{\hat{g}^{\omega_0}\} + \varphi_g + \omega_0 T_{\max}. \quad (4.37)$$

The desired adjoint fields $(\hat{\mathbf{E}}_{pq})_R$ and $(\hat{\mathbf{E}}_{pq})_I$ can be obtained from the ω_0 component of the adjoint field (4.34) by: 1) scaling the magnitude by the factor in (4.35), and 2) adding the difference in the angles in (4.36) and (4.37) to their respective phases. The result is

$$(\hat{E}_{\zeta pq}^{\omega_0})_R(P, t) = \frac{|E_{\zeta p(P)}^{\omega_0}|}{J_p G_m \omega_0 \beta \Delta t \Delta z_p} \cos\left(\omega_0 t - \varphi_{e\zeta p(P)} + \varphi_g - \frac{\pi}{2}\right) \quad (4.38)$$

$$(\hat{E}_{\zeta pq}^{\omega_0})_I(P, t) = \frac{|E_{\zeta p(P)}^{\omega_0}|}{J_p G_m \omega_0 \beta \Delta t \Delta z_p} \cos\left(\omega_0 t - \varphi_{e\zeta p(P)} + \varphi_g\right). \quad (4.39)$$

Here, the scaling factor J_p is added in the denominator to account for the actual strength of the source, see (4.30). In (4.38)-(4.39), G_m and φ_g are obtained through the Fourier transform (FT) of the original excitation pulse $g(t)$ as per (4.31), while $|E_{\zeta p(P)}^{\omega_0}|$ and $\varphi_{e\zeta p(P)}$ are obtained through the FT of the \mathbf{E} -field recorded at a perturbation grid point P during the original simulation, in which port p is excited.

In conclusion, we do not need to perform any adjoint simulations in order to compute the derivatives of the whole scattering matrix with respect to all design parameters. The necessary information is already contained in the EM field solution of the original problem. Our algorithm, which exploits the self-adjoint nature of the linear problem, uses this information in the most efficient manner.

4.4 Conversion from TLM mesh to FDTD Mesh

Our finite-difference sensitivity technique assumes that the E -field components are computed at the edges of the staggered FDTD-Yee grid. In the TLM method,

however, all field components are co-located and computed at the center of the node. As a result, the vertical electric field component computed by the 2D TLM is displaced by half a cell size with respect to the location where our technique needs it. This is illustrated in Figure 4.1. The solid lines depict the 2D TLM grid, and the dash lines show the 2D FDTD grid. The solid circles are the points where the TLM solver computes the vertical E -field; the squares are the points where the FDTD AVM algorithm needs the vertical E -field. We obtain the desired E -field at an FDTD node by taking the average of the E -field waveforms recorded at the four TLM neighboring points. When the TLM mesh is fine enough, the average gives the FDTD result accurately.

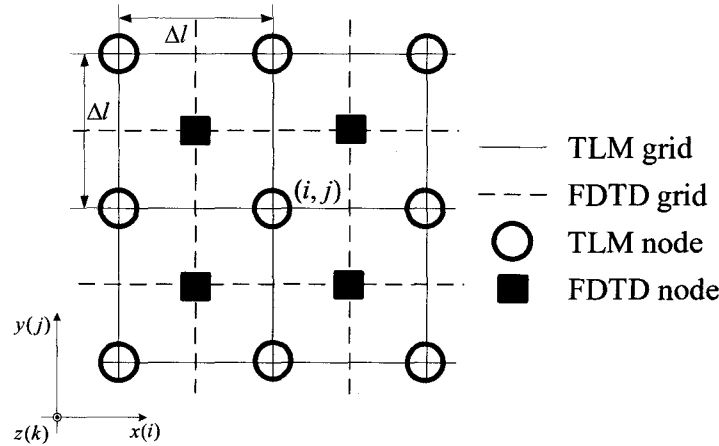


Figure 4.1. H -plane view of the 2D TLM and FDTD mesh.

4.5 De-embedding Technique for AVM

According to the self-adjoint theory, the adjoint source and the respective observation points should be located at the same place. However, to extract S -parameters

accurately, we usually choose the observation plane to be away from the boundary, the excitation and the discontinuities, as in Figure 2.1. To take into account this displacement in computing $\partial \tilde{F}_{pq}^{obs} / \partial p_n$, the adjoint field $\hat{\underline{\mathbf{E}}}_{pq}^{\omega_0}$ at a perturbation point P must be augmented by

$$\hat{\underline{\mathbf{E}}}_{pq}^{\omega_0}(P)_{aug} = \hat{\underline{\mathbf{E}}}_{pq}^{\omega_0}(P)_{recorded} \cdot e^{\gamma_p D_p}. \quad (4.40)$$

That is equivalent to moving the adjoint source from the observation plane to the excitation plane of port p . Here, we assume that the observation plane is further into the port waveguide compared to the excitation plane. This can be realized also by keeping the adjoint field $\hat{\underline{\mathbf{E}}}_{pq}^{\omega_0}$ unchanged and modifying the source spectrum \underline{G}^{ω_0} by

$$\underline{G}_{aug}^{\omega_0} = \underline{G}_{recorded}^{\omega_0} \cdot e^{-\gamma_p D_p}. \quad (4.41)$$

Then the adjoint solution in (4.38) and (4.39) with de-embedding becomes

$$(\hat{E}_{\zeta pq}^{\omega_0})_R(P, t) = \frac{|E_{\zeta p(P)}^{\omega_0}| e^{\alpha_p D_p}}{J_p G_m \omega_0 \beta \Delta t \Delta z_p} \cos\left(\omega_0 t - \varphi_{e\zeta p(P)} + \varphi_g - \frac{\pi}{2} - \beta_p D_p\right), \quad (4.42)$$

$$(\hat{E}_{\zeta pq}^{\omega_0})_I(P, t) = \frac{|E_{\zeta p(P)}^{\omega_0}| e^{\alpha_p D_p}}{J_p G_m \omega_0 \beta \Delta t \Delta z_p} \cos(\omega_0 t - \varphi_{e\zeta p(P)} + \varphi_g - \beta_p D_p). \quad (4.43)$$

4.6 Validation Examples

The examples focus on the sensitivity calculations with respect to the shape parameters in 2D waveguide (in the dominant TE_{10} mode) and antenna problems. We set “GSCN (Generalized Symmetrical Condensed Node) mesh for H -plane” in MEFiSTo-3D Pro for the simulation. After we set the cell size Δh and define the mesh, the discrete

time step Δt is determined automatically by the software, so that $q = \Delta h / c \Delta t = 2$. The sources are located next to the port boundaries.

The first two examples have been analyzed with the self-adjoint TLM-based AVM algorithm with the incident-voltage solution of our in-house solver [5] as well as with the field solution of MEFiSTo [6]-[7]. Here, we use the self-adjoint FDTD-AVM algorithm with the averaged field solution.

The TLM solver does not support the current-density excitation in (4.1); however, the E -field source can be used with a vertical component excitation. With this source, the sensitivity results have to be multiplied by a constant factor (independent of the grid parameters) to account for the difference in the powers injected by the current and the E -field sources. This factor is determined empirically by comparing the AVM and the CFD derivatives with respect to one of the parameters. In 2D loss-free problems, the factor is 150; in 3D loss-free problems, the factor is 150^2 .

In all plots, the derivative curves obtained with our time-domain self-adjoint sensitivity analysis approach are marked with FDTD-SASA, while the curves obtained through parameter perturbations and finite differencing of the S -parameters are marked with BFD, CFD and FFD for the backward, central, and forward finite differences, respectively. Response finite differences are used with both commercial solvers, MEFiSTo-3D Pro and HFSS, in order to acquire reference sensitivity curves and compare them with the FDTD-SASA results.

4.6.1 Single-resonator Filter

The structure of the single-resonator filter is shown in Figure 2.12. The setup of the MEFiSTo simulation is shown in Table 2.2. The probe fields needed in the FDTD-based SASA algorithm are illustrated in Figure 4.2 and Figure 4.3, where we assume an increase of the length of the resonator D and its septum width W , respectively

The sensitivities of $|S_{11}|$ and $|S_{21}|$ with respect to D are presented in Figure 4.4 and Figure 4.5, respectively. The sensitivities of $|S_{11}|$ and $|S_{21}|$ with respect to W are presented in Figure 4.6 and Figure 4.7, respectively

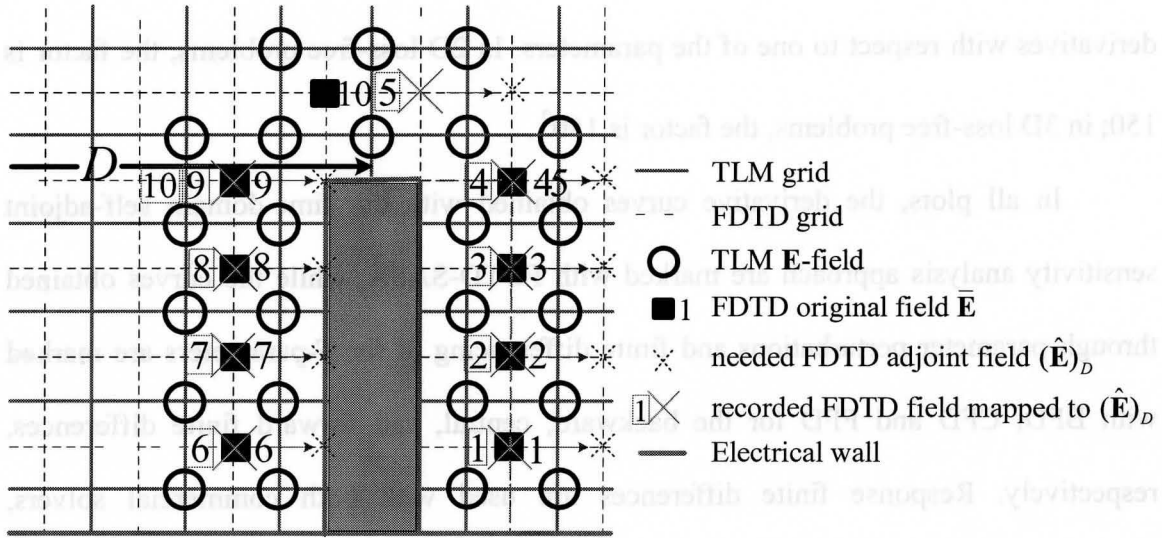


Figure 4.2. FDTD-based AVM probes (marked with circles) at the right septum (assume increasing D) in the single-resonator filter example.

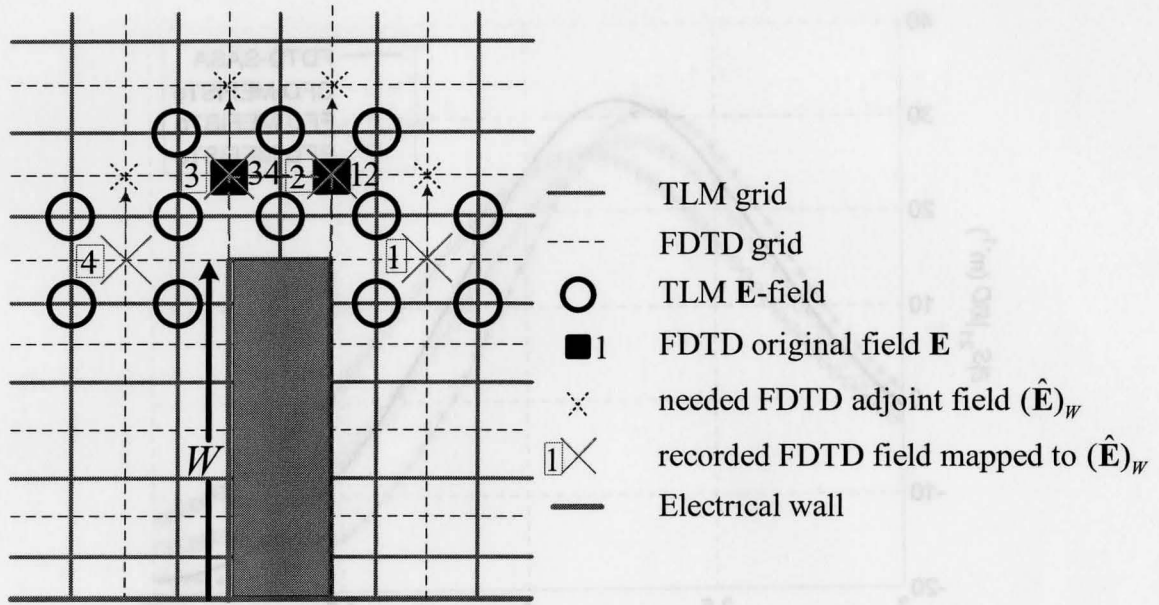


Figure 4.3 FDTD-based AVM probes (marked with circles) at the right septum (assume increasing W) in the single-resonator filter example.

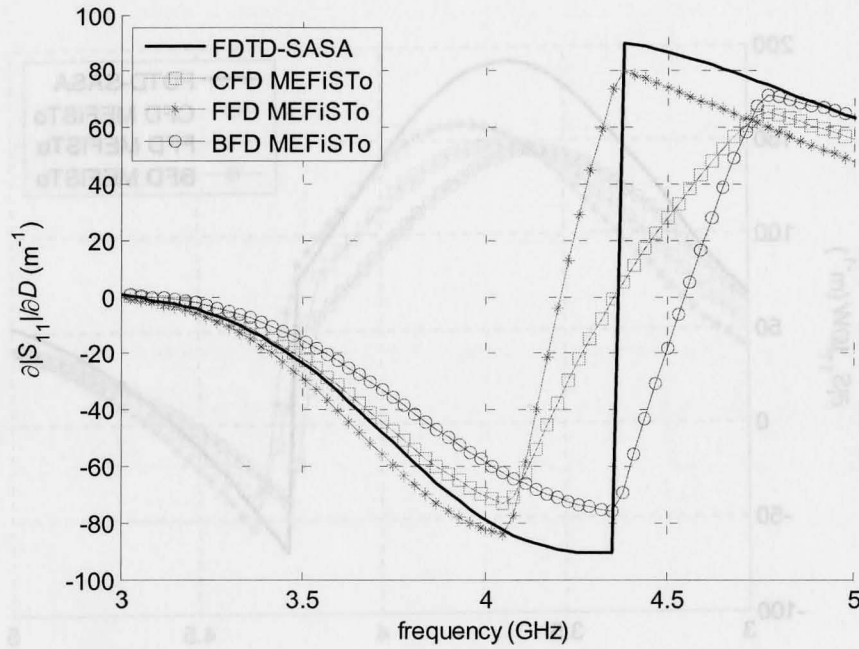


Figure 4.4. Derivatives of $|S_{11}|$ with respect to D in the single-resonator filter example.

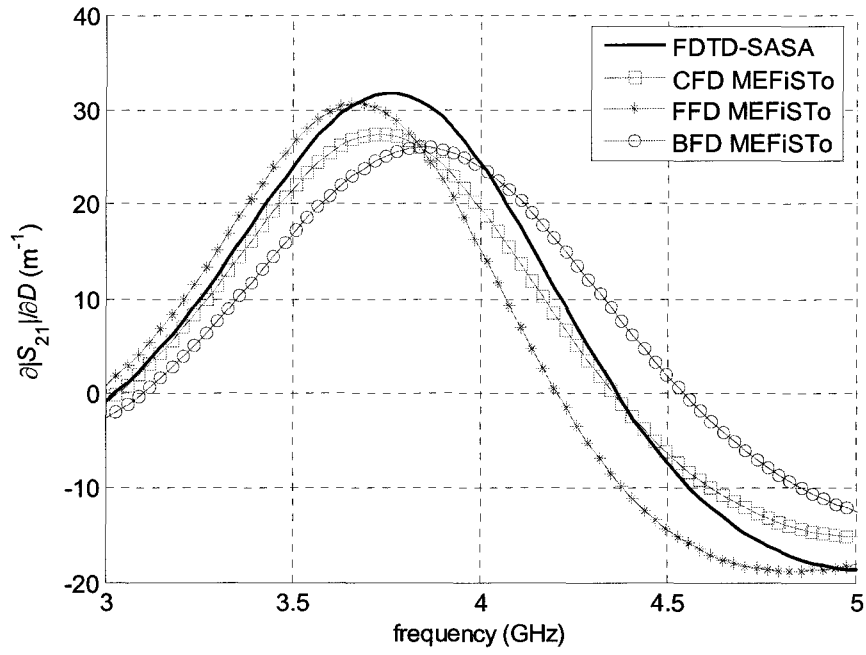


Figure 4.5. Derivatives of $|S_{21}|$ with respect to D in the single-resonator filter example.

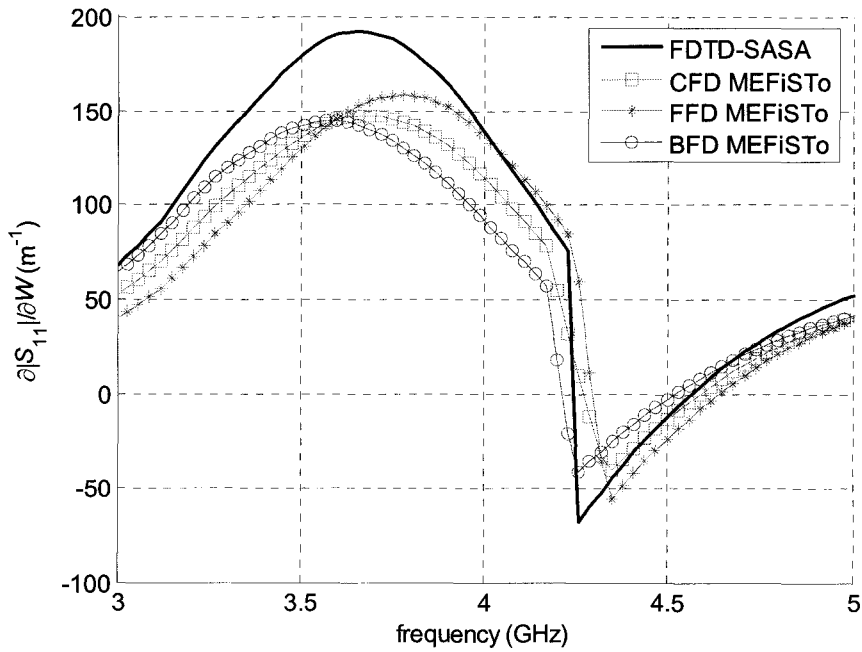


Figure 4.6. Derivatives of $|S_{11}|$ with respect to W in the single-resonator filter example.

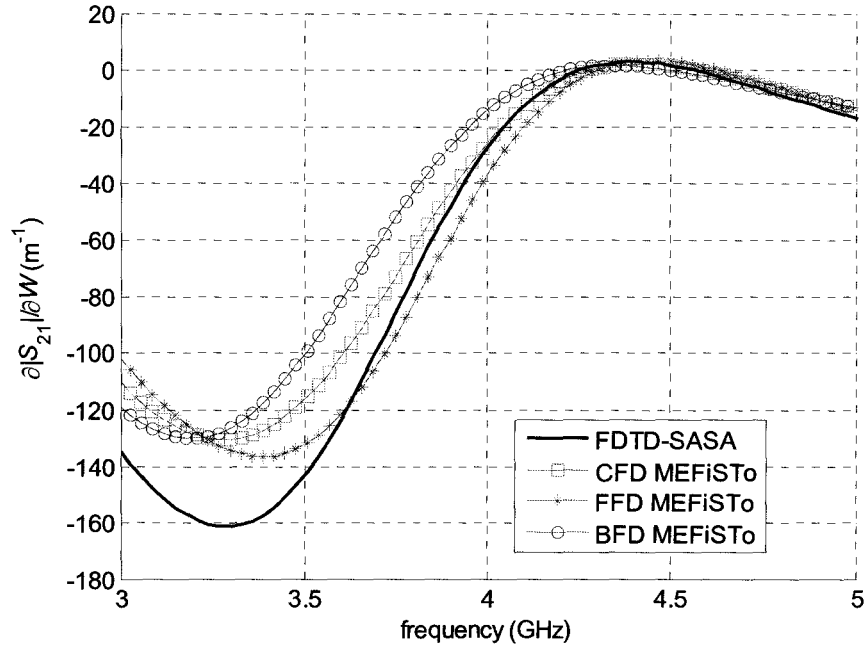


Figure 4.7. Derivatives of $|S_{21}|$ with respect to W in the single-resonator filter example.

4.6.2 Single-section Waveguide Impedance Transformer

The single-section waveguide impedance transformer is shown in Figure 3.18. The S -parameters with the nominal design are plotted in Figure 3.19. The setup of the MEFiSTo simulation is shown in Table 3.2. The AVM probes needed in the FDTD-based SASA algorithm are illustrated in Figure 4.8, when we assume an increase of L .

4.6.2.1 Frequency Sweep Sensitivity Analysis

We test our technique with the S -parameter sensitivity with respect to W and L at the optimal solution. We use the optimal solution of the commercial software HFSS

$[W_0 \ L_0]^T = [14\Delta h \ 10\Delta h]^T$ at $f_0 = 6.48$ GHz as the nominal design.

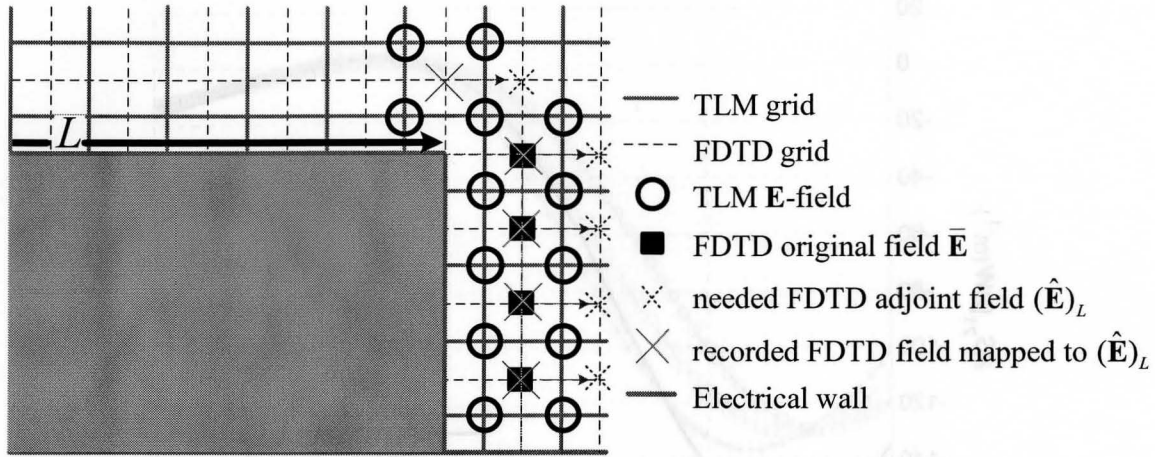


Figure 4.8. FDTD-based AVM probes (marked with circles) at the matching section boundaries (assume increasing L) in the waveguide impedance transformer example.

We first compute the sensitivity at the optimal W_0 and L_0 with a frequency sweep around the optimal frequency f_0 . The derivatives of $|S_{11}|$ and $|S_{21}|$ with respect to the length L are shown in Figure 4.9 and Figure 4.10. The results are compared with the HFSS finite-difference derivatives. From Figure 4.9, we see that the FFD and BFD curves show inferior accuracy of the first-order finite-difference approximations. For a given cell size, our results are less likely to suffer from an insufficiently refined grid. This is due to their second-order accuracy comparable to that of the CFD approximation. However, the adjoint sensitivity result of $|S_{21}|$ with respect to L in Figure 4.10 is worse than that of $|S_{11}|$ in Figure 4.9. We explore the case further by convergence analysis in the next section.

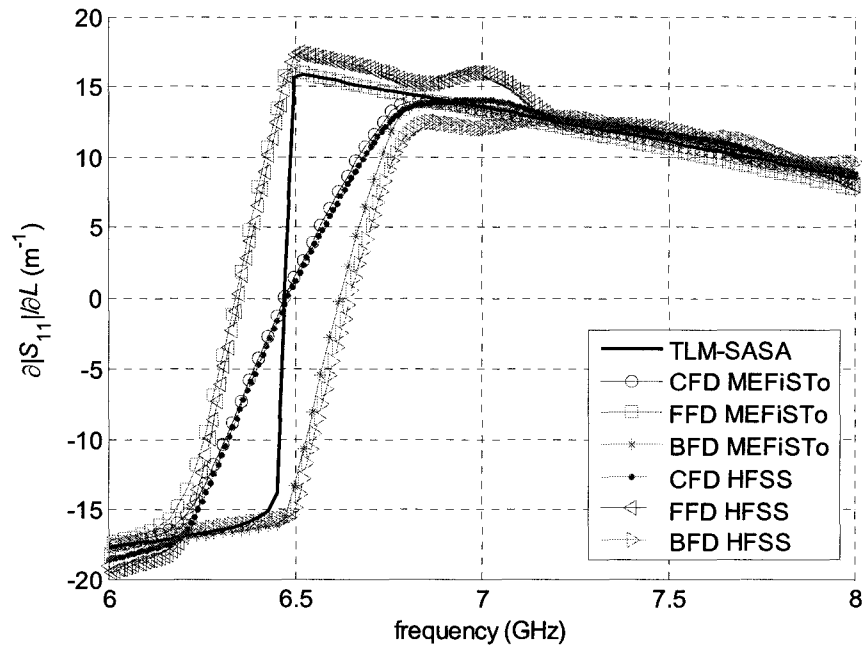


Figure 4.9. Derivatives of $|S_{11}|$ with respect to L in the waveguide impedance transformer example.

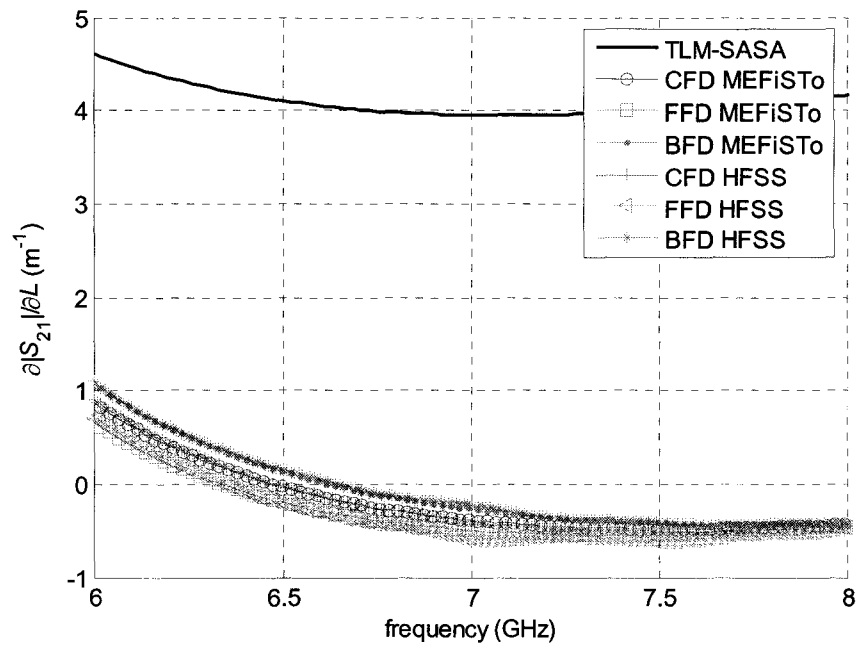


Figure 4.10. Derivatives of $|S_{21}|$ with respect to L in the waveguide impedance transformer example.

4.6.2.2 Convergence Analysis

We perform convergence analysis to illustrate the superior accuracy of the sensitivities computed with our approach as compared to those obtained by response-level finite differences.

The derivatives of $|S_{11}|$ and $|S_{21}|$ with respect to the section length L and width W with converging mesh sizes are shown in Figure 4.11, Figure 4.12, Figure 4.13 and Figure 4.14, respectively. As the mesh is refined twice and then four-fold, the TLM-SASA curve changes little and consistently shows zero derivatives at our estimated optimal frequency $f_0 = 6.48$ GHz. The CFD curves converge toward the FDTD-SASA curves as the mesh is refined.

From Figure 4.12 and Figure 4.14, we find the $|S_{21}|$ sensitivity results are worse than that of $|S_{11}|$, as also seen in Figure 4.10. As the mesh is refined, the FDTD-SASA curves converge toward the CFD curves. It seems that the accuracy of FDTD-SASA is worse than the accuracy of finite-difference methods in these cases. Note that the derivative of $|S_{21}|$ is much smaller than the derivatives of $|S_{11}|$. It appears that the accuracy of our AVM algorithm deteriorates when the absolute values of the derivatives are small, i.e., the objective function is insensitive with respect to the parameter perturbation. It consistently overestimates the derivative. The FDTD-SASA curve has the same frequency dependence as the finite-difference curves but seems to add a spurious value to the true derivative value.

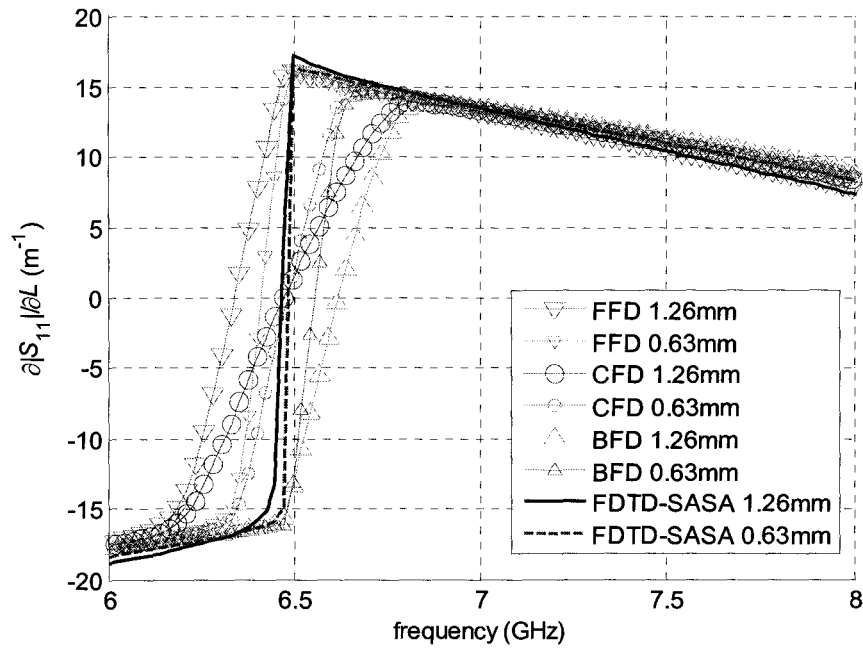


Figure 4.11. Convergence analysis of the derivatives of $|S_{11}|$ with respect to L in the waveguide impedance transformer example.

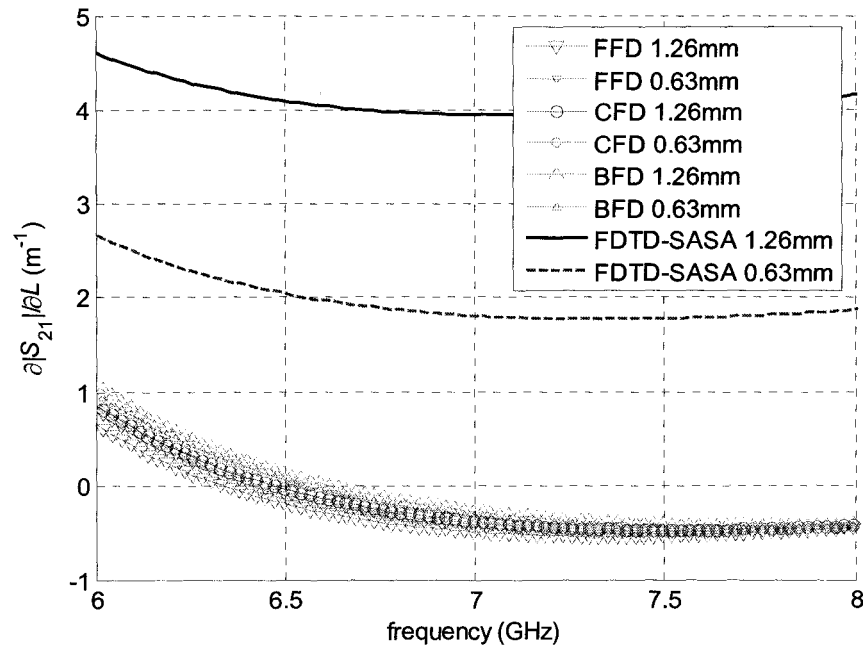


Figure 4.12. Convergence analysis of the derivatives of $|S_{21}|$ with respect to L in the waveguide impedance transformer example.

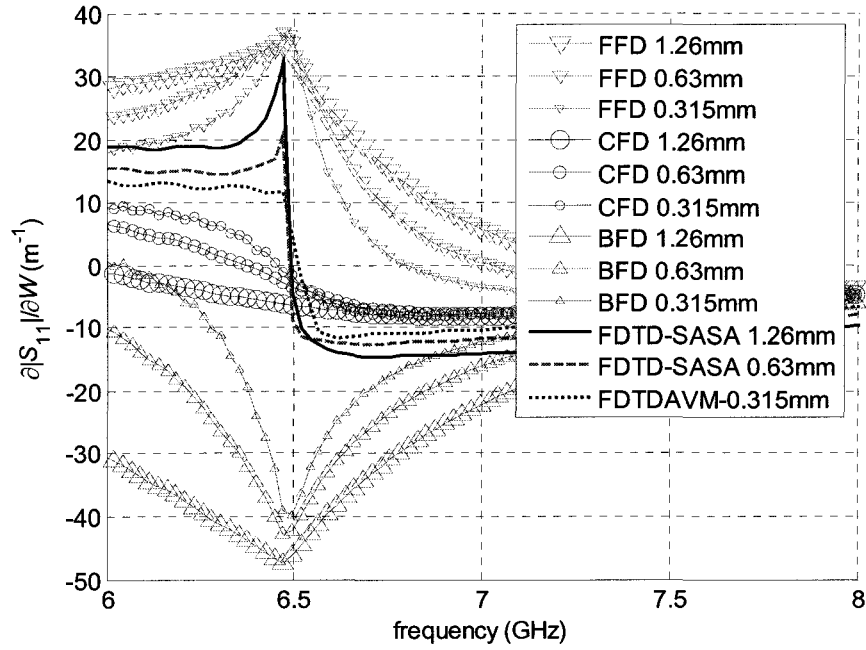


Figure 4.13. Convergence analysis of the derivatives of $|S_{11}|$ with respect to W in the waveguide impedance transformer example.

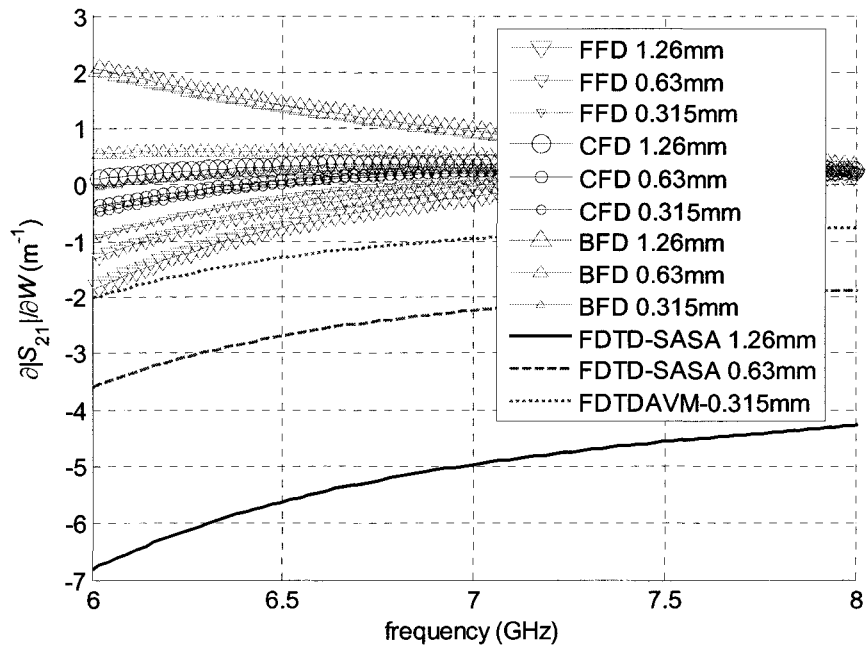


Figure 4.14. Convergence analysis of the derivatives of $|S_{21}|$ with respect to W in the waveguide impedance transformer example.

In the lossless case, we use the error function (3.23) to estimate the accuracy of the S -parameter sensitivities of different techniques. We can compute the error from the sensitivity results we obtained above. We show the error of the S -parameter derivatives with respect to W with a convergence analysis in Figure 4.15. We see that the overall error of the FDTD-SASA is much smaller than that of the CFD results and it is practically independent of frequency. It also seems that most of the FDTD-SASA error is due to the derivative of $|S_{21}|$ (see Figure 4.14) rather than the derivative of $|S_{11}|$ (see Figure 4.13).

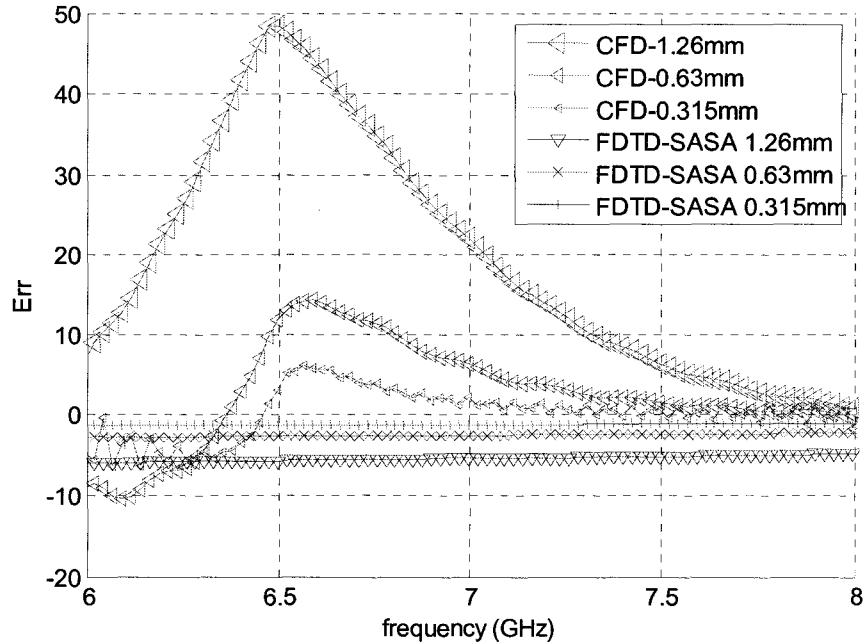


Figure 4.15. Convergence analysis of the error with respect to W in the waveguide impedance transformer example.

4.6.2.3 Parameter Sweep Sensitivity Analysis

Finally, we perform a parameter sweep and compare the derivatives of the FDTD-SASA technique and the MEFiSTo/HFSS finite-difference approximations. We sweep L and W around their optimal values for $f = f_0$. The sensitivities of $|S_{11}|$ and $|S_{21}|$ are shown in Figure 4.16, Figure 4.17, Figure 4.18 and Figure 4.19.

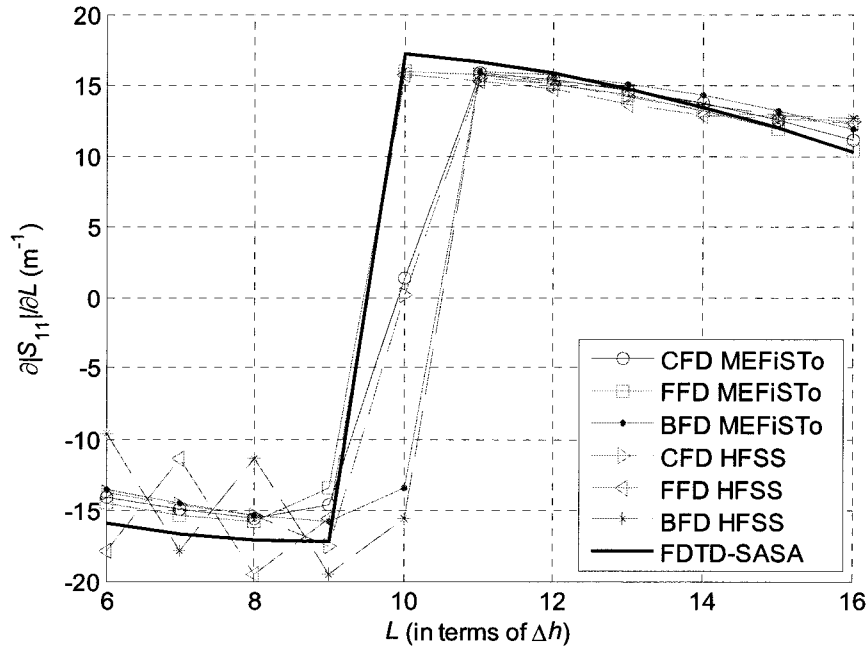


Figure 4.16. Derivatives of $|S_{11}|$ with respect to L in the waveguide impedance transformer example (parameter sweep of L).

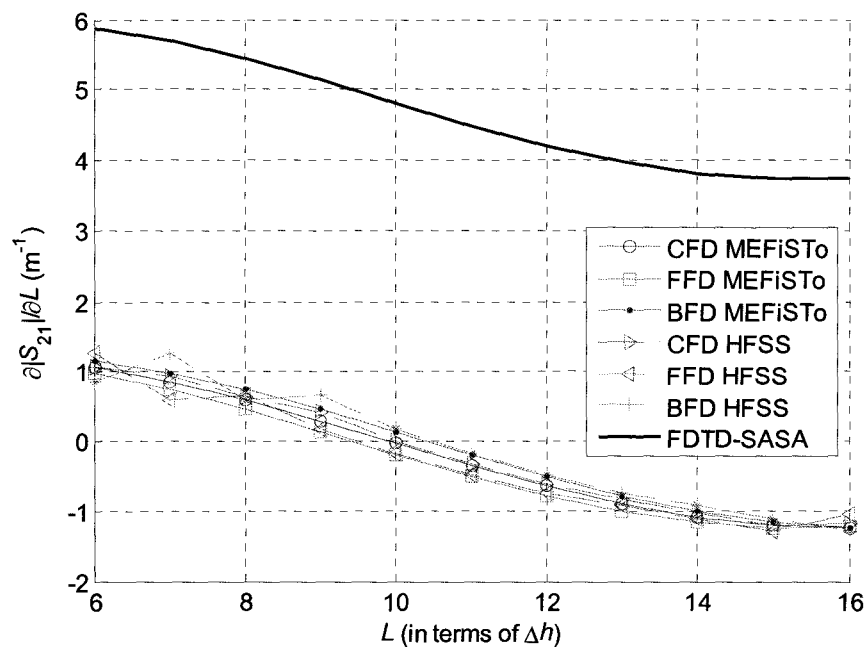


Figure 4.17. Derivatives of $|S_{21}|$ with respect to L in the waveguide impedance transformer example (parameter sweep of L).

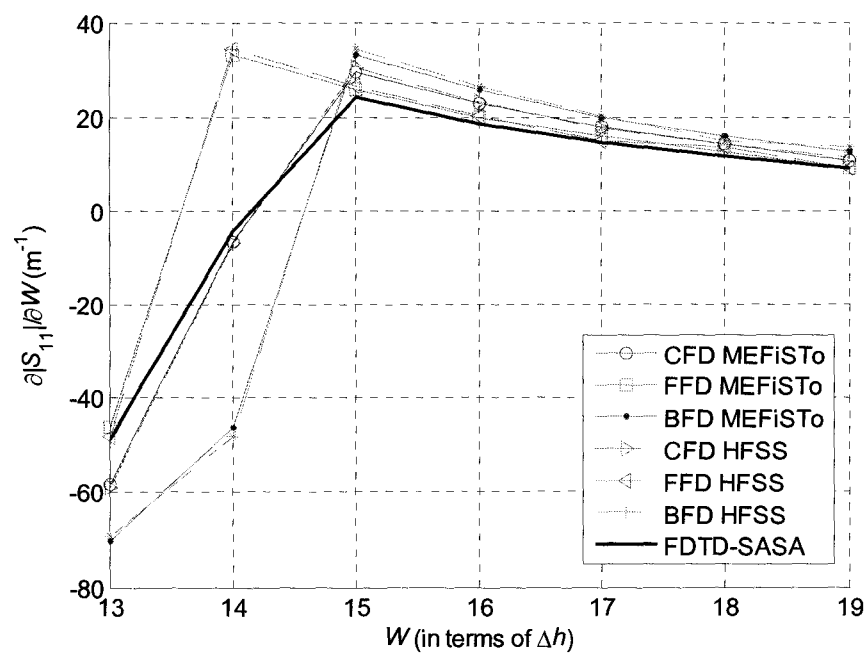


Figure 4.18. Derivatives of $|S_{11}|$ with respect to W in the waveguide impedance transformer example (parameter sweep of W).

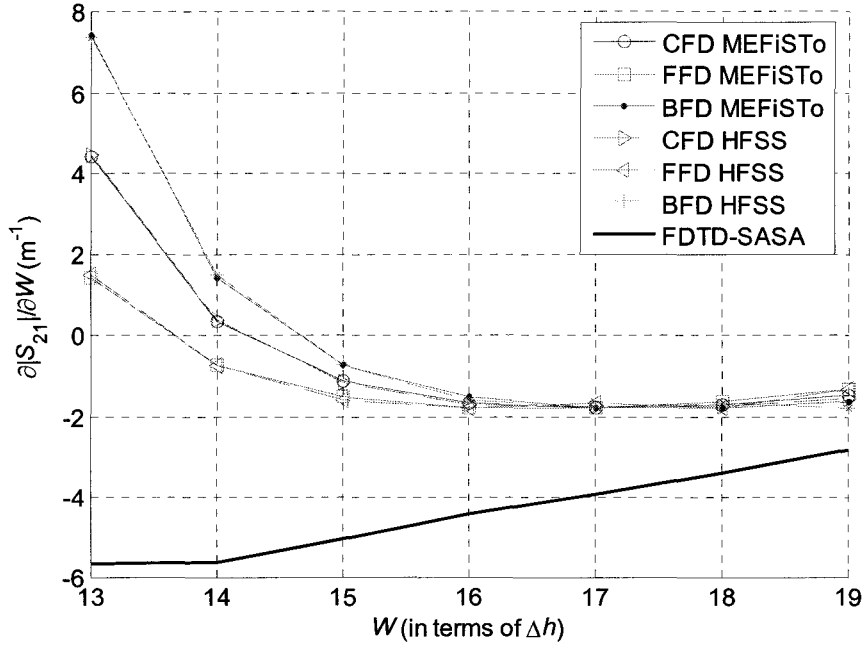


Figure 4.19. Derivatives of $|S_{21}|$ with respect to W in the waveguide impedance transformer example (parameter sweep of W).

4.6.2.4 Computational Overhead

The CPU time for calculating the sensitivity per one parameter is shown in Table 4.1. The processor of the computer is Pentium 4 at 3 GHz clock frequency. The post-process is conducted in MATLAB [8]. In the MEFiSTo simulations, we request the least number of discrete Fourier Transform (FT) points for the field waveforms of the probes, so that the simulations are not delayed by the extra processing. As seen from Table 4.1, the simulation time in MEFiSTo does not depend much on the number of AVM probes. However, if we request multiple-point discrete FT, the simulation time in MEFiSTo grows significantly as the probe number increases.

Table 4.1. CPU time for the waveguide impedance transformer example

	Obtain sensitivity with respect to W	Obtain sensitivity with respect to L	Without probes
A VM Probe number	36	24	0
Simulation time in MEFiSTo (seconds)	160.969	159.250	158.171
CPU time per adjoint sensitivity calculation (seconds)	0.7812	0.5937	

The memory requirements of the sensitivity analysis are mostly due to the field waveforms recorded at the perturbation points. The number of these points is roughly equal to the number of cells surrounding a perturbation surface or line. MEFiSTo exports the field components through text files after the simulation is completed.

The CPU time of the post-process for obtaining the adjoint sensitivities is much less than the simulation time of the full-wave EM analysis. The FFD or BFD approximations require N additional EM system analyses (each involving K simulations for the K ports), while our approach can provide the same information at a fraction of the time required by one EM simulation. In conclusion, our approach to S -parameter sensitivity analysis is far more computationally efficient than the finite-difference approximations.

4.6.3 Dielectric-resonator Filter

This filter [9] consists of three identical ceramic blocks located asymmetrically at one of the waveguide walls. An H -plane view is shown in Figure 4.20. The vertical extent of the ceramic posts is the same as the waveguide height. Thus, the 2D TM_x analysis is feasible for the modes, which do not vary with x . We extract the S -parameters and their sensitivities for the dominant $\text{TE}_z^{(01)}$ mode. The shape parameters of interest are the posts' width w , length r , and inter-post separation s . The nominal shape parameters $\mathbf{p}^T = [r \quad w \quad s]$ are given in the inset of Figure 4.20.

The S -parameters computed from the field solutions of MEFiSTo and HFSS are compared in Figure 4.21 for the nominal design. The setup of the MEFiSTo simulation is summarized in Table 4.2. The probes needed for the derivative with respect to the shape parameter w with forward and backward perturbations are shown in Figure 4.22. The location of the probes needed for the perturbation of s is similar to Figure 4.2.

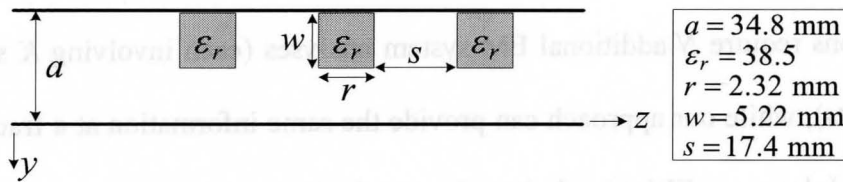
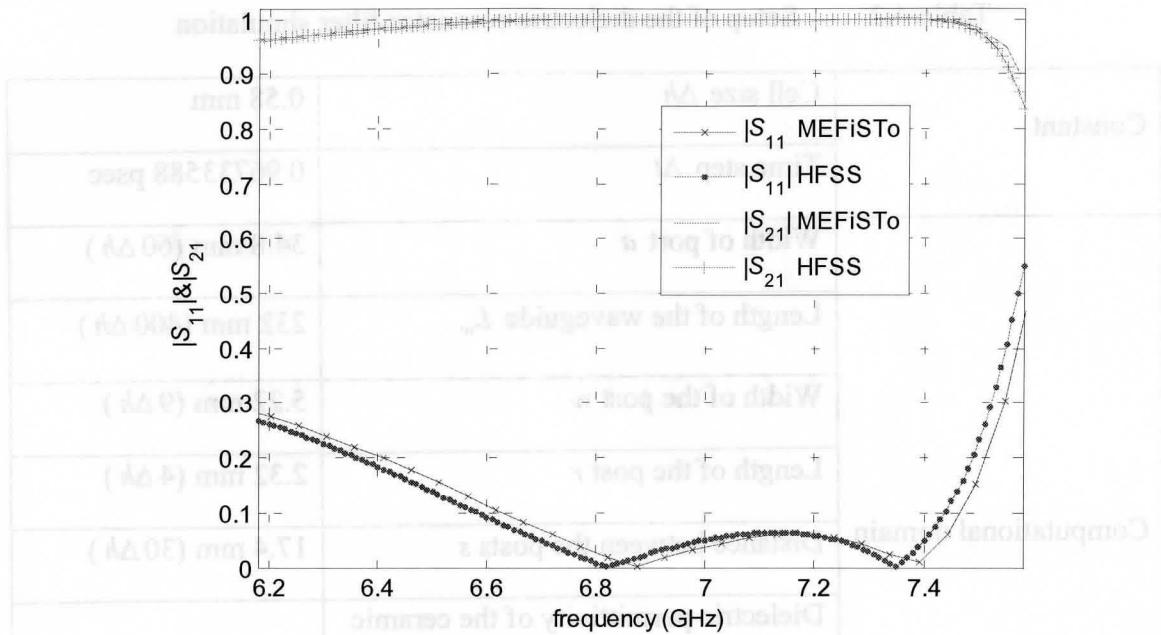
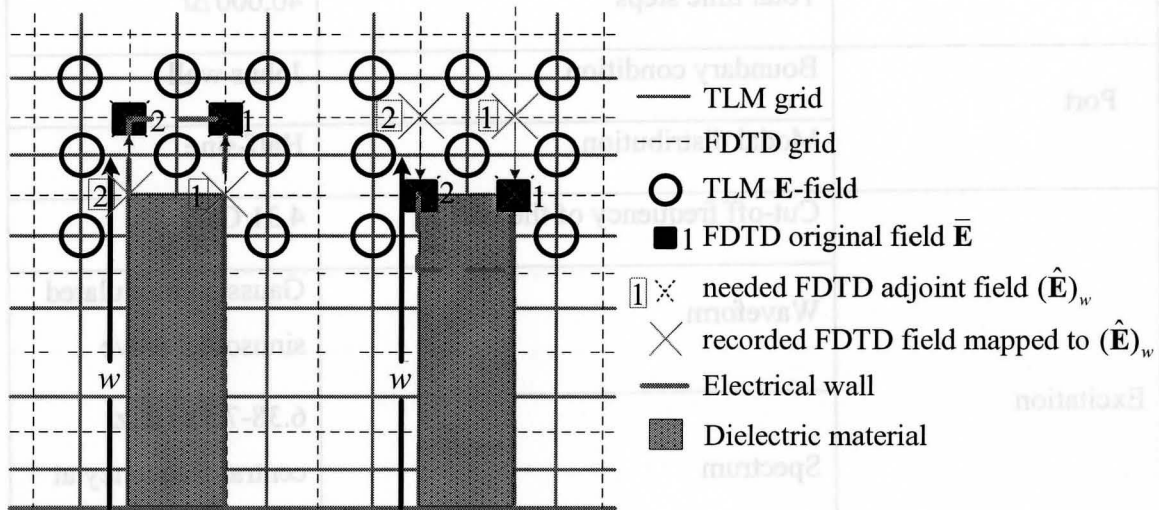


Figure 4.20. H -plane view of the dielectric-resonator filter

Table 4.2. Setup of the dielectric-resonator filter simulation

Constant	Cell size Δh	0.58 mm
	Time step Δt	0.96733588 psec
Computational domain	Width of port a	34.8 mm (60 Δh)
	Length of the waveguide L_w	232 mm (400 Δh)
	Width of the post w	5.22 mm (9 Δh)
	Length of the post r	2.32 mm (4 Δh)
	Distance between the posts s	17.4 mm (30 Δh)
	Dielectric permittivity of the ceramic blocks ϵ_r	38.5
	Computational domain in space	400 $\Delta h \times 60 \Delta h$
	Total time steps	40,000 Δt
Port	Boundary condition	Johns wall
	Modal distribution	Half-sine
Excitation	Cut-off frequency of the port	4.31 GHz
	Waveform	Gaussian modulated sinusoidal wave
	Spectrum	6.38-7.38 GHz, central frequency at 6.88 GHz
	Port distribution	Half-sine
Probes	Distance from the respective port	20 Δh

Figure 4.21 S -parameters of the dielectric-resonator filterFigure 4.22. FDTD-based AVM probes (marked with circles) at the post boundaries (left post assume increasing w , right post assume decreasing w) in the dielectric-resonator filter example.

4.6.3.1 Frequency Sweep Sensitivity Analysis

We first compute the sensitivity with respect to the parameters with a frequency sweep. The derivatives of $|S_{11}|$ and $|S_{21}|$ with respect to the width of the post w are shown in Figure 4.23 and Figure 4.24. The derivatives of $|S_{11}|$ and $|S_{21}|$ with respect to the distance between the posts s are shown in Figure 4.25 and Figure 4.26. The results are compared with the MEFiSTo finite differences. All other parameters are kept at their nominal values.

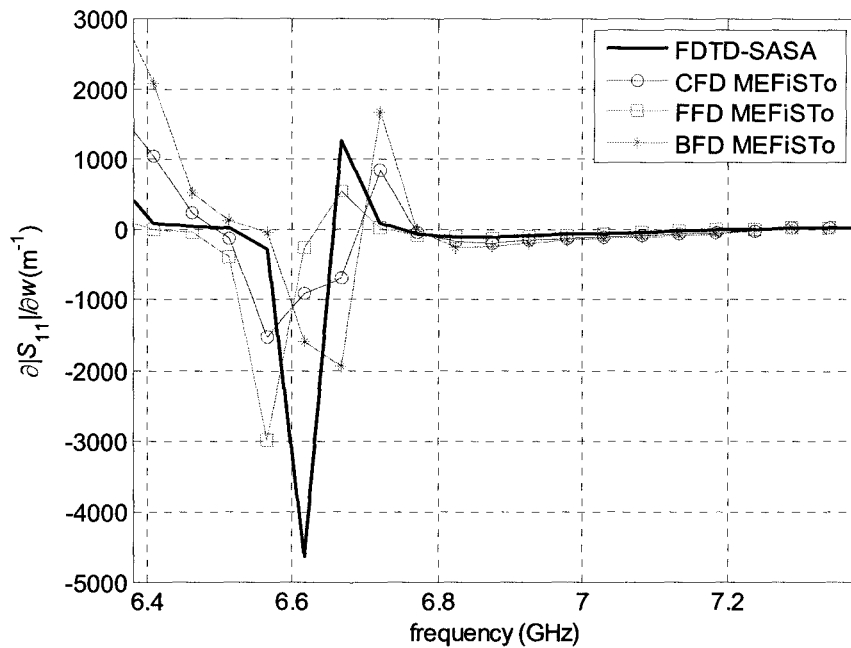


Figure 4.23. Derivatives of $|S_{11}|$ with respect to w in the dielectric-resonator filter example.

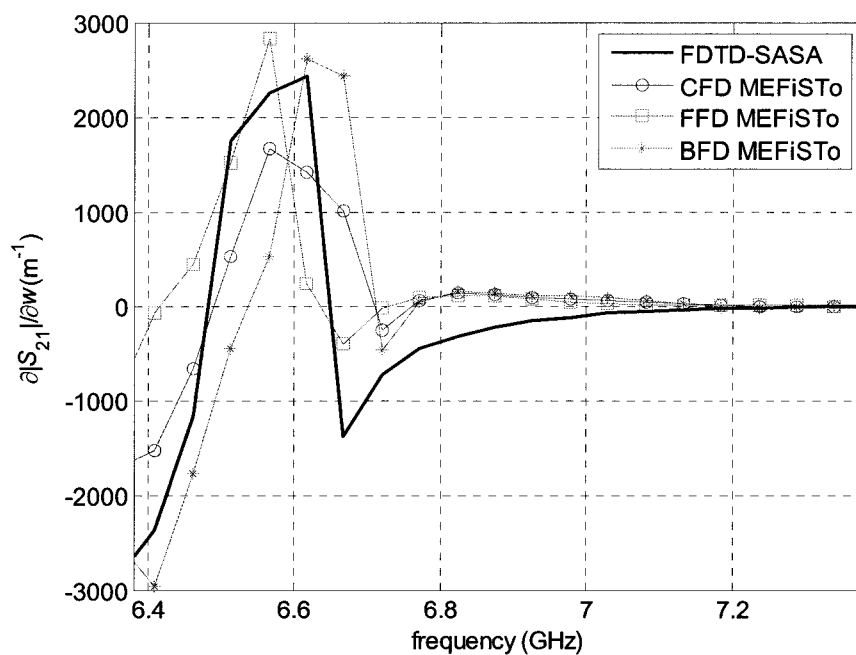


Figure 4.24. Derivatives of $|S_{21}|$ with respect to w in the dielectric-resonator filter example.

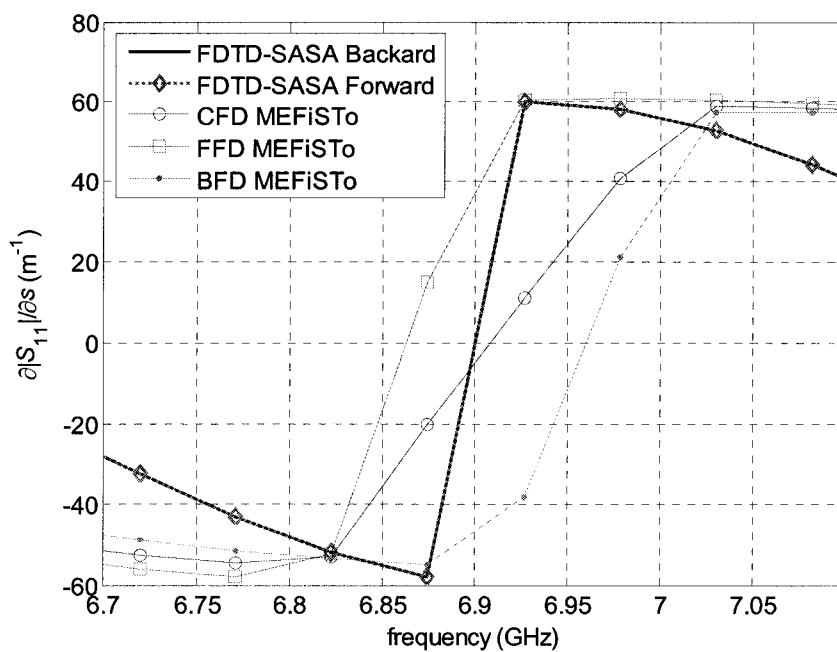


Figure 4.25. Derivatives of $|S_{11}|$ with respect to s in the dielectric-resonator filter example.

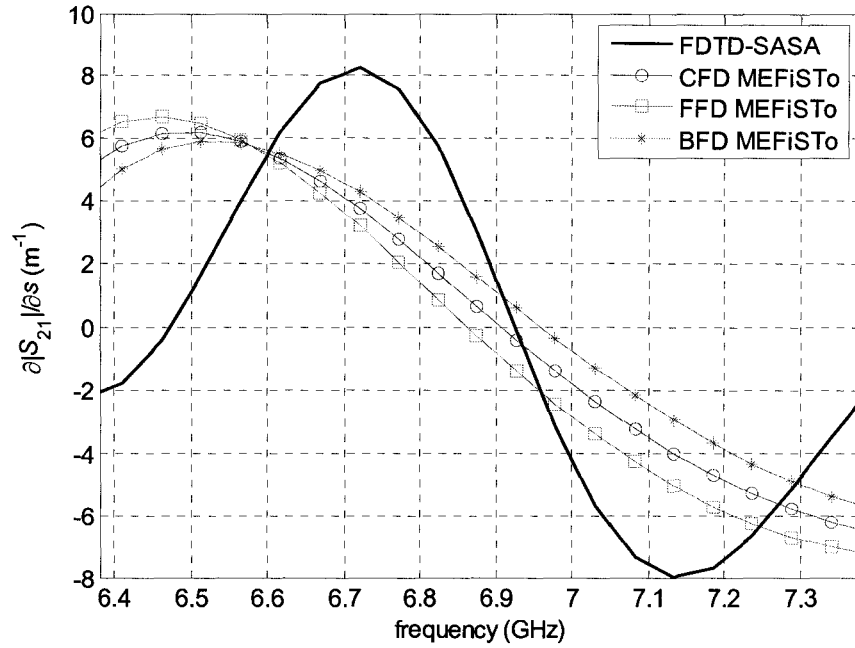


Figure 4.26. Derivatives of $|S_{21}|$ with respect to s in the dielectric-resonator filter example.

In Figure 4.25, the adjoint sensitivity curves obtained by assuming forward perturbation of the parameter (increasing the value of the parameter) and backward perturbation of the parameter (decreasing the value of the parameter) are marked as FDTD-SASA Forward and FDTD-SASA Backward, respectively. We can see that with both backward and forward assumed perturbations, the AVM algorithm gives almost the same results. The differences are less than 10^{-7} times the derivatives themselves.

In general, we find that with a high dielectric constant material the SASA results are still in agreement with the finite differences, although not as well as in the case of metallic objects in homogeneous dielectrics. We also find that when the S -parameters change very little, i.e. they are insensitive, the accuracy of the AVM result deteriorates, as indicated in Figure 4.26.

4.6.3.2 Parameter Sweep Sensitivity Analysis

We perform a parameter sweep and compare the derivatives of the FDTD-SASA technique and the MEFiSTo/HFSS finite-difference approximation. We vary w and s around the nominal design. The sensitivities of $|S_{11}|$ and $|S_{21}|$ with respect to w for a sweep of w are shown in Figure 4.27 and Figure 4.28, respectively. The sensitivities of $|S_{11}|$ and $|S_{21}|$ with respect to s for a sweep of s are shown in Figure 4.29 and Figure 4.30, respectively. The sensitivities of $|S_{11}|$ and $|S_{21}|$ with respect to w for a sweep of s are shown in Figure 4.31 and Figure 4.32, respectively. The sensitivities of $|S_{11}|$ and $|S_{21}|$ with respect to s for a sweep of w are shown in Figure 4.33 and Figure 4.34, respectively.

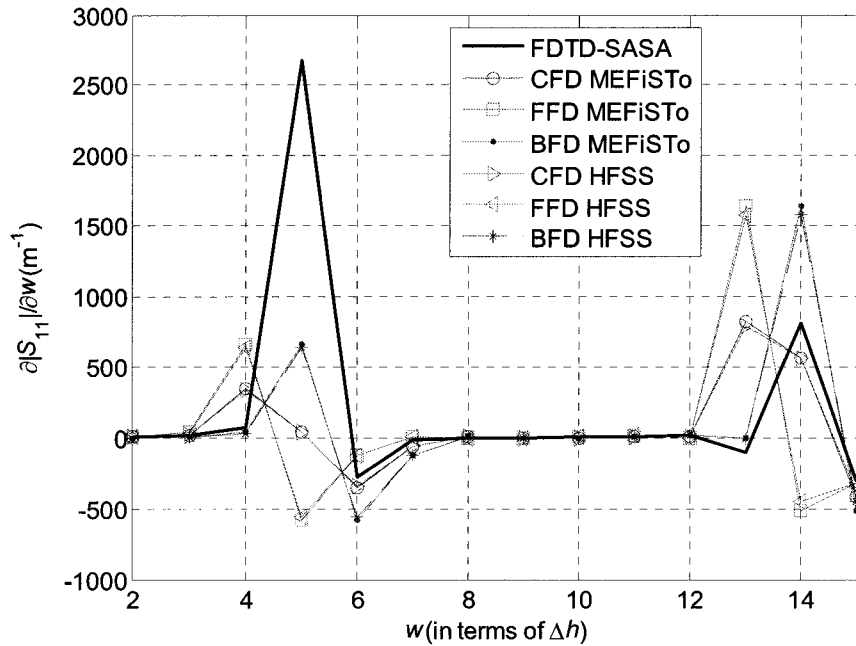


Figure 4.27. Derivatives of $|S_{11}|$ with respect to w in the dielectric-resonator filter example (parameter sweep of w).

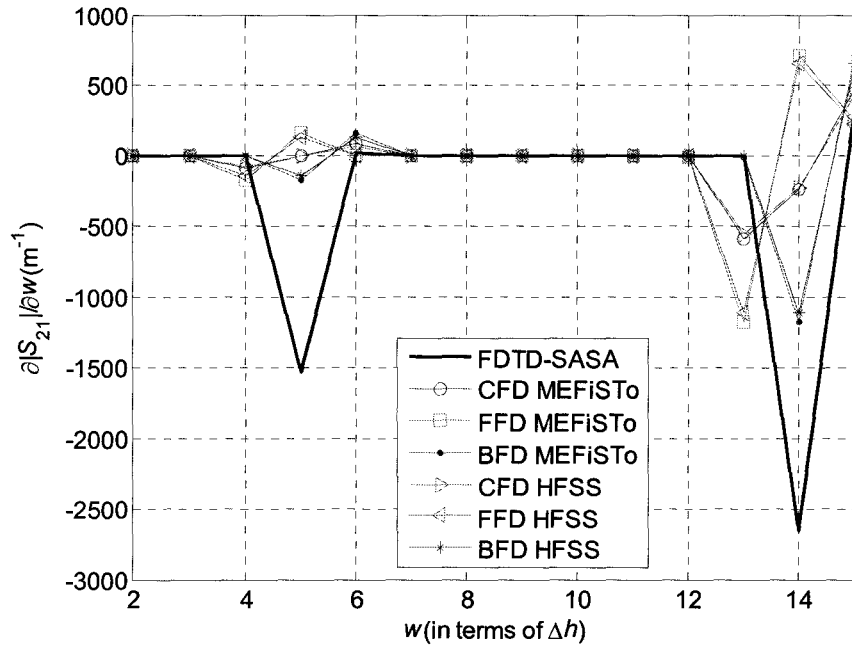


Figure 4.28. Derivatives of $|S_{21}|$ with respect to w in the dielectric-resonator filter example (parameter sweep of w).

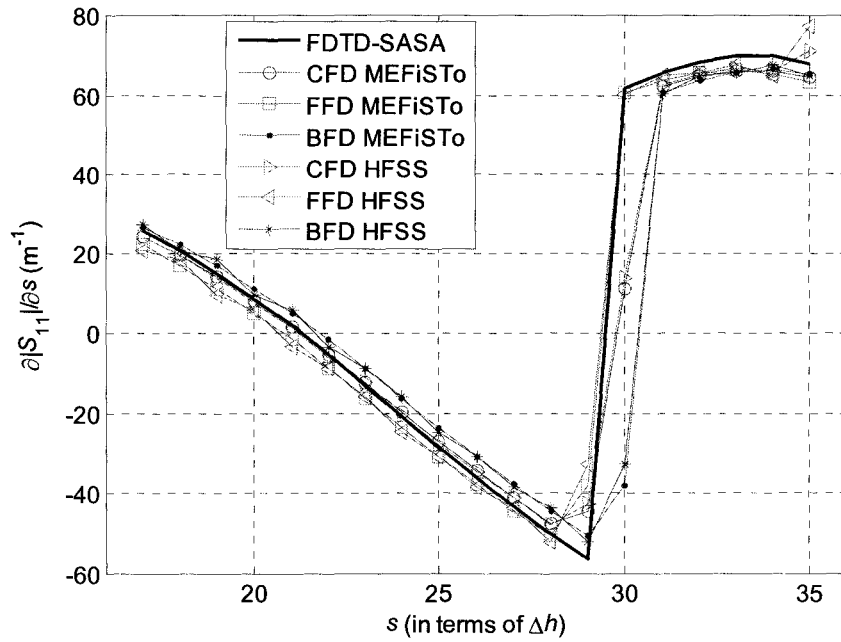


Figure 4.29. Derivatives of $|S_{11}|$ with respect to s in the dielectric-resonator filter example (parameter sweep of s).

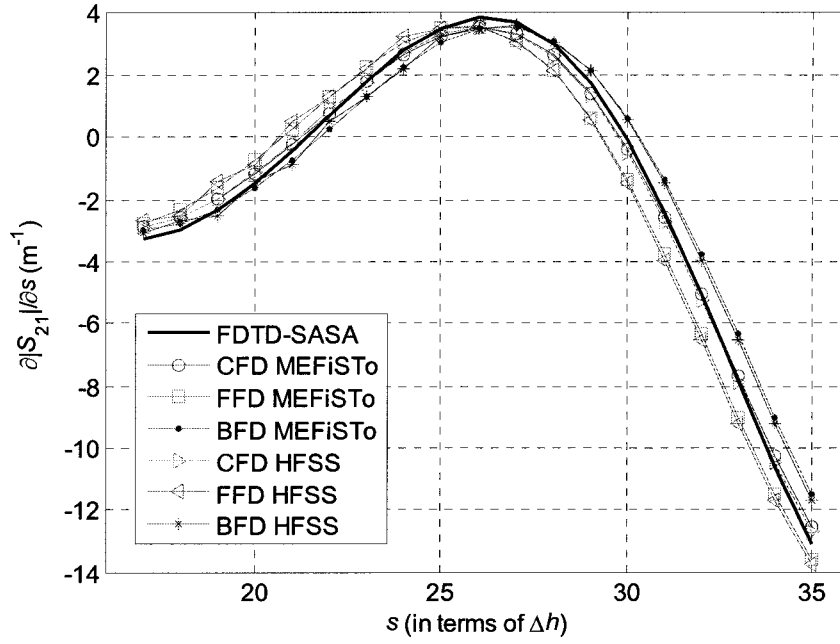


Figure 4.30. Derivatives of $|S_{21}|$ with respect to s in the dielectric-resonator filter example (parameter sweep of s).

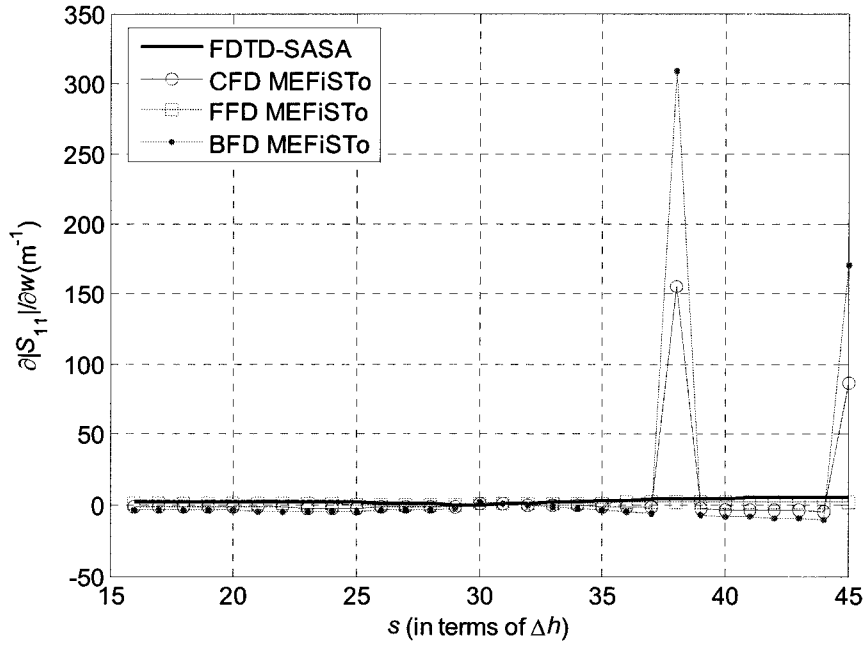


Figure 4.31. Derivatives of $|S_{11}|$ with respect to w in the dielectric-resonator filter example (parameter sweep of s).

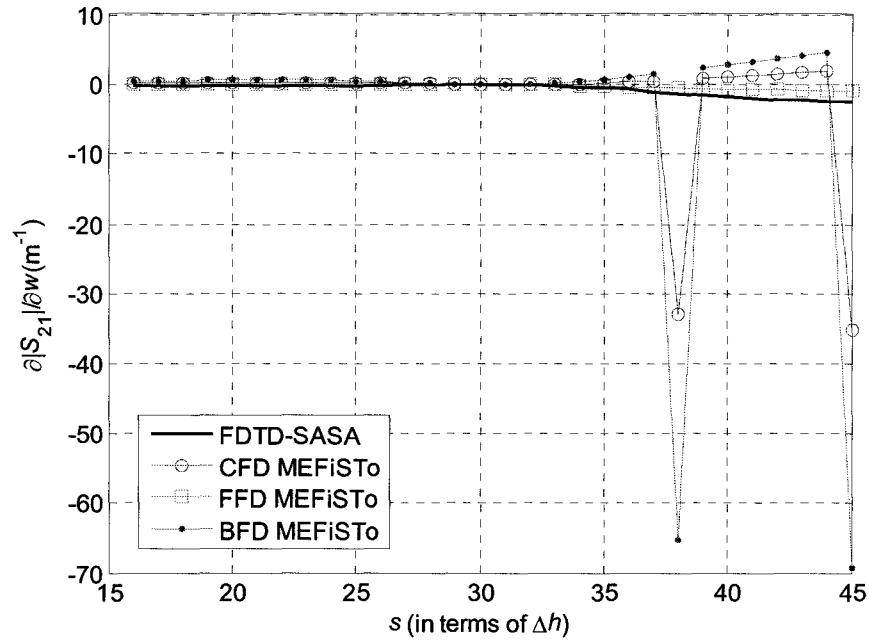


Figure 4.32. Derivatives of $|S_{21}|$ with respect to w in the dielectric-resonator filter example (parameter sweep of s).

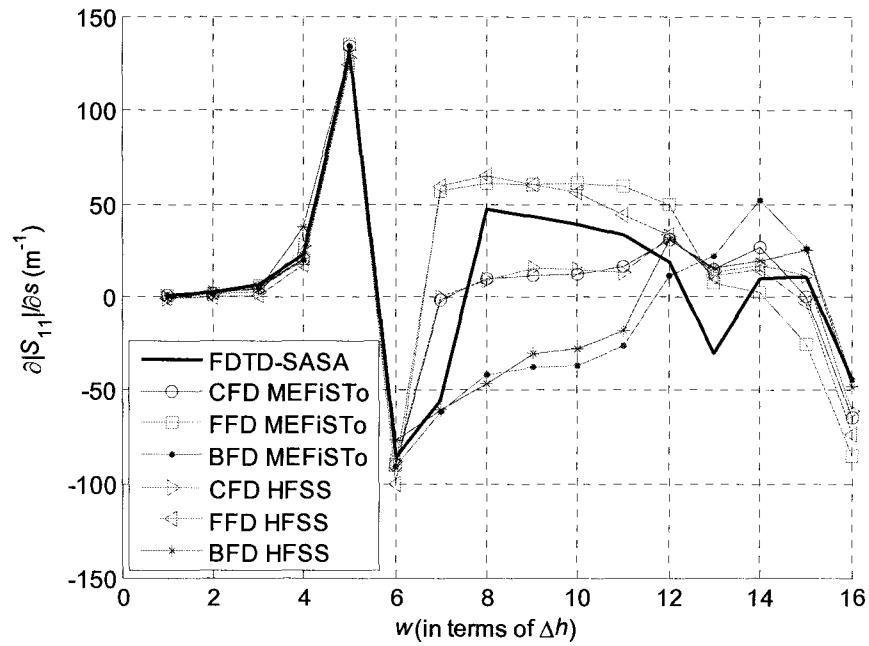


Figure 4.33. Derivatives of $|S_{11}|$ with respect to s in the dielectric-resonator filter example (parameter sweep of w).

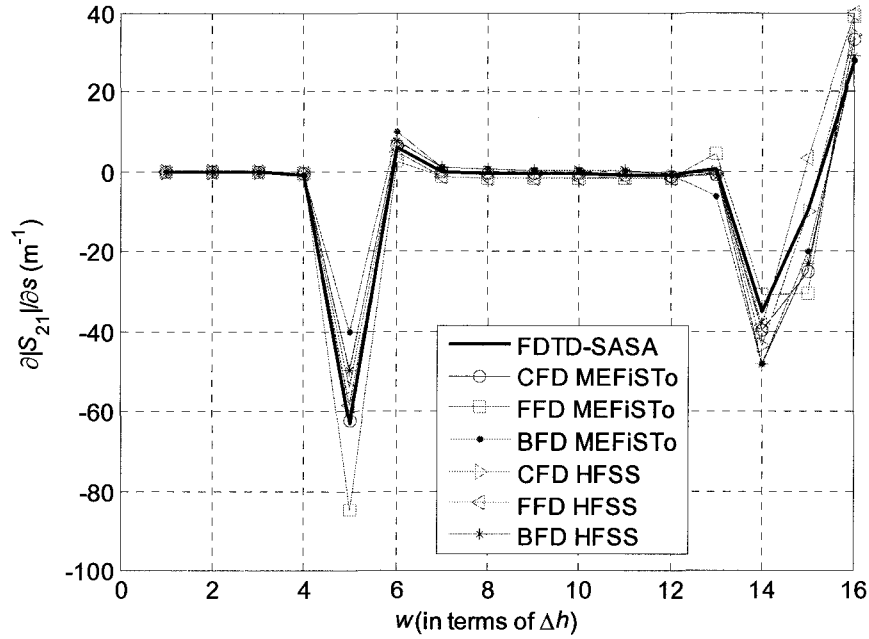


Figure 4.34. Derivatives of $|S_{21}|$ with respect to s in the dielectric-resonator filter example (parameter sweep of w).

4.6.3.3 Computational Overhead

The CPU time required to calculate the derivative with respect to one parameter is shown in Table 4.3. The setup is the same as in the waveguide impedance transformer example. From this table, we reach our conclusion that our approach to S -parameter sensitivity analysis is far more computationally efficient than the finite-difference approximations.

Table 4.3. CPU time for the dielectric-resonator filter example

	Obtain sensitivity with respect to s	Obtain sensitivity with respect to w	Without probes
Probe number	120	54	0
Simulation time in MEFiSto (seconds)	213.391	187.281	168.703
Simulation time in MEFiSto (seconds))	173.344	169.453	166.360
CPU time per adjoint S_{11} sensitivity calculation (seconds)	2.6875	1.1875	
CPU time per adjoint S_{21} sensitivity calculation (seconds)	1.0486	0.5000	

4.6.4 Dielectric-resonator Antenna

The dielectric-resonator antenna [9] is shown in Figure 4.35. It is coupled to the feeding microstrip line through an aperture in the ground plane. The microstrip is etched on the opposite side of the ground plane. The rectangular dielectric resonator has its bottom face centered onto the aperture.

This structure represents a demanding computational task. It is simulated in the 3D mode of MEFiSto. The symmetry of the antenna is exploited and only half of it is simulated. The computed return loss of the antenna is shown in Figure 4.36. The shape parameters of interest are the length a , width b and height c of the dielectric resonator, the length of the open-end stub l_s , as well as the width w_a and the length of the coupling

aperture l_a , i.e., $\mathbf{p}^T = [a \ b \ c \ l_s \ w_a \ l_a]$ The setup of the MEFiSto simulation of

the dielectric-resonator antenna is summarized in Table 4.4.

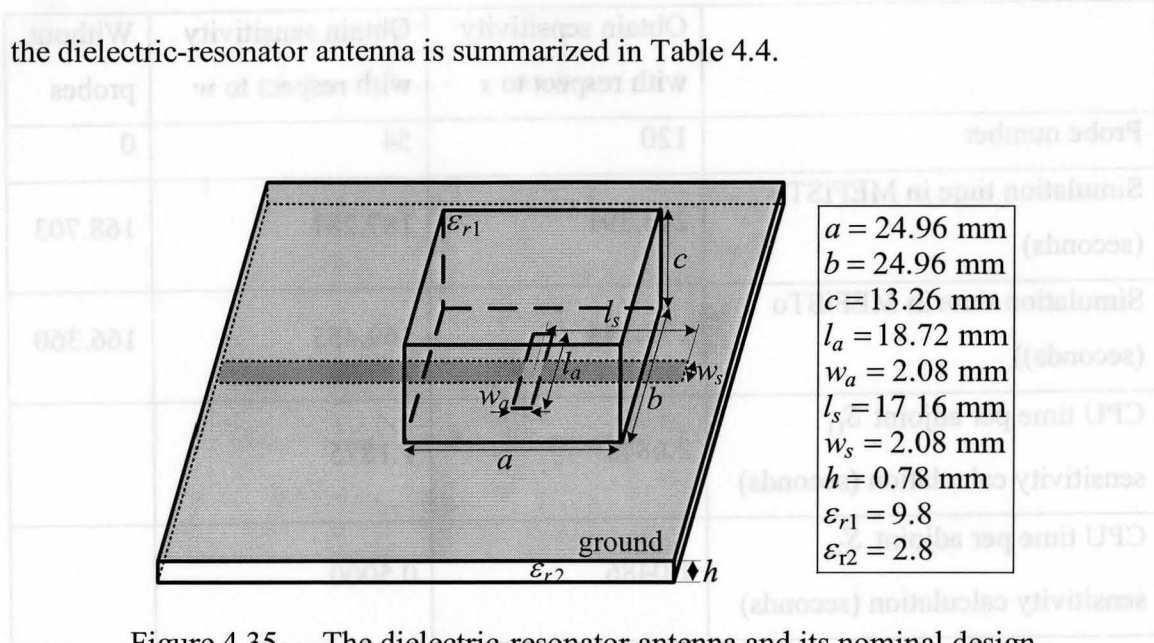


Figure 4.35. The dielectric-resonator antenna and its nominal design.

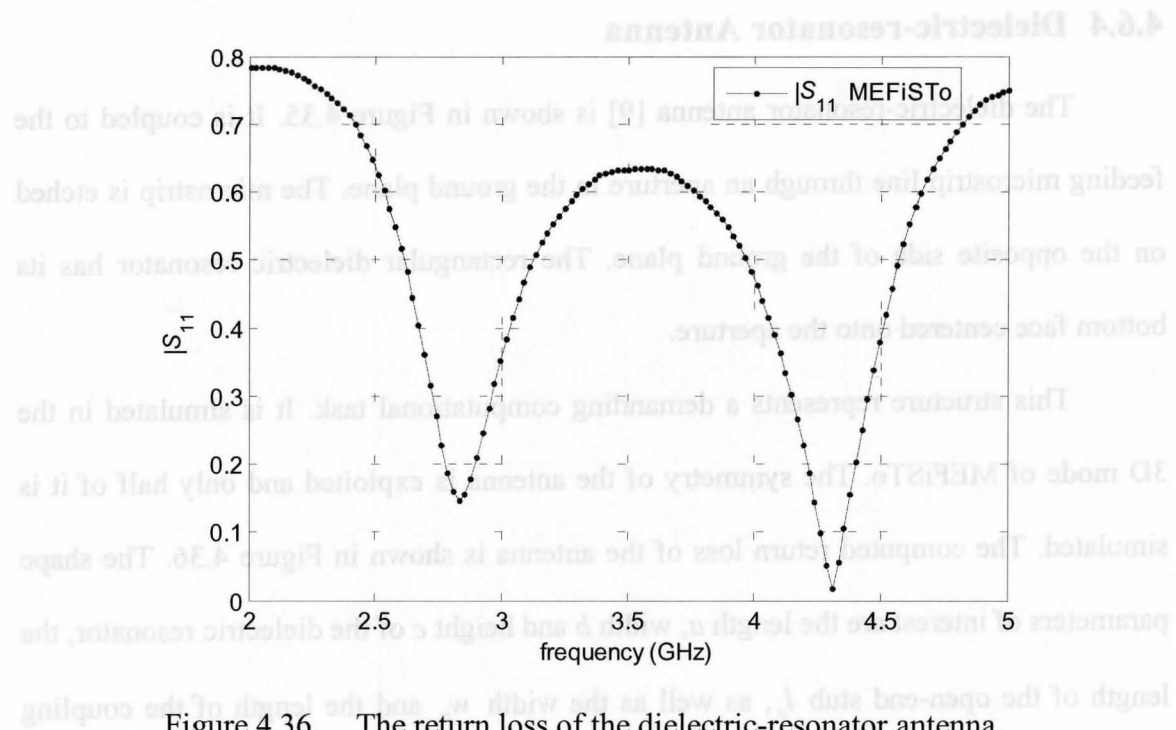


Figure 4.36. The return loss of the dielectric-resonator antenna.

Table 4.4. Setup of the dielectric-resonator antenna. simulation

Constant	Cell size Δh	0.26 mm
	Time step Δt	0.43363 psec
Computational domain	Length of the resonator a	24.96 mm (96 Δh)
	Width of the resonator b	24.96 mm (96 Δh)
	Height of the resonator c	13.26 mm (51 Δh)
	Dielectric permittivity of the resonator $\epsilon_{r,1}$	9.8
	Length of the open-end stub l_s	17.16 mm (66 Δh)
	Width of the open-end stub w_s	2.08 mm (8 Δh)
	Dielectric permittivity of the substrate $\epsilon_{r,2}$	2.8
	Width of the coupling aperture w_a	2.08 mm (8 Δh)
	Length of the coupling aperture l_a	18.72 mm (72 Δh)
	Computational domain in space	264 $\Delta h \times 144 \Delta h \times 111 \Delta h$
	Total time steps	30,000 Δt
Port	Boundary condition	TEM wave absorbing boundary
	Modal distribution	Constant
Excitation	Waveform	Gaussian wave
	Spectrum	HPBW 20 GHz
	Port distribution	Constant
Probes	Distance from the respective port	24 Δh

4.6.4.1 Sensitivity Analysis

The derivative of the return loss with respect to the antenna height c is plotted in Figure 4.37. The agreement between the finite-difference curves and our results is good. We note that the finite-difference curves are computed with a perturbation of $\delta c = 4\Delta h$ to remove the fluctuations. For the SASA calculation the assumed perturbation is $\delta c = \Delta h$ as before.

Due to the limitation of memory, we can not place more than about 150 probes in the MEFiSTo simulation; otherwise, the system fails. To obtain derivatives with respect to c , we need AVM probes all over the upper face of the resonator. If we place probes at each node of the current mesh, where the probe mesh size is $\Delta h_p = \Delta h = 0.26$ mm, then we will need $(a/\Delta h_p + 1) \times (b/2/\Delta h_p + 1) \times 3 = (97 \times 25 \times 3) = 7275$ probes for each E -field component when symmetry is exploited. Obviously, this cannot be implemented with MEFiSTo on this computer. So, we have to increase the probe mesh size to $\Delta h_p = 12\Delta h$. Then, the probe number needed becomes $(a/\Delta h_p + 1) \times (b/2/\Delta h_p + 1) \times 3 = (9 \times 5 \times 3) = 135$, which is acceptable for a single E -field component. We need to perform 3 times the same simulation to record E_x , E_y and E_z .

To improve the accuracy of the adjoint sensitivity results, we need more AVM probes. With the limitation of the probe number, we can only do more simulations with the probes placed in between the probes of the previous simulations. We perform additional 3 sets of simulations, with all the probes displaced in space one-half probe mesh size $\Delta h_p/2$ along each axis on the upper face of the resonator. Then, we interpolate

all 4 sets of the probe fields. This is equivalent to having twice finer probe mesh size. This final result is the one plotted in Figure 4.37.

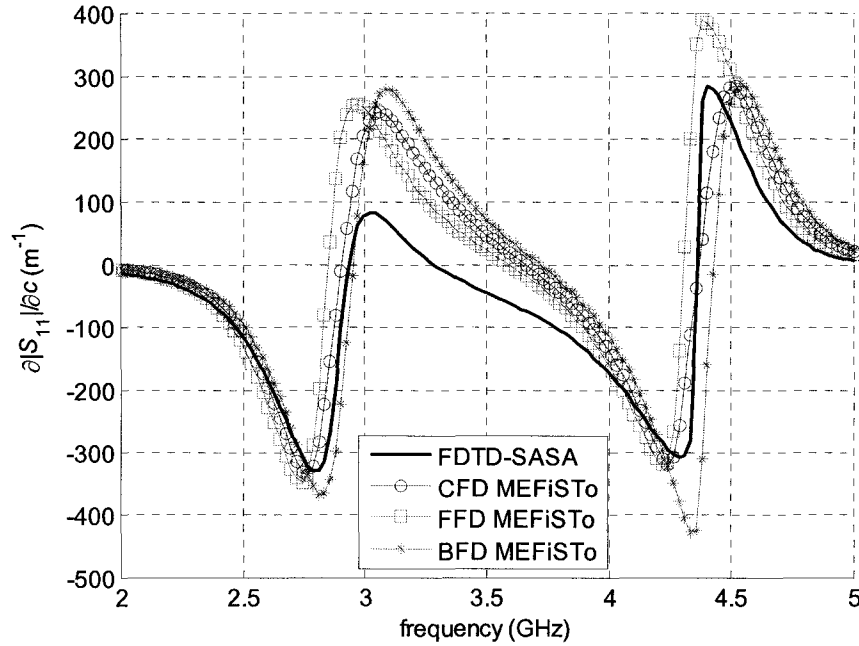


Figure 4.37. The derivative $|S_{11}|$ with respect to c of the dielectric-resonator antenna.

4.6.4.2 Computational Overhead

In this example, the advantages of the self-adjoint sensitivity analysis are the most obvious. The simulation of the dielectric-resonator antenna requires about 12 hours. In the same time, the computation of its response derivative $\partial|S_{11}|/\partial c$ shown in Figure 4.37 requires only about 4 minutes per frequency point despite the large number of probes necessary to cover the whole area of the top face of the dielectric resonator. In any

case, the EM simulation is significantly more demanding in terms of memory and CPU time in comparison with the derivative computation.

4.7 Summary

We developed an efficient method for S -parameter sensitivity analysis based on a FDTD self-adjoint sensitivity expression with a TLM-based commercial time-domain EM solvers. The method converts the field solution from the TLM mesh to the FDTD mesh. It can be used to derive S -parameter sensitivities in both air and dielectric inhomogeneous structures.

Our approach is illustrated through the S -parameter sensitivities with respect to the shape parameters of antenna and waveguide discontinuities for either a frequency sweep or a parameter sweep. Our results and the convergence analysis show superior accuracy and efficiency of our approach than those of the finite-difference approximation. The S -matrix and its derivatives with respect to all design parameters are obtained through a single system analysis. The overhead of the sensitivity computation is negligible compared to the computational intensity of the time-domain full-wave simulation. The memory requirements of the sensitivity analysis are mostly due to the field waveforms recorded at the perturbation points.

4.8 References

- [1] MEFiSTo-3D[®] Pro v. 4, *User Guide and Operating Manual*, 6th ed., Faustus Scientific, Jan. 2003, <http://www.faustcorp.com/products/mefisto3dpro/> .
- [2] HFSS[®] v. 9.0, Ansoft, <http://www.ansoft.com/products/hf/hfss/> .
- [3] N.K. Nikolova, H.W. Tam, and M.H. Bakr, “Sensitivity analysis with the FDTD method on structured grids,” *IEEE Trans. Microwave Theory Tech.*, vol. 52, pp. 1207-1216, April 2004.
- [4] Y. Chung, C. Cheon, I. Park, and S. Hann, “Optimal shape design of microwave device using FDTD and design sensitivity analysis,” *IEEE Trans. Microwave Theory Tech.*, vol. 48, pp. 2289-2296, Dec. 2000.
- [5] M.H. Bakr, N.K. Nikolova, and P.A.W. Basl, “Self-adjoint *S*-parameter sensitivities for lossless homogeneous TLM problems,” *Int. J. of Numerical Modeling: Electronic Networks, Devices and Fields*, vol.18, pp. 441-455, Nov. 2005.
- [6] Ying Li, “TLM-based self-adjoint sensitivities of *S*-parameters with time-domain TLM electromagnetic solver,” Computational Electromagnetics Res. Lab., McMaster University, Feb. 2006.
- [7] Ying Li, N.K. Nikolova, and M.H. Bakr, “TLM-based self-adjoint sensitivities of *S*-parameters with time-domain electromagnetic solvers”, accepted by *IEEE MTT-S International Microwave Symposium*, 2006.
- [8] MATLAB[®] v. 7, The MathWorks, Inc.,
<http://www.mathworks.com/products/matlab/> .

- [9] L. Minakova and L. Rud, "Spectral approach to the synthesis of the waveguide bandstop filters based on dielectric rectangular posts," *Int. Conference on Mathematical Methods in Electromagnetic Theory MMET*, Sept. 2000, vol. 2, pp. 479-481.
- [10] D. Yau and N.V. Shuley, "A moment method analysis of an aperture coupled rectangular dielectric resonator antenna," *IEEE AP-S/URSI Int. Symp. on Antennas and Propagation*, vol. 2, July 1999, pp. 858-861.

Chapter 5

TIME DOMAIN SENSITIVITY ANALYSIS OF LOSSY INHOMOGENEOUS STRUCTURES

5.1 Introduction

We present an efficient adjoint-based approach to response derivative computations with respect to shape and constitutive parameters using time domain electromagnetic (EM) solutions in lossy dielectric inhomogeneous structures. This self-adjoint approach yields the derivatives without additional adjoint system analysis. The only requirement is access to the field solution at the perturbation grid points. The approach is verified in 1D and 2D examples using the time domain EM solver MEFiSTo-3D Pro [1].

The sensitivity analysis of microwave problems involving lossy media becomes increasingly important due to applications in design and inverse problems arising in non-destructive testing and biomedical imaging. The obtained response derivatives (response

Jacobian) can be used to guide a gradient-based optimizer as well as to provide a sufficiently good initial guess for the solution of the nonlinear inverse problem.

The efficiency of the approach used to obtain the response Jacobian is crucial in microwave inverse problems. It is rarely possible to use response-level derivative estimations such as finite differences when the number of optimizable parameters is large and the forward analysis uses full-wave simulations. In Chapter 4, we proposed an efficient time-domain self-adjoint analysis approach [2] for the computation of the sensitivities of the S -parameters. Regardless of the number of the optimizable parameters, and from only one system simulation, we obtain the S -parameters and all their derivatives. Beside its efficiency, the approach also features second-order accuracy. We confirmed our approach with metallic and lossless dielectric structures in [2]. Here, we extend our approach to lossy dielectric structures. Beside the S -parameters, we use a slightly different normalized response function, which is self-adjoint and is suitable for inverse imaging problems.

The significance of the sensitivity analysis of dielectric lossy inhomogeneous structures is due to the fact that most materials in the microwave inverse problems have significant losses. Breast tumor and subsurface detection, oil pocket location are some examples. Another factor, which makes this study important, is the difficulty of the inhomogeneous structure analysis. It is well known that an inhomogeneous medium with high loss (above 0.1 S/m) and large permittivity variations poses a challenge in numerical simulations [3]. This is due to the rapid field changes in time and in space, especially at interfaces. To achieve acceptable accuracy, the mesh has to be set more than twice finer

than the minimum limit recommended for loss-free problems. In this case, the efficiency of our approach is even more important.

We start with a brief introduction to the time-domain self-adjoint sensitivity analysis. We discuss its specifics for the case of derivatives with respect to the local constitutive parameters. The approach is illustrated and verified through 1D and 2D examples, where the inhomogeneous medium features high permittivities ($\epsilon_r \geq 12$) and losses ($\sigma \geq 0.5$). We conclude with a summary and our future developments.

5.2 FDTD-based AVM Theory with Material Parameters

The general FDTD-based AVM sensitivity expression is shown in Chapter 4 (4.14) and (4.15). In the case when the design parameter is a local permittivity or conductivity, we can obtain the analytical derivatives of the system coefficients from (4.4):

$$\frac{d\alpha}{d\epsilon_r} = \left(\frac{\Delta h}{c\Delta t} \right)^2, \quad \frac{ds}{d\sigma} = \frac{\mu_0 \Delta h^2}{2\Delta t}. \quad (5.1)$$

Therefore, the terms $\Delta_n \alpha / \Delta p_n$ and $\Delta_n s / \Delta p_n$ in (4.15) are substituted with the analytical expressions (5.1). Also, with analytical derivatives of the system coefficients, the adjoint solution must correspond to the unperturbed structure, i.e., $(\hat{\mathbf{E}})_n$ is replaced simply by $\hat{\mathbf{E}}$. There is no need for the solution mapping [4], which is necessary when dealing with shape parameters.

We notice that the sensitivity computation with respect to the constitutive parameters is more reliable, compared to the shape parameters. This is because it eliminates the inaccuracy in the system matrix derivative and depends only on the accuracy of the field solution.

The self-adjoint S -parameter sensitivity approach with respect to material parameters is similar to the case of shape parameters. However, in the case when the excitation is a point source in an open problem, the S -parameters may not be suitable response functions for the lack of port waveguides. Instead, we use a normalized response function. It is defined as

$$F_{PQ} = \frac{\tilde{E}_{PQ}}{\tilde{G}_Q}. \quad (5.2)$$

Here, E_{PQ} is the field solution at point P when point Q is excited; G_Q is the excitation waveform at point Q , and \tilde{E}_{PQ} and \tilde{G}_Q are their respective Fourier transforms (FT).

Similarly to (3.7), the derivative of F_{PQ} with respect to the n th parameter is computed as

$$\frac{\partial F_{PQ}}{\partial p_n} = \frac{1}{\tilde{G}_Q} \cdot \frac{\partial \tilde{E}_{PQ}}{\partial p_n}. \quad (5.3)$$

The derivative of \tilde{E}_{PQ} is computed as that of \tilde{F}_{pq} in the case of the S_{pq} parameter. The adjoint fields are derived in the same manner.

5.3 Validation Examples

We validate our approach with 1D and 2D lossy inhomogeneous examples. We compute the sensitivities of the S -parameters and a normalized response function with respect to both shape and constitutive parameters.

In all figures, we use TD-SASA as a notation for the results obtained by our self-adjoint sensitivity analysis, while FFD, CFD and BFD denote the forward, central and backward finite-difference estimates.

5.3.1 Normally Incident TEM Plane Wave in a Lossy Layered Medium

The structure and its dimensions are shown in Figure 5.1. Both the host medium and the inhomogeneity (shown in shade) are lossy. The field analysis is carried out in the time domain with MEFiSTo-3D Pro. The simulation setup is summarized in Table 5.1. The TLM solution is set on a uniform generalized symmetrical condensed node (GSCN) grid with $\Delta h / (c\Delta t) = 2$. It has a uniform field distribution across the port conforming to a TEM plane wave.

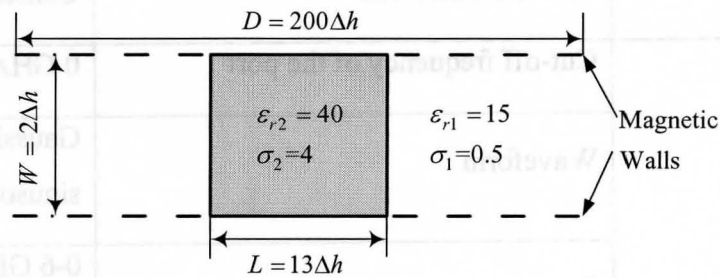


Figure 5.1 The structure of the 1D lossy-medium example.

Table 5.1. Setup of the 1D lossy-medium example simulation

Constant	Cell size Δh	1 mm
	Time step Δt	1.6678205 psec
Computational domain	Width of port a	2 mm ($2 \Delta h$)
	Length of the waveguide L_w	200 mm ($200 \Delta h$)
	Width of the central layer	2 mm ($2 \Delta h$)
	Length of the central layer	13 mm ($13 \Delta h$)
	Conductivity of the host σ_1	0.5
	Dielectric permittivity of the host ϵ_{r1}	15
	Conductivity of the central layer σ_2	4
	Dielectric permittivity of the central layer ϵ_{r2}	40
	Computational domain in space	$200 \Delta h \times 2 \Delta h$
Port	Total time steps	$30,000 \Delta t$
	Boundary condition	TEM wave absorbing boundary
Excitation	Modal distribution	Constant
	Cut-off frequency of the port	0 GHz
	Waveform	Gaussian modulated sinusoidal wave
	Spectrum	0-6 GHz, central frequency at 3 GHz

	Port distribution	Constant
Probes	Distance from the respective port	$20 \Delta h$

The design parameters are $\mathbf{p}^T = [\varepsilon_{r2} \ \sigma_2 \ L]$, which are the constitutive and shape parameters of the central layer. Figure 5.2 shows the derivative of $|S_{11}|$ with respect to the conductivity σ_2 of the middle layer. Figure 5.3 shows the derivative of $|S_{21}|$ with respect to its length L . Both analyses are performed over a frequency sweep from 0.3 GHz to 2.5 GHz. They show good agreement with the CFD results.

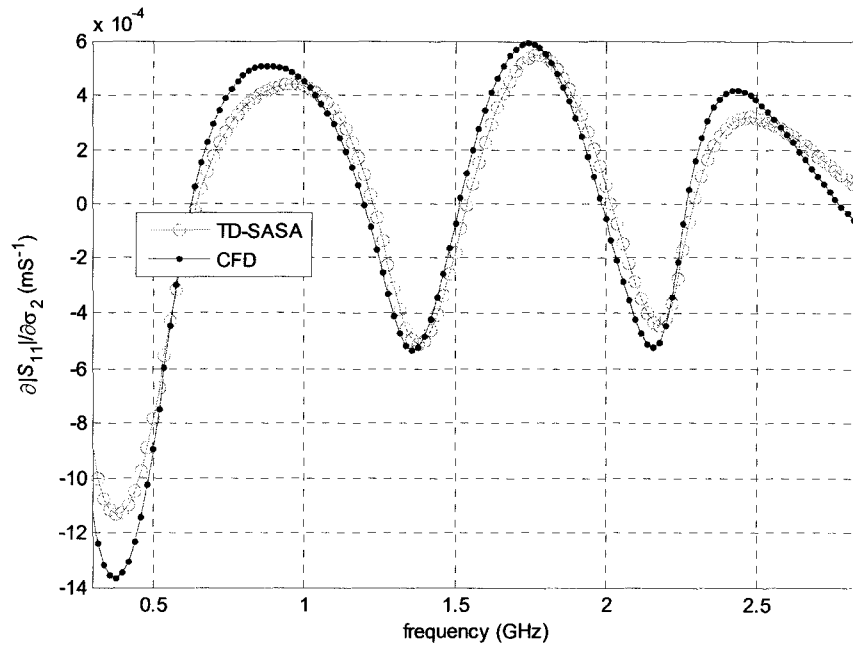


Figure 5.2. Derivative of $|S_{11}|$ with respect to the conductivity σ_2 of the central layer in the 1D lossy medium example.

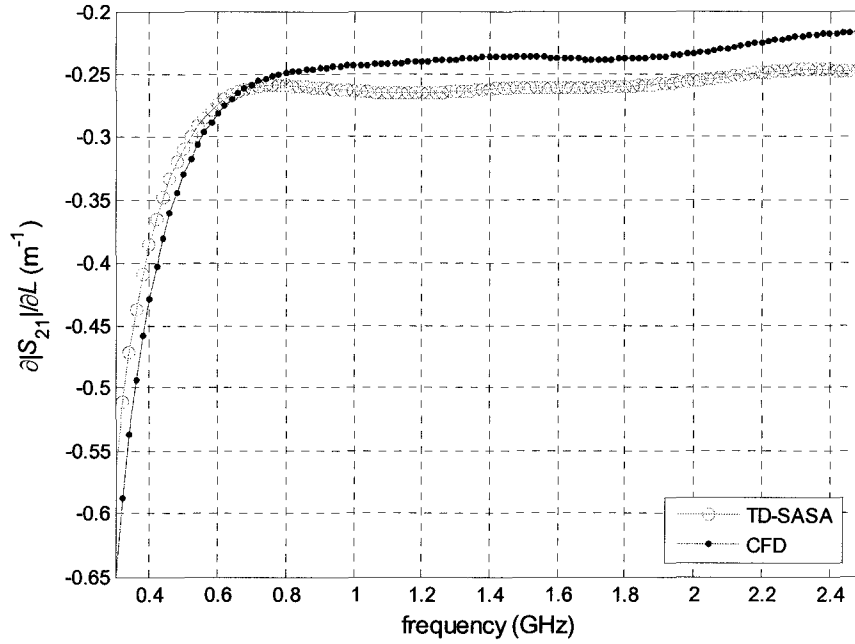


Figure 5.3. Derivative of $|S_{21}|$ with respect to the length L of the central layer in the 1D lossy medium example.

Since the locations of the field points on the TLM grid do not coincide with those on the FDTD Yee grid, we perform averaging [2] to obtain the field at the points required by the FDTD-based self-adjoint method. The difference in the excitation schemes of the TLM and FDTD methods leads to a constant factor of 10, which must be used to multiply to the final sensitivity value with TD-SASA formula in order to match the CFD result. In lossless problems in Chapter 4 this factor is 150. This factor is determined empirically by comparing the TD-SASA and the CFD derivatives with respect to one of the parameters. The derivatives with respect to any other parameter can be obtained with this same factor since it depends only on the constitutive parameters of the medium at the location of the source.

5.3.2 Object in a 2D Lossy Layered Medium

Figure 5.4 shows the top view and the dimensions of the nominal 2D structure. It consists of two different lossy mediums and an object placed in the middle layer. It is analyzed with MEFiSTo in a 2D TM_z mode. The simulation setup is shown in Table 5.2.

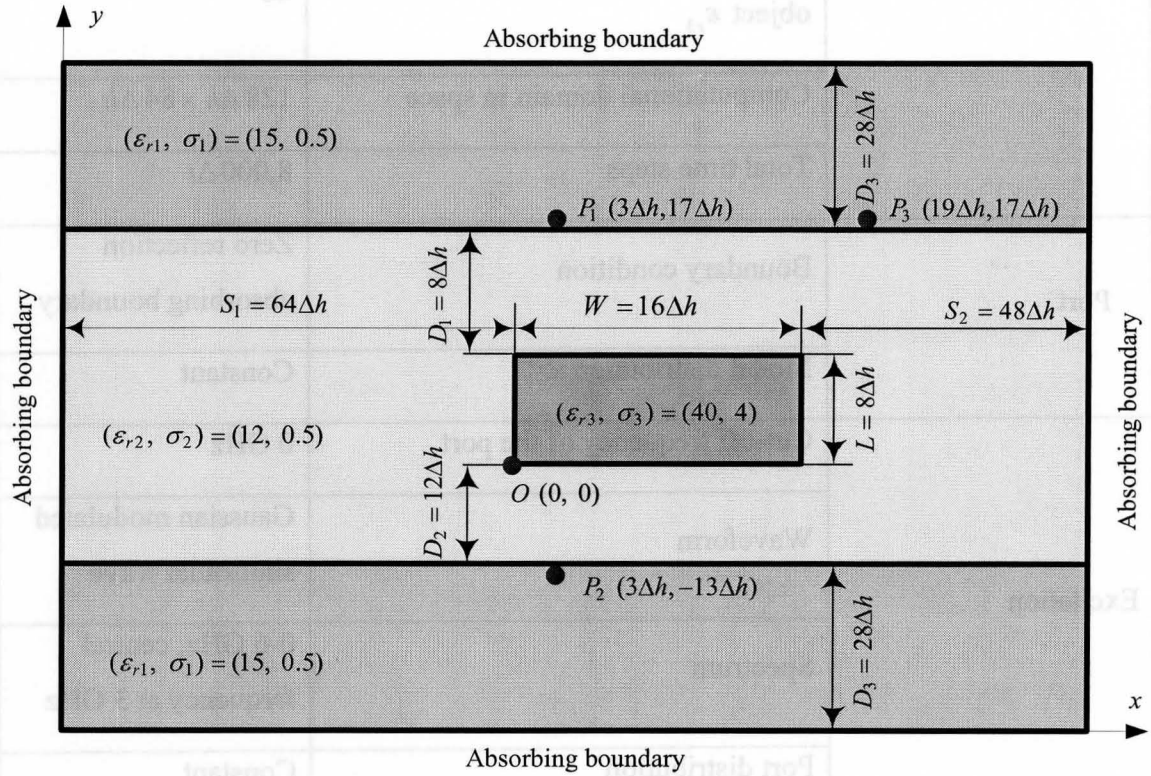


Figure 5.4. Top view of the structure in the 2D example.

Table 5.2. Setup of the 2D lossy layered medium example simulation

Constant	Cell size Δh	1 mm
	Time step Δt	1.6678205 psec
Computational domain	Width of the central object	16 mm (16 Δh)
	Length of the central object	8 mm (8 Δh)
	Conductivity of the central object σ_3	4
	Dielectric permittivity of the central object ϵ_{r3}	40
	Computational domain in space	128 $\Delta h \times 84 \Delta h$
	Total time steps	8,000 Δt
Port	Boundary condition	Zero reflection absorbing boundary
	Modal distribution	Constant
Excitation	Cut-off frequency of the port	0 GHz
	Waveform	Gaussian modulated sinusoidal wave
	Spectrum	0-6 GHz, central frequency at 3 GHz
	Port distribution	Constant
Probes	Distance from the respective port	20 Δh

The design parameters include the shape parameters W and L and the constitutive parameters $\varepsilon_{r,3}$ and σ_3 of the object. We use the normalized response function F_{PQ} in (5.3). In Figure 5.4, P_1 is the excitation point while P_2 and P_3 are the observation points. They are placed at the interfaces of the layers. In this example, we obtain the sensitivities of $|F_{PQ}|$ with respect to σ_3 and W over parameter sweeps at a certain frequency. The derivative curves are plotted in Figure 5.5 and Figure 5.6, respectively.

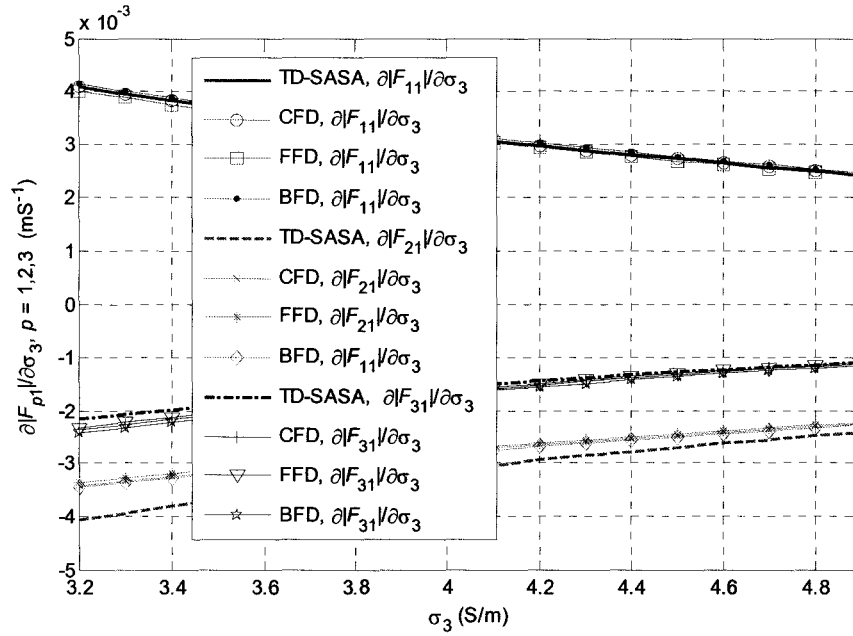


Figure 5.5. Derivatives of $|F_{P_kR}|$, $k = 1, 2, 3$, with respect to σ_3 of the central object for a sweep of σ_3 at 0.9 GHz.

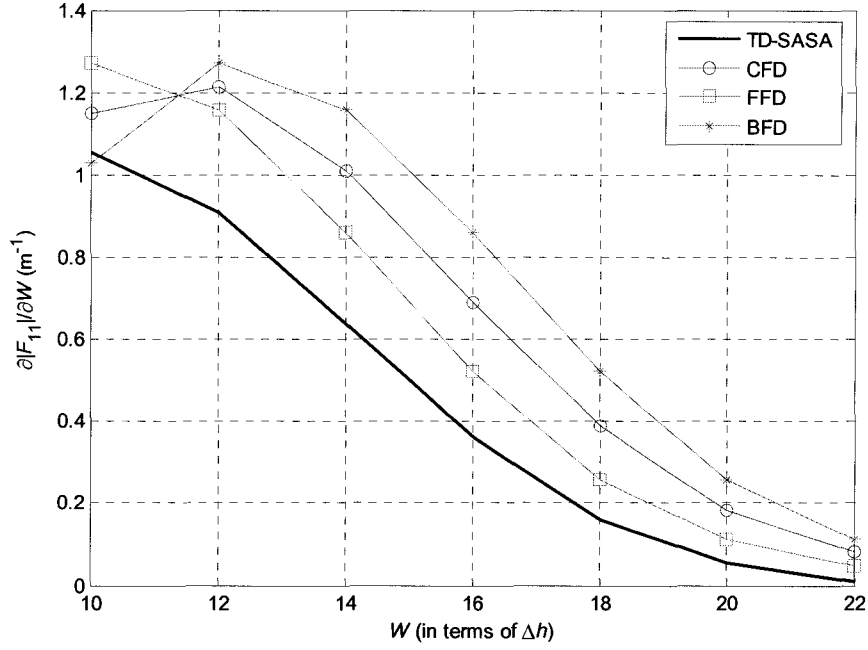


Figure 5.6. Derivatives of $|F_{PR}|$ with respect to the width W of the central object for a sweep of W at 2.6 GHz.

We notice that the agreement between the TD-SASA and CFD derivative estimates with respect to σ_3 in Figure 5.5 is good, while for the derivatives with respect to W in Figure 5.6 it is worse. The reason for the difference may be that more field points are involved in the computation of the derivatives with respect to σ_3 than those with respect to W . In fact, our results at other frequency points are generally much worse than those in Figure 5.5 and Figure 5.6. Compared with our results in the lossless structures [2], we believe that the significant losses affect negatively the sensitivity results. In order to determine which results are more accurate, the TD-SASA or the finite-difference derivative estimates, we have to perform convergence analysis.

5.4 Summary

We presented a self-adjoint sensitivity analysis method for the computation of the response derivatives with respect to constitutive and shape parameters in lossy inhomogeneous structures. The method is based on the FDTD discretization scheme; however, the field solution is obtained with the TLM-based commercial simulator MEFiSTo-3D Pro. The approach is intended for applications to the solution of inverse microwave imaging problems arising in biomedical diagnostics and non-destructive testing.

Our method can provide the response Jacobians needed in the inverse optimization at a computational cost, which is just a fraction of what is required by the response-level finite differences. In the 1D case, it also provides accuracy comparable to that of the central finite-difference approach. In the 2D case, the agreement is not satisfactory in general. Further investigations are needed to solve these problems by carrying out convergence analyses or comparisons with examples, which have analytical solutions.

5.5 References

- [1] MEFiSTo-3D[®] Pro v. 4, Faustus Scientific,
<http://www.faustcorp.com/products/mefisto3dpro/> .

- [2] N.K. Nikolova, Ying Li, Yan Li, and M.H. Bakr, "Sensitivity analysis of scattering parameters with electromagnetic time-domain simulators," *IEEE Trans. Microwave Theory Tech.*, vol. 54, no. 4, pp. 1598-1610, April 2006.
- [3] Allen Taflove, *Computational Electrodynamics: The Finite-Difference Time-Domain Method*. Artech House, Inc, 1995.
- [4] N.K. Nikolova, H.W. Tam, and M.H. Bakr, "Sensitivity analysis with the FDTD method on structured grids," *IEEE Trans. Microwave Theory Tech.*, vol. 52, pp. 1207-1216, April 2004.

Chapter 6

CONCLUSIONS

In this thesis, the theory and implementation of the self-adjoint sensitivity analysis (SASA) of the S -parameters with time-domain commercial EM solvers are presented. The self-adjoint approach enables the calculation of the S -parameter derivatives with respect to all the shape and material parameters efficiently and accurately. The computation is done as an independent post-process with negligible overhead, which means that we can obtain the sensitivity information in addition to the field solution and network parameters with a single simulation at the nominal design.

Our self-adjoint sensitivity analysis theory is based on the adjoint variable method (AVM). The development of the discrete form of the AVM and the self-adjoint approach make the implementation of the AVM possible with time-domain commercial EM solvers, which can not in general run backward adjoint simulations. Thus, our approach is readily applicable to practical gradient-based design problems.

The SASA theory can be formulated based on two widely used time-domain analysis methods: the FDTD method and the TLM. Our implementation uses the TLM-based commercial solver MEFiSTo-3D Pro. In Chapter 2, the field solution given by

MEFiSTo is validated by HFSS, and an independent S -parameter calculation based on the MEFiSTo field solution. In Chapters 3 and 4, we present the SASA approach based on the FDTD and TLM analyses, respectively. We convert the field solution of MEFiSTo to apply each of the two SASA theories. For the TLM-based SASA, the E and H field solution is converted to the TLM incident and reflected impulses. In the FDTD-based SASA, the E field solution in the TLM mesh is converted into a FDTD mesh solution. The TLM-based and FDTD-based SASA algorithms can be applied with any time-domain solver, no matter what numerical method they use.

The TLM-based SASA algorithm is limited to the loss-free homogeneous case, while the FDTD-based SASA is valid also for lossy inhomogeneous structures. In Chapter 5, we demonstrate the self-adjoint sensitivities with respect to both shape and material parameters for structures with high permittivity variations and high losses.

From the validation examples, we can conclude that the accuracy of the SASA is comparable to the second-order central finite-difference derivative estimates, except when the S -parameter is insensitive, i.e., the derivative is too small. The efficiency of our SASA algorithm is quite obvious in the cases where the number of design parameters is large or the computational load of the simulation (e.g. 3D problems) is heavy.

From the experience and knowledge gained in the above work, the following topics for further research are suggested:

- 1) The SASA approach can be integrated into commercial EM solvers, which will add new capability for the efficient sensitivity analysis for practical design problems, in addition to the accurate system response analysis. More work should

be done for its commercialization. For example, how to find the positions of the user-defined points to be recorded automatically for different structures, and how to expedite the interface between the EM solvers and the Jacobian calculation post-process.

- 2) The accuracy of the SASA algorithm in highly lossy media should be improved and validated. Further study of the adjoint sensitivity analysis in lossy inhomogeneous structures can be carried out for inverse problems, such as microwave imaging and non-destructive testing.
- 3) The TLM-based SASA theory can be extended to the lossy inhomogeneous problems analyzed with commercial solvers. The development and application of the SASA theory for the printed structures in the 3D case are also challenging topics.

COMPLETE REFERENCE LIST

Chapter 1

- [1] E.J. Haug, K.K. Choi and V. Komkov, *Design Sensitivity Analysis of Structural Systems*. Orlando: Academic Press Inc., 1986, pp. 70-77, pp. 167-178.
- [2] E.J. Haug and J. Céa, eds., *Optimization of Distributed Parameter Structures*. Alphen aan den Rijn, the Netherlands: Sijthoff & Noordhoff, 1981.
- [3] Y. Chung, C. Cheon, I. Park, and S. Hann, “Optimal shape design of microwave device using FDTD and design sensitivity analysis,” *IEEE Trans. Microwave Theory Tech.*, vol. 48, pp. 2289-2296, Dec. 2000.
- [4] Y. Chung, J. Ryu, C. Cheon, I. Park and S. Hahn, “Optimal design method for microwave device using time domain method and design sensitivity analysis – part I: FETD case,” *IEEE Trans. Magnetics*, vol. 37, pp. 3289-3293, Sep. 2001.
- [5] Y. Chung, J. Ryu, C. Cheon, I. Park and S. Hahn, “Optimal design method for microwave device using time domain method and design sensitivity analysis – part II: FDTD case,” *IEEE Trans. Magnetics*, vol. 37, pp. 3255-3259, Sep. 2001.
- [6] N.K. Nikolova, J.W. Bandler, and M.H. Bakr, “Adjoint techniques for sensitivity analysis in high-frequency structure CAD,” *IEEE Trans. Microwave Theory Tech.*, vol. 52, pp. 403-419, Jan. 2004.

- [7] A. Taflove, S.C. Hagness, *Computation Electrodynamics: The Finite Difference Time-Domain Method*, 2nd ed. Boston: Artech House, 2000.
- [8] C. Christopoulos, *The Transmission-Line Modeling Method TLM*. Oxford: IEEE/Oxford University Press, 1995.
- [9] W.J.R. Hoefer, "The transmission-line matrix method – theory and applications," *IEEE Trans. Microwave Theory Tech.*, vol. MTT-33, pp. 882-893, Oct. 1985.
- [10] M.H. Bakr and N.K. Nikolova, "An adjoint variable method for time domain TLM with fixed structured grids," *IEEE Trans. Microwave Theory Tech.*, vol. 52, pp. 554-559, Feb. 2004.
- [11] N.K. Nikolova, H.W. Tam, and M.H. Bakr, "Sensitivity analysis with the FDTD method on structured grids," *IEEE Trans. Microwave Theory Tech.*, vol. 52, pp. 1207-1216, April 2004.
- [12] M.H. Bakr and N.K. Nikolova, "Efficient estimation of adjoint-variable *S*-parameter sensitivities with time domain TLM," *Int. J. of Numerical Modelling: Electronic Networks, Devices and Fields*, vol. 18, No. 2, March/April 2005, pp. 171-187.
- [13] M.H. Bakr, N.K. Nikolova, and P.A.W. Basl, "Self-adjoint *S*-parameter sensitivities for lossless homogeneous TLM problems," *Int. J. of Numerical Modelling: Electronic Networks, Devices and Fields*, vol. 18, No. 6, Nov. 2005, pp. 441-455.
- [14] MEFiSTo-3D[®] Pro v. 4, *User Guide and Operating Manual*, 6th ed., Faustus Scientific, Jan. 2003, <http://www.faustcorp.com/products/mefisto3dpro/> .

- [15] XFDTD[®] v. 6.2, *Reference Manual*, Remcom, 2004,
<http://www.remcom.com/xfDTD6/> .
- [16] MATLAB[®] v. 7, The MathWorks, Inc.,
<http://www.mathworks.com/products/matlab/> .
- [17] Ying Li, N.K. Nikolova, and M.H. Bakr, “TLM-based self-adjoint sensitivities of *S*-parameters with time-domain electromagnetic solvers”, accepted by *IEEE MTT-S International Microwave Symposium*, 2006.
- [18] N.K. Nikolova, Ying Li, Yan Li, and M.H. Bakr, “Sensitivity analysis of scattering parameters with electromagnetic time-domain simulators,” *IEEE Trans. Microwave Theory Tech.*, vol. 54, no. 4, pp. 1598-1610, April 2006.
- [19] Ying Li, Yan Li, N.K. Nikolova, and M.H. Bakr, “Time domain sensitivity analysis of lossy dielectric structures,” accepted by *Frontiers in Applied Computational Electromagnetics*, 2006.

Chapter 2

- [1] MEFiSTo-3D[®] Pro v. 4, *User Guide and Operating Manual*, 6th ed., Faustus Scientific, Jan. 2003, <http://www.faustcorp.com/products/mefisto3dpro/> .
- [2] MATLAB[®] v. 7, The MathWorks, Inc.,
<http://www.mathworks.com/products/matlab/> .
- [3] HFSS[®] v. 9.0, Ansoft, <http://www.ansoft.com/products/hf/hfss/> .
- [4] N. Marcuvitz, *Waveguide Handbook*. London, UK: Peter Peregrinus Ltd., 1993 reprint, Chapter 2.

- [5] Y. Qian and T. Itoh, *FDTD Analysis and Design of Microwave Circuits and Antennas: Software and Applications*, Realize Inc., Tokyo, 1999.
- [6] K. S. Yee, "Numerical solution of initial boundary value problems involving Maxwell's equations in isotropic media," *IEEE Transactions on Antennas and Propagation*, vol. AP-14, pp.302-307, 1966.
- [7] Allen Taflov, *Computational Electrodynamics: The Finite-Difference Time-Domain Method*. Artech House, Inc., 1995.
- [8] Matthew N.O. Sadiku. *Numerical Techniques in Electromagnetics*. 2nd edition, 2001.

Chapter 3

- [1] HFSS[®] v. 9.0, Ansoft, <http://www.ansoft.com/products/hf/hfss/> .
- [2] M.H. Bakr, N.K. Nikolova, "An adjoint variable method for time-domain transmission-line modeling with fixed structured grids," *IEEE Trans. Microwave Theory Tech.*, vol. 52, no. 2, pp. 554–559, Feb. 2004.
- [3] M.H. Bakr, N.K. Nikolova, "Efficient estimation of adjoint-variable *S*-parameter sensitivities with time-domain TLM," *International Journal of Numerical Modeling: Electronic Networks, Devices and Fields*, vol. 18, no.2, pp. 171-187, March/April 2005.
- [4] M.H. Bakr, N.K. Nikolova, and P.A.W. Basl, "Self-adjoint *S*-parameter sensitivities for lossless homogeneous TLM Problems," *Int. J. of Numerical*

- Modeling: Electronic Networks, Devices and Fields*, vol.18, pp. 441-455, Nov. 2005.
- [5] MEFiSTo-3D[®] Pro v. 4, *User Guide and Operating Manual*, 6th ed., Faustus Scientific, Jan. 2003, <http://www.faustcorp.com/products/mefisto3dpro/> .
- [6] Z. Chen, M.M. Ney, W.J.R. Hoefer, “A new finite-difference time-domain formulation and its equivalence with TLM symmetrical condensed node,” *IEEE Trans. Microwave Theory Tech.*, vol. 39, no. 12, pp. 2160–2169, Dec. 1991.
- [7] N.K. Nikolova, H.W. Tam, and M.H. Bakr, “Sensitivity analysis with the FDTD method on structured grids,” *IEEE Trans. Microwave Theory Tech.*, vol. 52, pp. 1207-1216, April 2004.

Chapter 4

- [1] MEFiSTo-3D[®] Pro v. 4, *User Guide and Operating Manual*, 6th ed., Faustus Scientific, Jan. 2003, <http://www.faustcorp.com/products/mefisto3dpro/> .
- [2] HFSS[®] v. 9.0, Ansoft, <http://www.ansoft.com/products/hf/hfss/> .
- [3] N.K. Nikolova, H.W. Tam, and M.H. Bakr, “Sensitivity analysis with the FDTD method on structured grids,” *IEEE Trans. Microwave Theory Tech.*, vol. 52, pp. 1207-1216, April 2004.
- [4] Y. Chung, C. Cheon, I. Park, and S. Hann, “Optimal shape design of microwave device using FDTD and design sensitivity analysis,” *IEEE Trans. Microwave Theory Tech.*, vol. 48, pp. 2289-2296, Dec. 2000.

- [5] M.H. Bakr, N.K. Nikolova, and P.A.W. Basl, "Self-adjoint S -parameter sensitivities for lossless homogeneous TLM problems," *Int. J. of Numerical Modeling: Electronic Networks, Devices and Fields*, vol.18, pp. 441-455, Nov. 2005.
- [6] Ying Li, "TLM-based self-adjoint sensitivities of S -parameters with time-domain TLM electromagnetic solver," Computational Electromagnetics Res. Lab., McMaster University, Feb. 2006.
- [7] Ying Li, N.K. Nikolova, and M.H. Bakr, "TLM-based self-adjoint sensitivities of S -parameters with time-domain electromagnetic solvers", accepted by *IEEE MTT-S International Microwave Symposium*, 2006.
- [8] MATLAB[®] v. 7, The MathWorks, Inc.,
<http://www.mathworks.com/products/matlab/> .
- [9] L. Minakova and L. Rud, "Spectral approach to the synthesis of the waveguide bandstop filters based on dielectric rectangular posts," *Int. Conference on Mathematical Methods in Electromagnetic Theory MMET*, Sept. 2000, vol. 2, pp. 479-481.
- [10] D. Yau and N.V. Shuley, "A moment method analysis of an aperture coupled rectangular dielectric resonator antenna," *IEEE AP-S/URSI Int. Symp. on Antennas and Propagation*, vol. 2, July 1999, pp. 858-861.

Chapter 5

- [1] MEFiSTo-3D[®] Pro v. 4, Faustus Scientific,
<http://www.faustcorp.com/products/mefisto3dpro/> .
- [2] N.K. Nikolova, Ying Li, Yan Li, and M.H. Bakr, “Sensitivity analysis of scattering parameters with electromagnetic time-domain simulators,” *IEEE Trans. Microwave Theory Tech.*, vol. 54, no. 4, pp. 1598-1610, April 2006.
- [3] Allen Taflove, *Computational Electrodynamics: The Finite-Difference Time-Domain Method*. Artech House, Inc, 1995.
- [4] N.K. Nikolova, H.W. Tam, and M.H. Bakr, “Sensitivity analysis with the FDTD method on structured grids,” *IEEE Trans. Microwave Theory Tech.*, vol. 52, pp. 1207-1216, April 2004.